

LECTURES ON TROPICAL METEOROLOGY

Roger K. Smith

June 26, 2003



Contents

1	INTRODUCTION TO THE TROPICS	3
1.1	The zonal mean circulation	5
1.2	Data network in the Tropics	8
1.3	Field Experiments	10
1.4	Macroscale circulations	12
1.5	More on the Walker Circulation	18
1.6	El Niño and the Southern Oscillation	19
1.7	The Madden-Julian/Intraseasonal Oscillation	25
1.8	More on Monsoons	28
1.8.1	The Regional Theory	29
1.8.2	The Planetary Theory	29
1.9	Monsoon variability	31
1.10	Synoptic-scale disturbances	31
2	EQUATIONS AND SCALING AT LOW LATITUDES	37
2.1	The governing equations on a sphere	37
2.2	The hydrostatic equation at low latitudes	39
2.3	Scaling at low latitudes	41
2.4	Diabatic effects, radiative cooling	44
2.5	Some further notes on the scaling at low latitudes	48
2.6	The weak temperature gradient approximation	49
3	MORE ON DIABATIC PROCESSES	51
4	THE HADLEY CIRCULATION	58
4.1	The Held-Hou Model of the Hadley Circulation.	60
4.2	Extensions to the Held-Hou Model	66
5	WAVES AT LOW LATITUDES	71
5.1	The equatorial beta-plane approximation	75
5.2	The Kelvin Wave	77
5.3	Equatorial Gravity Waves	77
5.4	Equatorial Rossby Waves	78
5.5	The mixed Rossby-gravity wave	78

5.6	The equatorial waveguide	81
5.7	The planetary wave motions	85
5.8	Baroclinic motions in low latitudes	86
5.9	Vertically-propagating wave motions	87
5.9.1	Kelvin wave	88
5.9.2	Mixed Rossby-gravity wave	89
6	STEADY AND TRANSIENT FORCED WAVES	94
6.1	Response to steady forcing	94
6.1.1	Zonally-independent flow	95
6.1.2	Zonally-dependent flow	97
6.2	Response to transient forcing	98
6.3	Wintertime cold surges	107
7	MOIST CONVECTION AND CONVECTIVE SYSTEMS	119
7.1	Moist versus dry convection	119
7.2	Conditional instability	120
7.3	Shallow convection	121
7.4	Precipitating convection	122
7.5	Precipitation-cooled downdraughts	124
7.6	Organized convective systems	126
7.7	Clouds in the tropics	127
7.8	Interaction between convection and the large-scale flow	132
A	Appendix to Chapter 4	135
B	The WBK-approximation	137

Chapter 1

INTRODUCTION TO THE TROPICS

In geographical terminology “the tropics” refers to the region of the earth bounded by the Tropic of Cancer (lat. 23.5°N) and the Tropic of Capricorn (lat. 23.5°S). These are latitudes where the sun reaches the zenith just once at the summer solstice. An alternative definition would be to choose the region 30°S to 30°N , thereby dividing the earth's surface into equal halves. Defined in this way the tropics would be the source of all the angular momentum of the atmosphere and most of the heat. But is this meteorologically sound? Some parts of the globe experience “tropical weather” for a part of the year only - southern Florida would be a good example. While Tokyo (36°N) frequently experiences tropical cyclones, called “typhoons” in the Northwest Pacific region, Sydney (34°S) never does.

Riehl (1979) chooses to define the meteorological “tropics” as those parts of the world where atmospheric processes differ significantly from those in higher latitudes. With this definition, the dividing line between the “tropics” and the “extratropics” is roughly the dividing line between the easterly and westerly wind regimes. Of course, this line varies with longitude and it fluctuates with the season. Moreover, in reality, no part of the atmosphere exists in isolation and interactions between the tropics and extratropics are important.

Figure 1.1 shows a map of the principal land and ocean areas within 40° latitude of the equator. The markedly non-uniform distribution of land and ocean areas in this region may be expected to have a large influence on the meteorology of the tropics. Between the Western Pacific Ocean and the Indian Ocean, the tropical land area is composed of multitude of islands of various sizes. This region, to the north of Australia, is sometimes referred to as the “Maritime Continent”, a term that was introduced by Ramage (1968). Sea surface temperatures there are particularly warm providing an ample moisture supply for deep convection. Indeed, deep convective clouds are such a dominant feature of the Indonesian Region that the area has been called “the boiler-box” of the atmosphere. The Indian Ocean and West Pacific region with the maritime continent delineated is shown in Fig. 1.2.

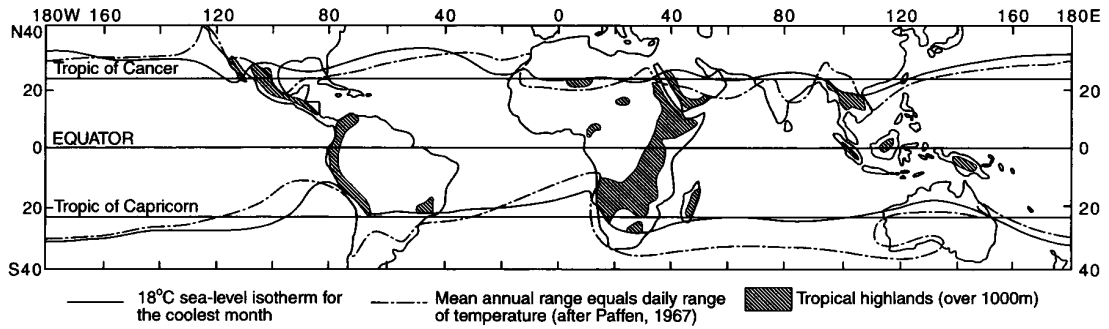


Figure 1.1: Principal land and ocean areas between 40°N and 40°S. The solid line shows the 18°C sea level isotherm for the coolest month; the dot-dash line is where the mean annual range equals the mean daily range of temperature. The shaded areas show tropical highlands over 1000 m. (From Nieuwolt, 1977)

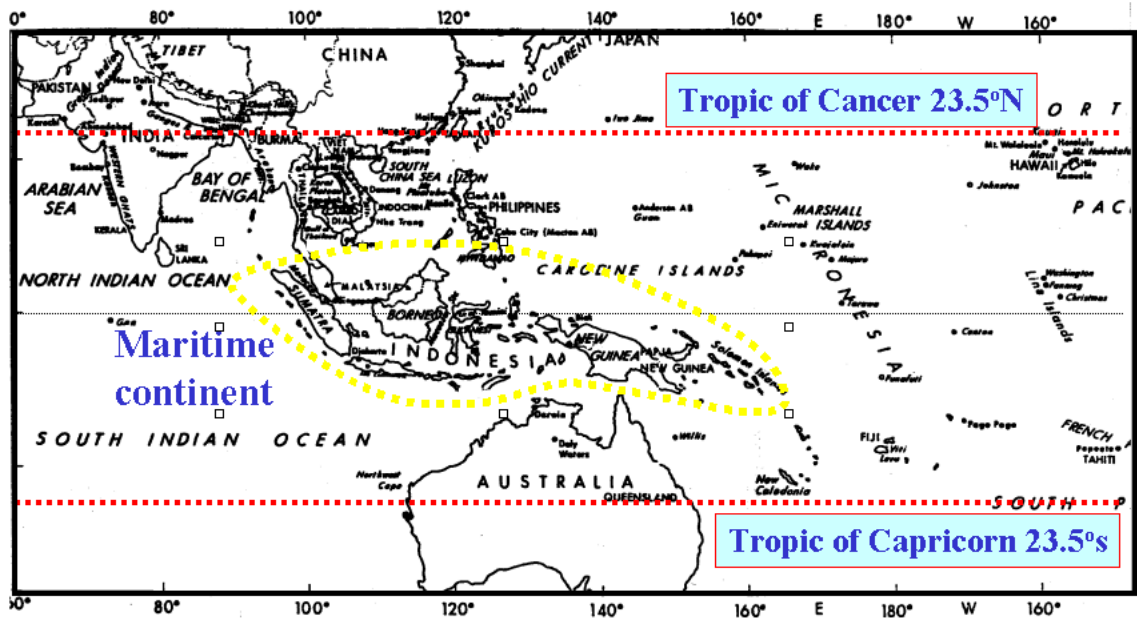


Figure 1.2: Indian Ocean and Western Pacific Region showing the location of the Maritime Continent (the region surrounded by a dashed closed curve).

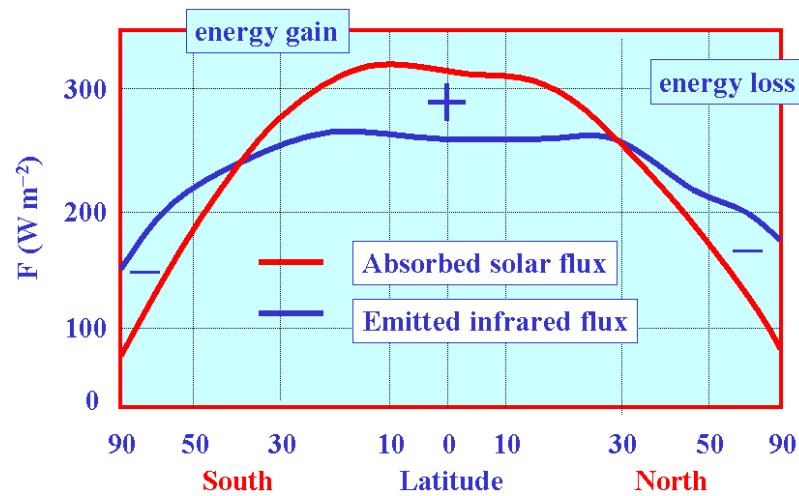


Figure 1.3: Zonally averaged components of the absorbed solar flux and emitted thermal infrared flux at the top of the atmosphere. + and – denote energy gain and loss, respectively. (From Vonder Haar and Suomi, 1971, with modifications)

1.1 The zonal mean circulation

Figure 1.3 shows the distribution of mean incoming and outgoing radiation at the edge of the atmosphere averaged zonally and over a year. If the earth-atmosphere system is in thermal equilibrium, these two streams of energy must balance. It is evident that there is a surplus of radiative energy in the tropics and a net deficit in middle and in high latitudes, requiring on average a poleward transport of energy by the atmospheric circulation. Despite the surplus of radiative energy in the tropics, *the tropical atmosphere is a region of net radiative cooling* (Newell *et al.*, 1974). The fact is that this surplus energy heats the ocean and land surfaces and evaporates moisture. In turn, some of this heat finds its way into the atmosphere in the form of sensible and latent heat and it is energy of this type that is transported polewards by the atmospheric circulation.

Figure 1.4 shows the zonally-averaged distribution of mean annual precipitation as function of latitude. Note that the precipitation is higher in the tropics than in the extratropics with a maximum a few degrees north of the equator. When precipitation occurs, i.e. a net amount of condensation without re-evaporation, then latent heat is released. The implication is that latent heat release may be an important effect in the tropics.

Figure 1.4 shows the zonally-averaged distribution of mean annual precipitation as function of latitude. Note that the precipitation is higher in the tropics than in the extratropics with a maximum a few degrees north of the equator. When precipitation occurs, i.e. a net amount of condensation without re-evaporation, then latent heat is released. The implication is that latent heat release may be an important effect

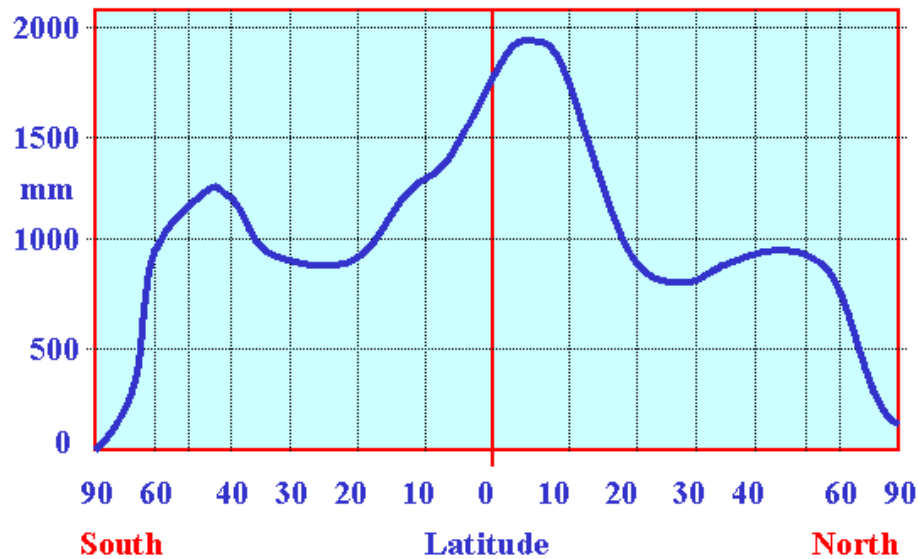


Figure 1.4: Mean annual precipitation as a function of latitude. (After Sellers, 1965)

in the tropics.



A variety of diagrams have been published depicting the mean meridional circulation of the atmosphere (see, e.g. Smith, 1993, Ch. 2). While these differ in detail, especially in the upper troposphere subtropics, they all show a pronounced Hadley cell with convergence towards the equator in the low-level trade winds, rising motion at or near the equator in the so-called *equatorial trough*, which is co-located with the *intertropical convergence zone* (ITCZ), poleward flow in the upper troposphere and subsidence into the subtropical high pressure zones. The ITCZ is a narrow zone paralleling the equator, but lying at some distance from it, in which air from one hemisphere converges towards air from the other to produce cloud and precipitation. It is characterized by low pressure and cyclonic relative vorticity in the lower troposphere. Usually the ITCZ is well marked only at a small range of longitudes at any one time. Figure 1.7 shows a case of an ITCZ marked by a very narrow line of deep convection across the Atlantic ocean, a little north of the Equator, while Fig. 1.8 shows an unusual case with the ITCZ stretching across much of the Pacific Ocean.

Figure 1.9 shows the zonally-averaged zonal wind component at 750 mb and 250 mb during June, July and August (JJA) and December, January and February (DJF). The most important features are the separation of the equatorial easterlies and middle-latitude westerlies and the variation of the structure between seasons. In particular, the westerly jets are stronger and further equatorward in the winter hemisphere. The rather irregular distribution of land and sea areas in and adjacent to the tropics gives rise to significant variation of the flow with longitude so that zonal averages of various quantities may obscure a good deal of the action!

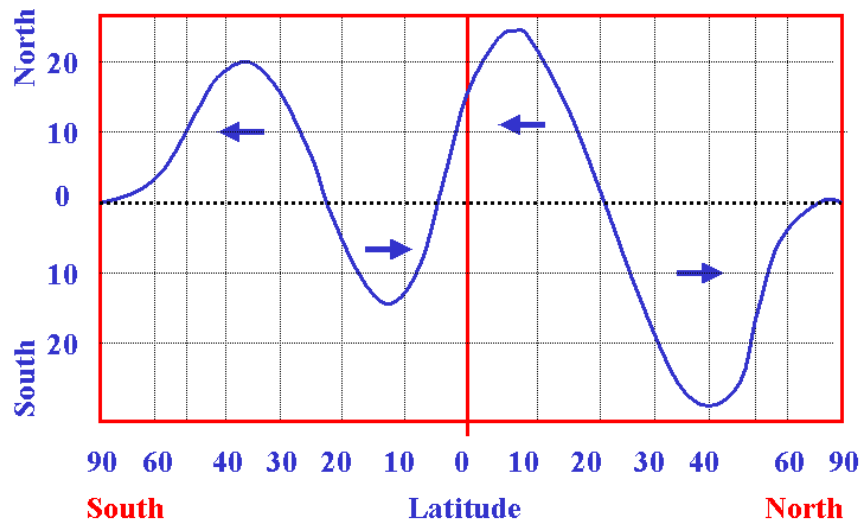


Figure 1.5: The mean annual meridional transfer of water vapour in the atmosphere (in 10^{15} kg). (After Sellers, 1965)

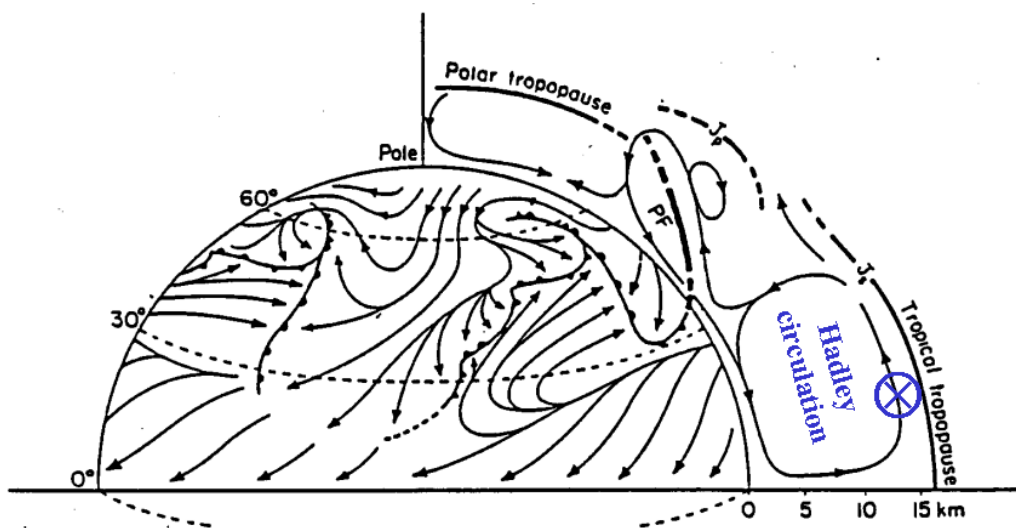


Figure 1.6: The mean meridional circulation and main surface wind regimes. (From Defant, 1958)

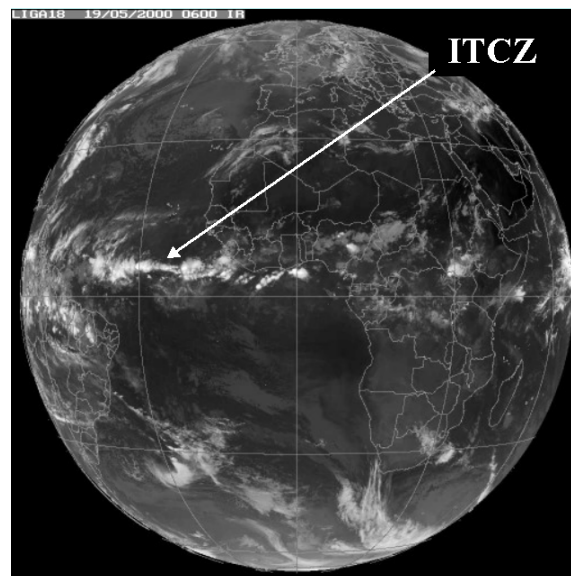


Figure 1.7: Visible satellite imagery from the EUMETSAT geostationary satellite at 0600 GMT on 19 May 2000 showing a well-formed ITCZ across the Atlantic Ocean.

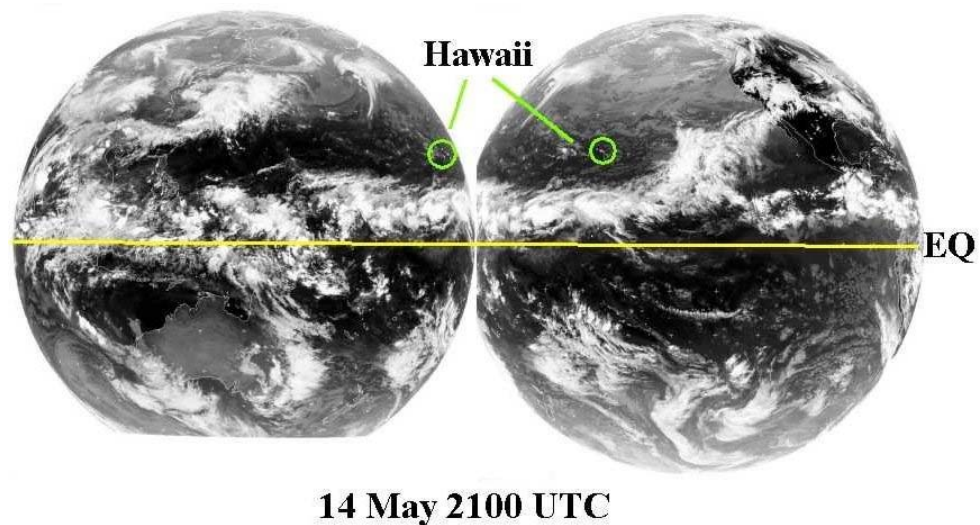


Figure 1.8: Visible satellite imagery from the two geostationary satellites at 2100 GMT on 14 May 2003 showing a well-formed ITCZ across the entire Pacific Ocean.

1.2 Data network in the Tropics

One factor that has hampered the development of tropical meteorology is the relatively coarse data network, especially the upper air network, compared with the network available in the extra-tropics, at least in the Northern Hemisphere. This

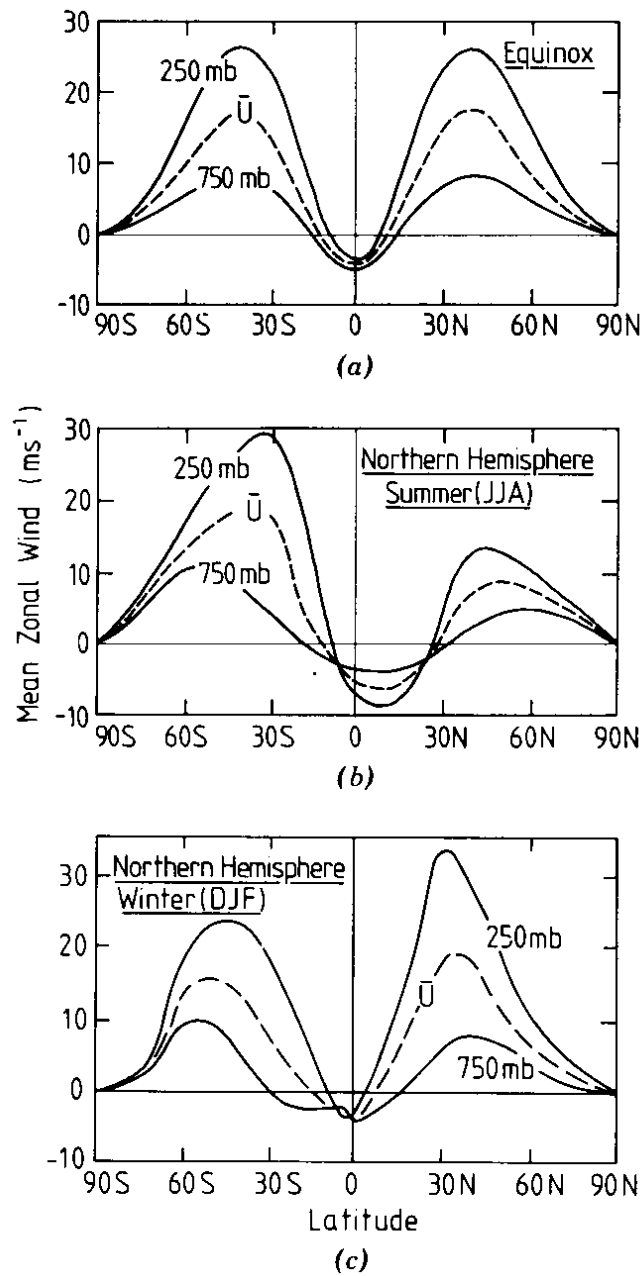


Figure 1.9: Mean seasonal zonally averaged wind at 250 mb and 750 mb for (a) the equinox, (b) JJA, and (c) DJF as a function of latitude. The dashed line indicates the tropospheric vertical average. Units are m s^{-1} . (Adapted from Webster, 1987b)

situation is a consequence of the land distribution and hence the regions of human settlement.

The main operational instruments that provide detailed and reliable information on the vertical structure of the atmosphere are radiosondes and rawinsondes. Fig-

ure 1.10 shows the distribution and reception rates of radiosonde reports that were received by the European Centre for Medium Range Weather Forecasts (ECMWF) during April 1984. The northern hemisphere continents are well covered and reception rates from these stations are generally good. However, coverage within the tropics, with certain notable exceptions, is minimal and reception rates of many tropical stations is low. Central America, the Caribbean, India and Australia are relatively well-covered, with radiosonde soundings at least once a day and wind soundings four times a day. However, most of Africa, South America and virtually all of the oceanic areas are very thinly covered. The situation at the beginning of the 21st century is much the same.

Satellites have played an important role in alleviating the lack of conventional data, but only to a degree. For example, they provide valuable information on the location of tropical convective systems and storms and can be used to obtain “cloud-drift” winds. The latter are obtained by calculating the motion of small cloud elements between successive satellite pictures. A source of inaccuracy lies in the problem of ascribing a height to the chosen cloud elements. Using infra-red imagery one can determine at least the cloud top temperature which can be used to infer the broad height range. Generally use is made of low level clouds, the motion of which is often ascribed to the 850 mb level (approximately 1.5 km), and high level cirrus clouds, their motion being ascribed to the 200 mb level (approximately 12 km). Clouds with tops in the middle troposphere are avoided because it is less clear what their “steering level” is.

Satellites instruments have been developed also to obtain vertical temperature soundings throughout the atmosphere, an example being the TOVS instrument (TIROS-N Operational Vertical Sounder) described by Smith *et al.* (1979), which is carried on the polar-orbiting TIROS-N satellite. While these data do not compete in accuracy with radiosonde soundings, their areal coverage is very good and they can be valuable in regions where radiosonde soundings are sparse.

A further important source of data in the tropics arises from aircraft wind reports, mostly from jet aircraft which cruise at or around the 200 mb level. Accordingly, much of our discussion will be based on the flow characteristics at low and high levels in the troposphere where the data base is more complete.

1.3 Field Experiments

The routine data network in the tropics is totally inadequate to allow an in-depth study of many of the important weather systems that occur there. For this reason several major field experiments and many smaller ones have been carried out to investigate particular phenomena in detail. One early data set was obtained in the Marshall Islands in 1956, and was used by Yanai *et al.* (1976) to diagnose the effects of cumulus convection in the tropics. A further experiment on the same theme, the Barbados Oceanographical and Meteorological EXperiment (BOMEX), was carried out in 1969 (Holland and Rasmussen, 1973). Several large field experiments were or-

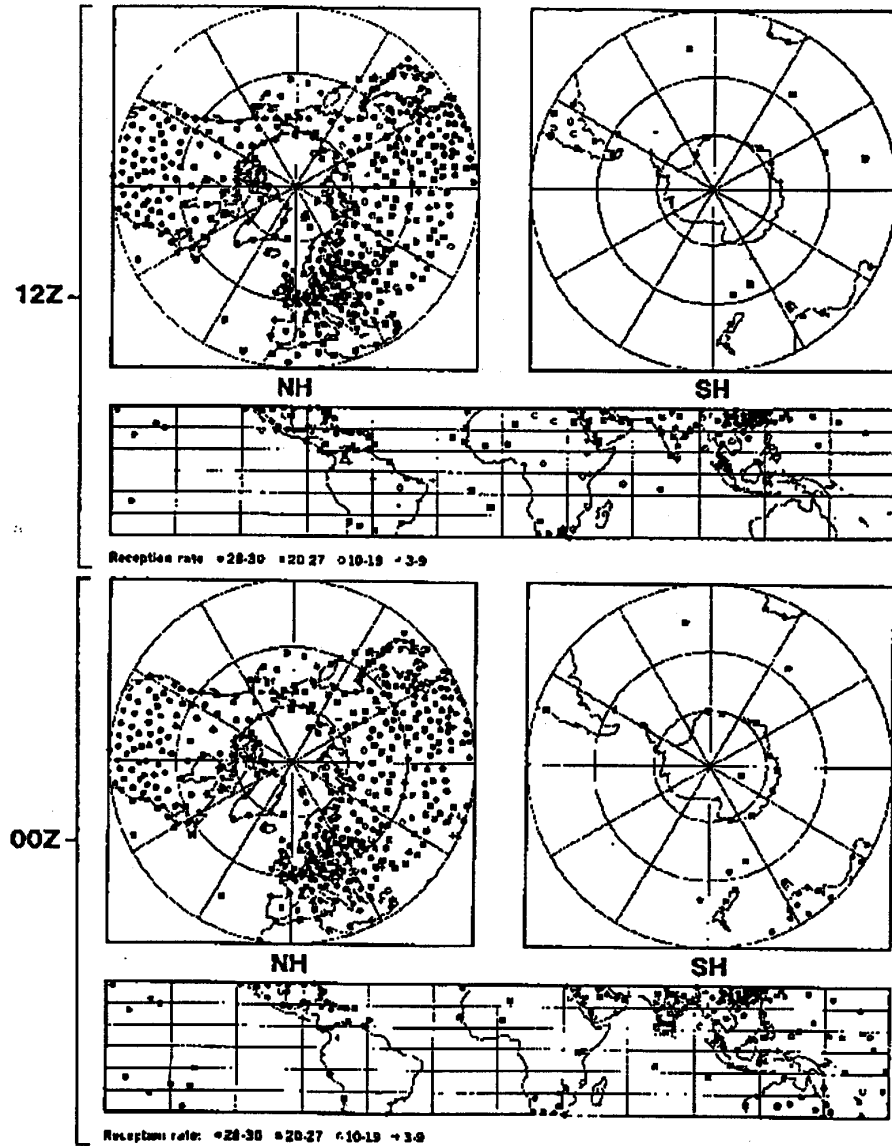


Figure 1.10: Distribution and reception rate of radiosonde ascents, from land stations, received at ECMWF during April 1984. Upper panels are for 12 UTC; lower panels for 00 UTC.

ganized under the auspices of the Global Atmospheric Research Programme (GARP), sponsored by the World Meteorological Organization - (WMO) and other scientific bodies (see Fleming *et al.*, 1979). The programme included a global experiment, code-named FGGE (The First GARP Global Experiment), which was held from December 1978 to December 1979. In turn, this included two special experiments to study the Asian monsoon and code-named MONEX (MONsoon EXperiments). The

first phase, Winter-MONEX, was held in December 1978 and focussed on the Indonesian Region (Greenfield and Krishnamurti, 1979). The second phase, Summer-MONEX, was carried out over the Indian Ocean and adjacent land area from May to August 1979 (Fein and Kuettner, 1980).

A forerunner of these experiments was GATE, the GARP Atlantic Tropical Experiment, which was held in July 1974 in a region off the coast of West Africa. Its aim was to study, *inter alia*, the structure of convective cloud clusters that make up the Inter-Tropical Convergence Zone (ITCZ) in that region (see Kuettner *et al.*, 1974).

More recently, the Australian Monsoon EXperiment (AMEX) and the Equatorial Mesoscale EXperiment (EMEX) were carried out concurrently in January-February 1987 in the Australian tropics, the former to study the large-scale aspects of the summertime monsoon in the Australian region, and the latter to study the structure of mesoscale convective cloud systems that develop within the Australian monsoon circulation. Details of the experiments are given by Holland *et al.* (1986) and Webster and Houze (1991).

The last large experiment at the time of writing was TOGA-COARE. TOGA stands for the Tropical Ocean and Global Atmosphere project and COARE for the Coupled Ocean-Atmosphere Response Experiment. The experiment was carried out between November 1992 and February 1993 in the Western Pacific region, to the east of New Guinea, in the so-called warm pool region. The principal aim was “to gain a description of the tropical oceans and the global atmosphere as a time-dependent system in order to determine the extent to which the system is predictable on time scales of months to years and to understand the mechanisms and processes underlying this predictability” (Webster and Lukas, 1992).

1.4 Macroscale circulations

Figure 1.11 shows the mean wind distribution at 850 mb and 200 mb for JJA. These levels characterize the lower and upper troposphere, respectively. Similar diagrams for DJF are shown in Fig. 1.12. At a first glance, the flow patterns show a somewhat complicated structure, but careful inspection reveals some rather general features.

At 850 mb there is a cross-equatorial component of flow towards the *summer* hemisphere, especially in the Asian, Australian and (east) African sectors. This flow, which reverses between seasons, constitutes the planetary monsoons (see §1.8). In the same sectors in the upper troposphere the flow is generally opposite to that at low levels, i.e., it is towards the winter hemisphere, with strong westerly winds (much stronger in the winter hemisphere) flanking the more meridional equatorial flow.

Both the upper and lower tropospheric flow in the Asian, Australian and African regions indicate the important effects of the land distribution in the tropics. Over the Pacific Ocean, the flow adopts a different character. At low levels it is generally eastward while at upper levels it is mostly westward. Thus the equatorial Pacific

region is dominated by motions confined to a zonal plane. Note the strong easterly flow along the Equator in the central Pacific in both seasons. These are associated with the Walker circulation discussed below.

In JJA, the upper winds near the equator are mostly easterly, rather than westerly as suggested by Fig. 1.6. This is consistent with the fact that mean position of the upward branch of the Hadley circulation lies north of the Equator and, as shown below, it is dominated by the circulation in the Asian region. In DJF, the upper winds at the Equator are generally westerly in the eastern hemisphere and westerly in the western hemisphere.

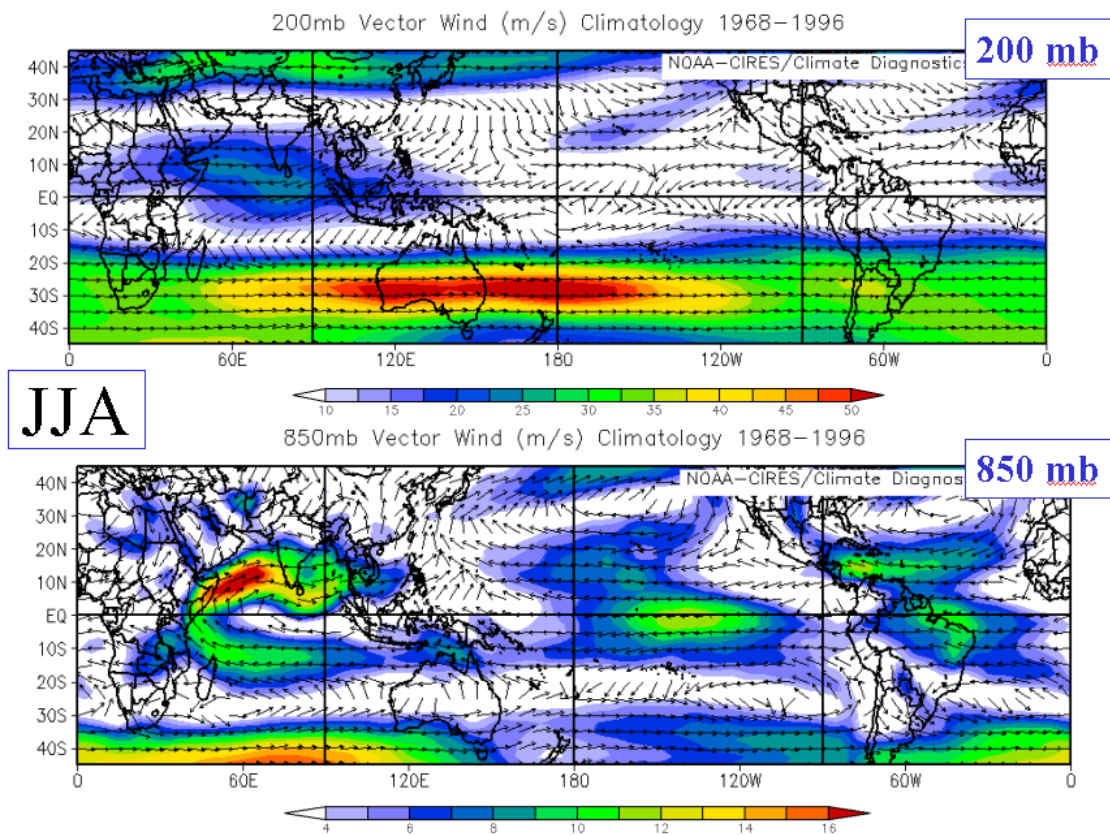


Figure 1.11: Mean wind fields at 850 mb and 200 mb during JJA (Based on NCEP Reanalysis data).

In constructing zonally-averaged charts, an enormous amount of structure is “averaged-out”. To expose some of this structure while still producing a simpler picture than the wind fields, we can separate the three-dimensional velocity field into a rotational part and a divergent part (see e.g. Holton, 1972, Appendix C). Thus

$$\mathbf{V} = \mathbf{k} \wedge \nabla\psi - \nabla\chi \quad (1.1)$$

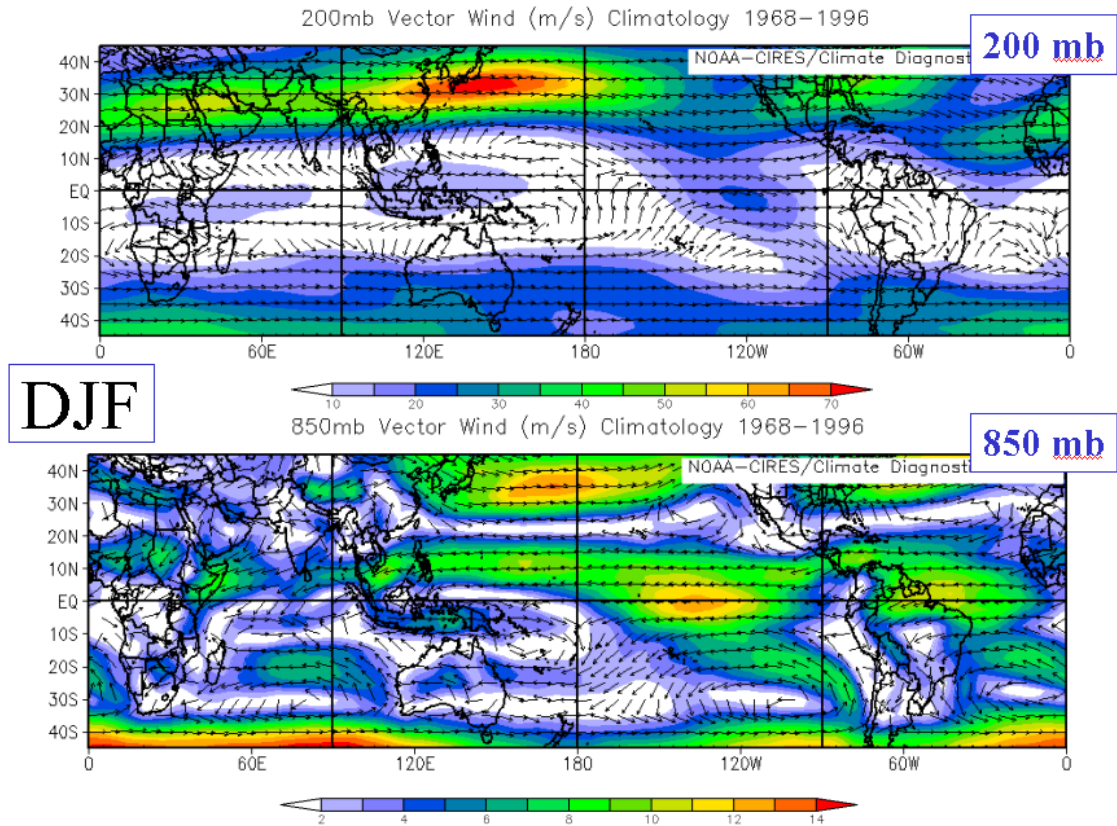


Figure 1.12: As in Fig. 1.11, but for DJF.

where ψ is a streamfunction and χ a velocity potential. The contribution $\mathbf{k} \wedge \nabla\psi$ is rotational with $\nabla \wedge (\mathbf{k} \wedge \nabla\psi) = \mathbf{k} \nabla^2\psi$, but nondivergent, whereas, $\nabla\chi$ is irrotational, but has divergence $\nabla^2\chi$. Because of this last property, examination of the velocity potential is especially useful as a diagnostic tool for isolating the divergent circulation. It is this part of the circulation which responds directly to the large-scale heating and cooling of the atmosphere.

Figure 1.13 shows the distribution of the upper-tropospheric mean seasonal velocity potential χ and arrows denoting the divergent part of the mean seasonal wind field during summer and winter. Two features dominate the picture. These are the large area of negative χ centred over southeast Asia in JJA and the equally strong negative region over Indonesia in DJF. These negative areas are located over positive χ centres at low levels (Krishnamurti, 1971, Krishnamurti *et al.*, 1973)¹. Moreover, the two areas dominate all other features.

The wind vectors indicate distinct zonal flow in the equatorial belt over the Pacific

¹Note that Krishnamurti defines χ to have the opposite sign to the normal mathematical convention used here. Accordingly, the signs in Fig. 1.13 have been changed to be consistent with our sign convention, the convention used also by the Australian Bureau of Meteorology.

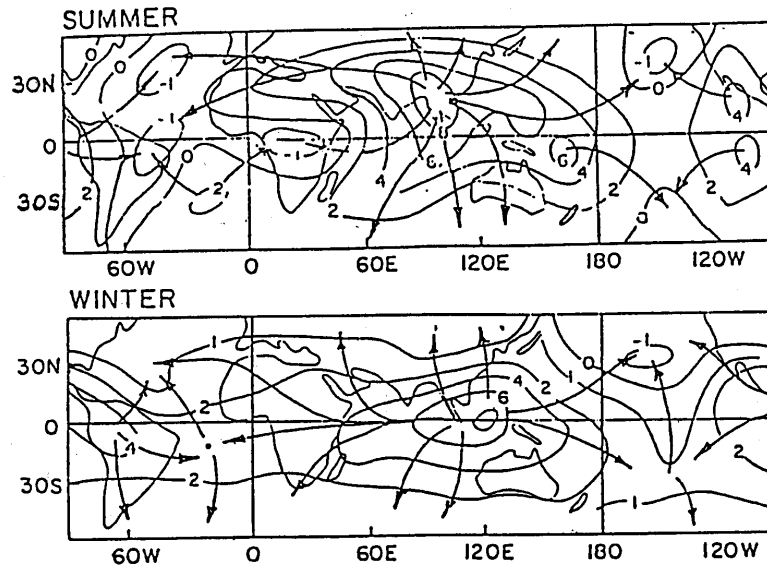


Figure 1.13: Distribution of the upper tropospheric (200 mb) mean seasonal velocity potential (solid lines) and arrows indicating the divergent part of the mean seasonal wind which is proportional to $\nabla^2\chi$. (Adapted from Krishnamurti *et al.*, 1973).

and Indian Oceans and strong meridional flow northward into Asia and southward across Australia. The meridional flow is strongest in these sectors (i.e., in regions of strongest meridionally-orientated $\nabla\chi$) and shows that the Hadley cell is actually dominated by regional flow at preferred longitudes.

When interpreting the χ -fields, a note of caution is appropriate. Remember that $\nabla \cdot V = -\nabla^2\chi$ and that $|w| \propto |\nabla \cdot V|$. Therefore centres of χ maximum or minimum do *not* coincide with centres of w maximum or minimum. The latter occur where $\nabla^2\chi$ is a maximum or minimum.

The seasonal changes in the broadscale upper-level divergence patterns indicated in Fig. 1.13 are reflected in the seasonal migration of the diabatic heat sources shown in Fig. 1.14. These heat sources are identified by regions of high cloudiness, itself characterized by regions with low values ($\approx 225 \text{ W m}^{-2}$) of outgoing long-wave radiation (OLR) measured by satellites. The assumption is that high cloudiness (cold cloud tops) arises principally from deep convection heating and can be used as a proxy for this.

Krishnamurti's arrows in Fig. 1.13 are also somewhat misleading as they refer only to the wind direction and not its magnitude. It is possible to study the flow in the equatorial belt by considering a zonal cross-section (longitude versus height) along the equator with the zonal and vertical components of velocity plotted. The mean circulation in such a cross-section is shown in Fig. 1.15. Strong ascending motion occurs in the western Pacific and Indonesian region with subsidence extending over most of the remaining equatorial belt. Exceptions are the small ascending zones

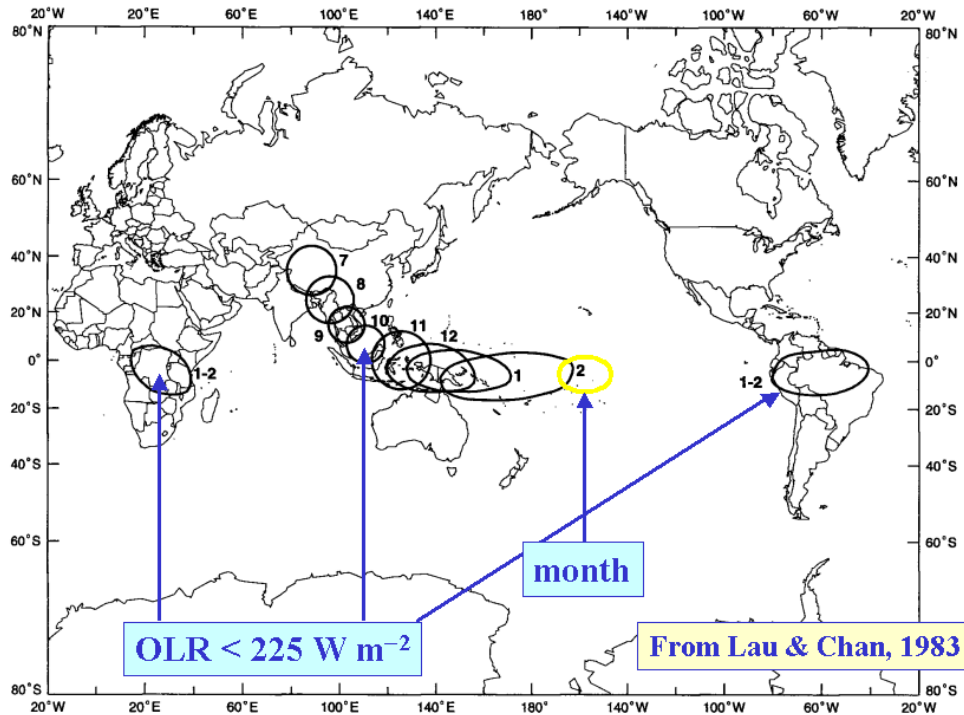


Figure 1.14: Seasonal migration of the diabatic heat sources during the latter half of the year (July-February, denoted by matching numerals). The extent of the diabatic heat sources is determined from the area with OLR values less than 225 W m^{-2} from monthly OLR climatology and is approximately proportional to the size and orientation of the schematic drawings. (Adapted from Lau and Chan 1983)

over South America and Africa. It should be noted that the Indonesian ascending region lies to the east of the velocity potential maximum in Fig. 1.13, in the area where $\nabla^2\chi$ is largest. The dominant east-west circulation is often called the *Walker Circulation*. Also plotted in Fig. 1.15 are the distributions of the pressure deviation in the upper and lower troposphere. These are consistent with the sense of the large-scale circulation, the flow being essentially down the pressure gradient.

Figure 1.15 displays significant vertical structure in the large scale velocity field. Data indicate that the tropospheric wind field possesses two extrema: one in the upper troposphere and one in the lower troposphere. A theory of tropical motions will have to account for these large horizontal and vertical scales. Indeed, it is interesting to speculate on the reason for the large scale of the structures which dominate the tropical atmosphere. Their stationary nature, *at least on seasonal time scales*, suggests that they are probably forced motions, the forcing agent being the differential heating of the land and ocean or other forms of heating resulting from it.

There is a considerable amount of observational evidence to support the heating

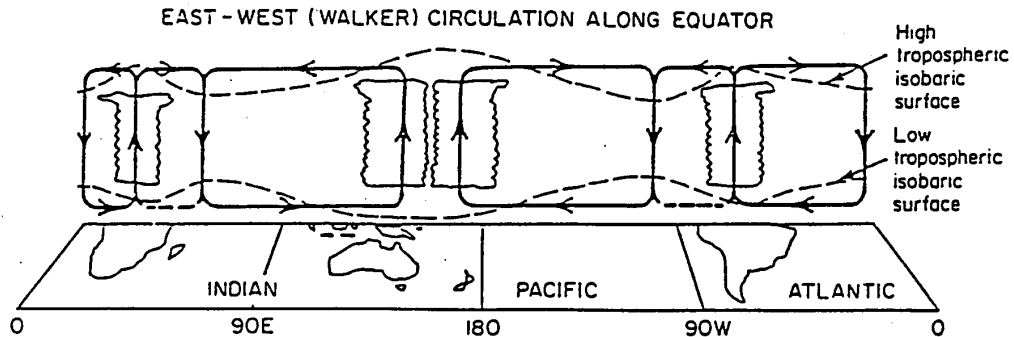


Figure 1.15: Schematic diagram of the longitude-height circulation along the equator. The surface and 200 mb pressure deviations are shown as dashed lines. Clouds indicate regions of convection. Note the predominance of the Pacific Ocean - Indonesian cell which is referred to as the Walker Circulation. (From Webster, 1983)

hypothesis. For example, Fig. 1.16 shows the distribution of annual rainfall throughout the tropics. It is noteworthy that the heaviest falls occur in the Indonesian and Southeast Asian region with a distribution which corresponds to the velocity potential field shown earlier. One is led to surmise that the common ascending branch of the Hadley cell and Walker cell is driven in some way by latent heat release. It is a separate problem to understand why the maximum latent heat release would be located in the Indonesian region. Figures 1.17 and 1.18 point to a solution. Figure 1.17 shows the distribution of mean annual surface air temperature. The pattern possesses considerable longitudinal variation, but correlates well with the sea surface temperature (SST) distribution shown in Fig. 1.18. Of great importance is the 8-10°C longitudinal temperature gradient across the Pacific Ocean. The air mass over the western Pacific should be much more unstable to convection than that overlying the cooler waters of the eastern Pacific.

It is important to remember that the seasonal or annual mean fields shown above possess both temporal and spatial variations on even longer time scales (see section 1.6). Figure 1.19 shows the mean annual temperature range of the air near sea level. It is significant that in the equatorial belt, the temperature variations are generally very small, perhaps an order of magnitude smaller than those observed at higher latitudes. This is true for both land and sea areas. We may conclude that the variations with longitude shown earlier will be maintained. On the other hand, at higher latitudes, the near surface temperature over the sea possesses a relatively large amplitude variation which is surpassed only by the temperature variation over land. Figure 1.19 shows only the amplitude of the variation and gives no details of its phase. In fact, the ocean temperature at higher latitudes lags the insolation by some 2 months. Continental temperatures lag by only a few weeks.

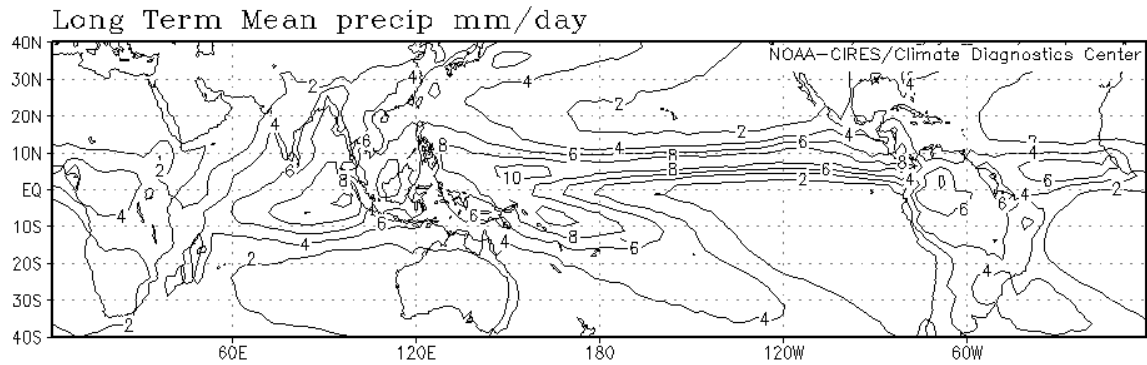


Figure 1.16: Distribution of annual rainfall in the tropics. Contour values marked in cm/day.

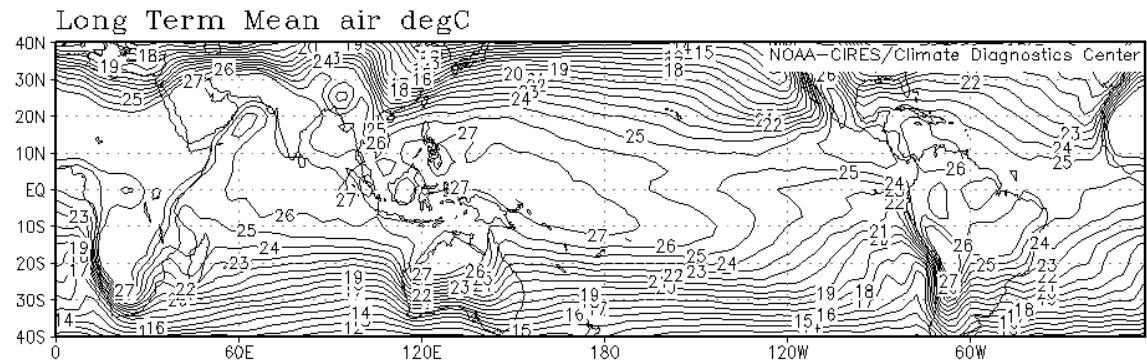


Figure 1.17: Mean annual surface air temperature in the tropics (Units °C).

1.5 More on the Walker Circulation

Figure 1.20 shows a closer view of the Walker circulation with ascent over the warm pool region and subsidence over the cooler waters of the eastern Pacific. Over the Pacific the flow is easterly at low levels and westerly at upper levels. The term “Walker Circulation” appears to have been first used by Bjerknes (1969) to refer to the overturning of the troposphere in the quadrant of the equatorial plane spanning the Pacific Ocean and it was Bjerknes who hypothesized that the “driving mechanism” for this overturning is condensational heating over the far western equatorial Pacific where SSTs are anomalously warm. The implication is that the source of precipitation associated with this driving mechanism is the local evaporation associated with the warm SSTs. This assumption was questioned by Cornejo-Garrido and Stone (1977) who showed on the basis of a budget study that the latent heat release driving the Walker Circulation is negatively-correlated with local evaporation, whereupon moisture convergence from other regions must be important. Newell *et al.* (1974) defined the Walker Circulation as the deviation of the circulation in the

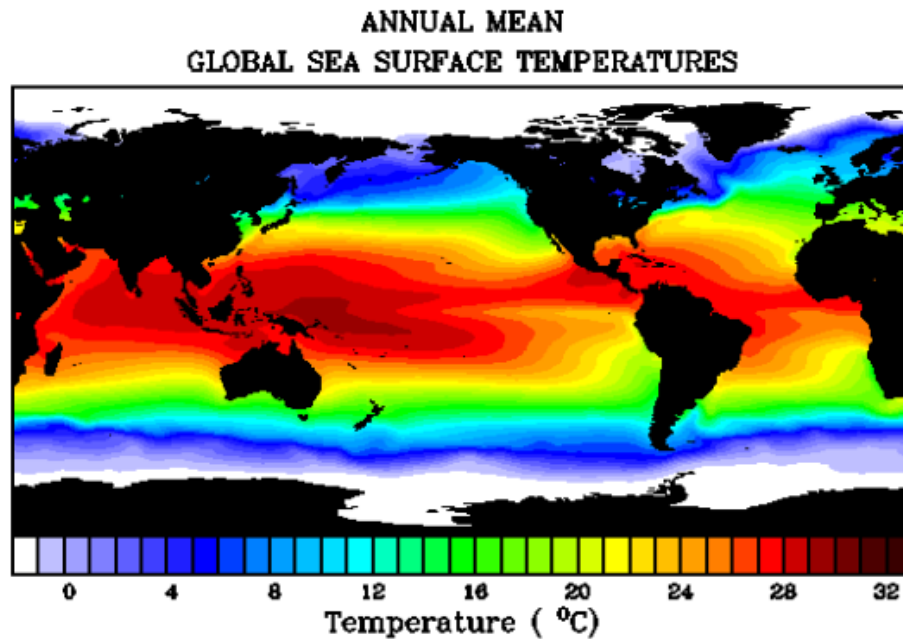


Figure 1.18: Annual mean sea surface temperature in the tropics.

equatorial plane from the zonal average. Figure 1.21, taken from Newell *et al.*, shows the contours of zonal mass flux averaged over the three month period December 1962 - February 1963 in a 10°S wide strip centred on the equator. In this representation there are five separate circulation cells visible around the globe, but the double cell whose upward branch lies over the far western Pacific is the dominant one. A similar diagram for the northern summer period June to August (Fig. 1.21(b)) shows only three cells, but again the major rising branch lies over the western Pacific. As we shall see, the circulation undergoes significant fluctuations on both interannual (1.6) and intraseasonal (1.7) time scales.

1.6 El Niño and the Southern Oscillation

There is considerable interannual variability in the scale and intensity of the Walker Circulation, which is manifest in the so-called *Southern Oscillation* (SO). The latter is associated with fluctuations in sea level pressure in the tropics, monsoon rainfall, and the wintertime circulation over the Pacific Ocean. It is associated also with fluctuations in circulation patterns over North America and other parts of the extratropics. Indeed, it is the single most prominent signal in year-to-year climate variability in the atmosphere. The SO was first described in a series of papers in the 1920s by Sir Gilbert Walker (Walker, 1923, 1924, 1928) and a review and references are contained in a paper by Julian and Chervin (1978). The latter authors use Walkers own words to summarize the phenomenon. “By the southern oscillation is

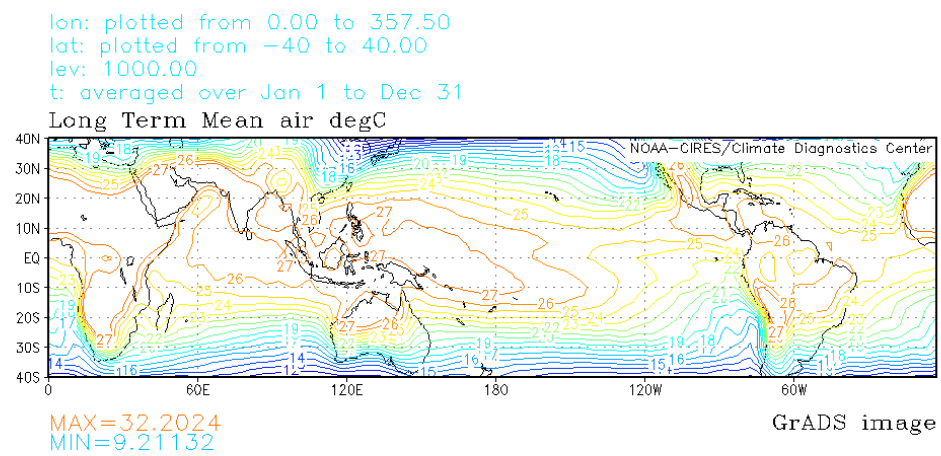


Figure 1.19: Mean annual temperature range ($^{\circ}\text{C}$) of the air near sea level.

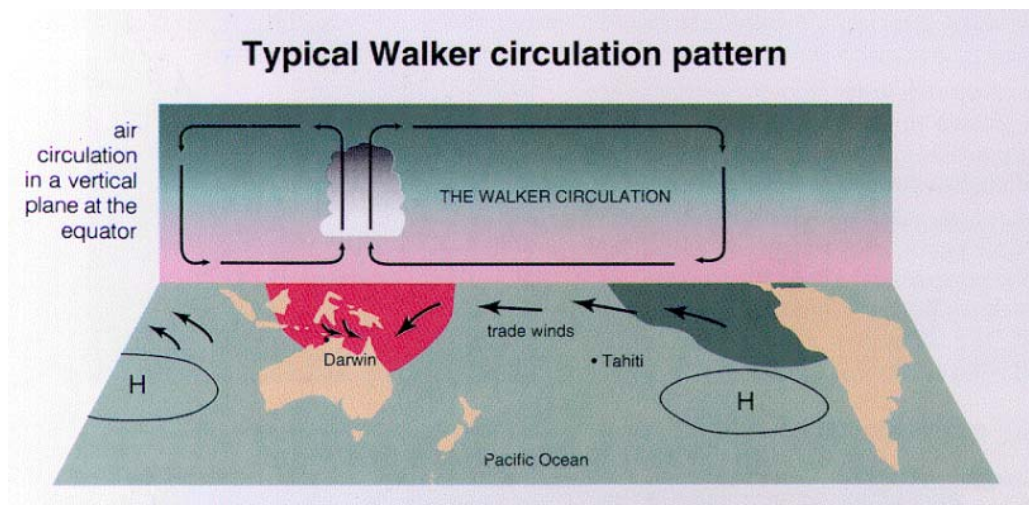


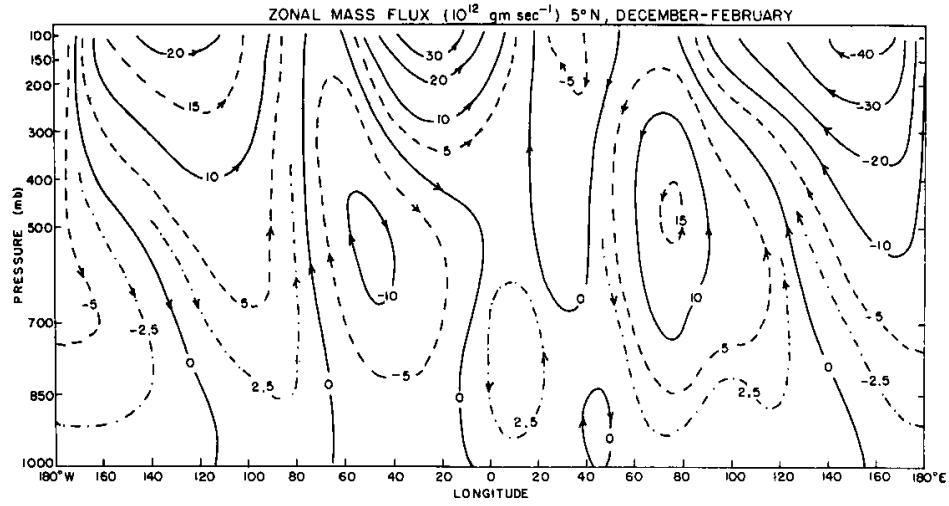
Figure 1.20: A close-up view of the Walker circulation showing ascent over the warm pool region and subsidence over the cooler waters of the eastern Pacific. The flow is easterly at low levels and westerly at upper levels.

implied the tendency of (surface) pressure at stations in the Pacific (San Francisco, Tokyo, Honolulu, Samoa and South America), and of rainfall in India and Java... to increase, while pressure in the region of the Indian Ocean (Cairo, N.W. India, Darwin, Mauritius, S.E. Australia and the Cape) decreases..." and "We can perhaps best sum up the situation by saying that there is a swaying of pressure on a big scale backwards and forwards between the Pacific and Indian Oceans..."

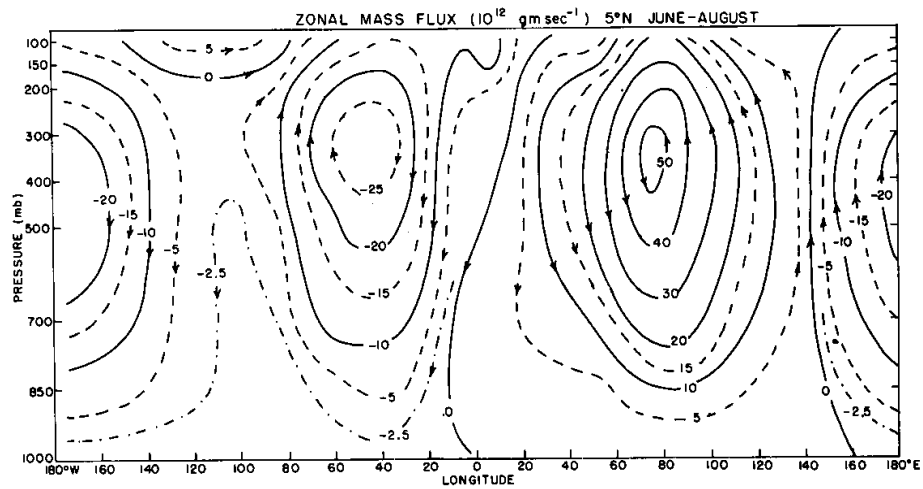
Figure 1.22a depicts regions of the globe affected by the SO. It shows the simultaneous correlation of surface pressure variations at all places with the Darwin surface pressure. It is clear, indeed, that the "sloshing" back and forth of pressure which characterizes the SO does influence a very large area of the globe and that the "centres of action", namely Indonesia and the eastern Pacific, are large also. Figure 1.22b shows the variation of the normalized Tahiti-Darwin pressure anomaly difference, frequently used as a Southern Oscillation Index (SOI), which gives an indication of the temporal variation of the phase of the SO. For example, a positive SOI means that pressures over Indonesia are relatively low compared with those over the eastern Pacific and vice versa.

It was Bjerknes (1969) who first pointed to an association between the SO and the Walker Circulation, although the seeds for this association were present in the investigations by Troup (1965). These drew attention to the presence of interannual changes in the upper troposphere flow over the tropics associated with the SO and indicated that the anomalies in the flow covered a large range of longitudes. Bjerknes stated:

"The Walker Circulation... must be part of the mechanism of the still larger 'Southern Oscillation' statistically defined by Sir Gilbert Walker... whereas



(a)



(b)

Figure 1.21: Deviations of the zonal mass flux, averaged over the latitude belt 0° - 10° N, from the zonal mean, for the periods (a) December - February, and (b) June - August calculated by Newell *et al.* (1974). Contours do not correspond with streamlines, but give a fairly good representation of the velocity field associated with the Walker Circulation.

the Walker Circulation maintains east-west exchange of air covering a little over an earth quadrant of the equatorial belt from South America to

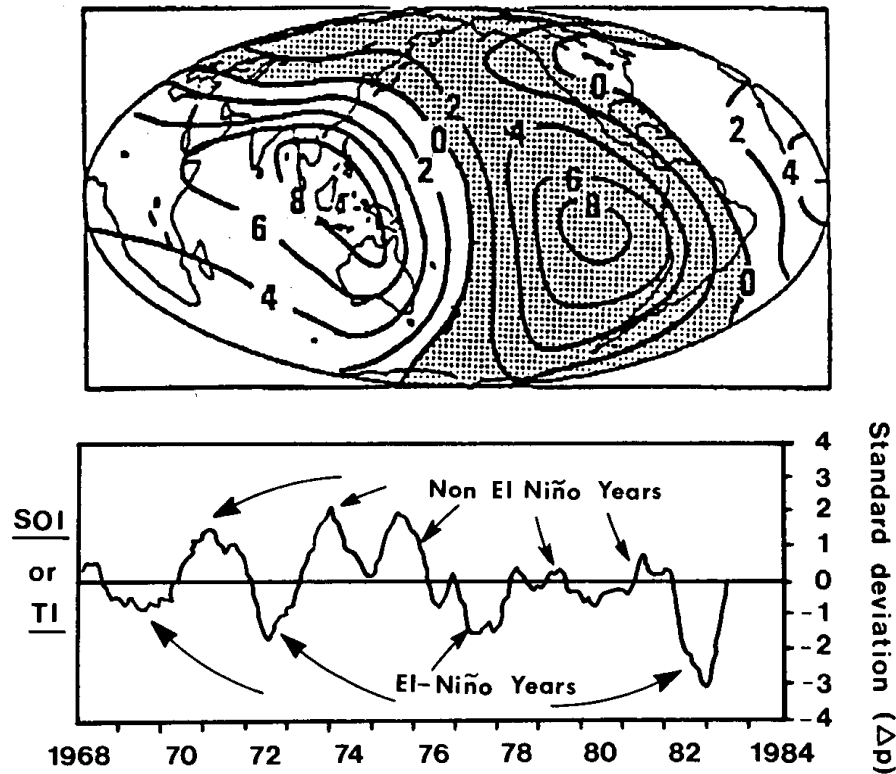


Figure 1.22: The spatial variation of the simultaneous correlation of surface pressure variations at all points with the Darwin surface pressure (upper panel). Shaded areas show negative correlations. The lower panel shows the variation of the normalized Tahiti-Darwin pressure difference on the Southern Oscillation Index. (From Webster, 1987b)

the west Pacific, the concept of the Southern Oscillation refers to the barometrically-recorded exchange of mass along the complete circumference of the globe in tropical latitudes. What distinguishes the Walker Circulation from other tropical east-west exchanges of air is that it operates a large tapping of potential energy by combining the large-scale rise of warm-moist air and descent of colder dry air”.

In a subsequent paper, Bjerknes (1970) describes this thermally-direct circulation oriented in a zonal plane by reference to mean monthly wind soundings at opposing “swings” of the SO and the patterns of ocean temperature anomalies.

El Niño is the name given to the appearance of anomalously warm surface water off the South American coast, a condition which leads periodically to catastrophic downturns in the Peruvian fishing industry by severely reducing the catch. The colder water that normally upwells along the Peruvian coast is rich in nutrients, in contrast to the warmer surface waters during *El Niño*. The phenomenon has been

the subject of research by oceanographers for many years, but again it seems to have been Bjerknes (1969) who was the first to link it with the SO as some kind of air-sea interaction effect. Bjerknes used satellite imagery to define the region of heavy rainfall over the zone of the equatorial central and eastern Pacific during episodes of warm SSTs there. He showed that these fluctuations in SST and rainfall are associated with large-scale variations in the equatorial trade wind systems, which in turn affect the major variations of the SO pressure pattern. The fluctuations in the strength of the trade winds can be expected to affect the ocean currents, themselves, and therefore the ocean temperatures to the extent that these are determined by the advection of cooler or warmer bodies of water to a particular locality, or, perhaps more importantly to changes in the pattern of upwelling of deeper and cooler water.

Figure 1.23 shows time-series of various oceanic and atmospheric variables at tropical stations during the period 1950 to 1973 taken from Julian and Chervin (1978). These data include the strength of the South Equatorial Current; the average SST over the equatorial eastern Pacific; the Puerto Chicama (Peru) monthly SST anomalies; the 12 month running averages of the Easter Island-Darwin differences in sea level pressure; and the smoothed Santiago-Darwin station pressure differences. The figure shows also the zonal wind anomalies at Canton Island (3°S , 172°W) which was available for the period 1954-1967 only. The mutual correlation and particular phase association of these time series is striking and indicate an atmosphere-ocean coupling with a time scale of years and a spatial scale of tens of thousands of kilometres involving the tropics as well as parts of the subtropics. This coupled ocean-atmosphere phenomenon is now referred to as ENSO, an acronym for *El Niño-Southern Oscillation*.

During El Niño episodes, the equatorial waters in the eastern half of the Pacific are warmer than normal while SSTs west of the date line are near or slightly below normal. Then the east-west temperature gradient is diminished and waters near the date line may be as warm as those anywhere to the west ($\sim 29^{\circ}\text{C}$). The region of heavy rainfall, normally over Indonesia, shifts eastwards so that Indonesia and adjacent regions experience drought while the islands in the equatorial central Pacific experience month after month of torrential rainfall. Near and to the west of the date line the usual easterly surface winds along the equator weaken or shift westerly (with implication for ocean dynamics), while anomalously strong easterlies are observed at the cirrus cloud level. In essence, in the atmosphere there is an eastward displacement of the Walker Circulation.

There are various theories for the oceanic response to changes in the atmospheric circulation, but as yet none is widely accepted as the correct one. A brief review of these is given by Hirst (1989). A popular style review of the meteorological aspects of ENSO is given by Rasmussen and Wallace (1983), who discuss, *inter alia*, the implications of ENSO for circulation changes in middle and higher latitudes. A more recent review is that of Philander (1990).

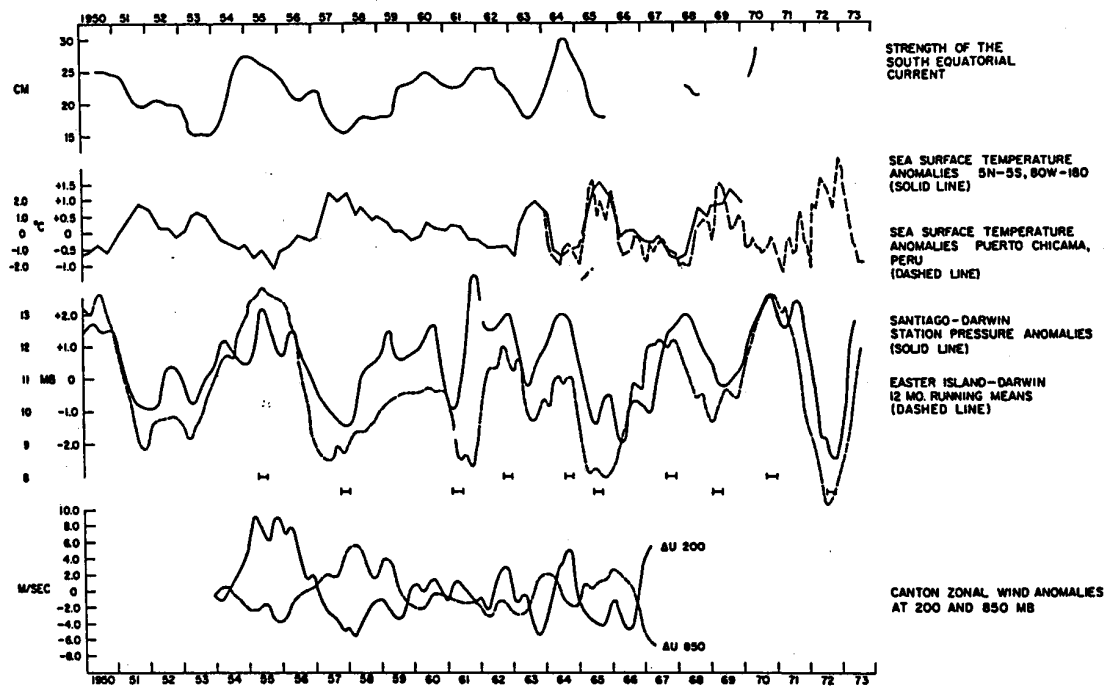


Figure 1.23: Composite low-pass filtered time series for various oceanographic and meteorological parameters involved in the Southern Oscillation and Walker-Circulation. Series are (top to bottom): the strength of the South Equatorial Current, a westward flowing current just south of the equator; ocean surface temperature anomalies in the region 5°N - 5°S and 80°W to 180°W (solid line), and monthly anomalies of Puerto Chicama ocean surface temperature, dashed; two Southern Oscillation indices, the dashed line being 12-month running means of the difference in station pressure Easter Island-Darwin and the solid line being a similar quantity except Santiago is used instead of Easter Island; the bottom series are low-pass filtered zonal wind anomalies (from monthly means) at Canton at 850 mb (dashed) and 200 mb (solid). The short horizontal marks appearing between two panels denote the averaging intervals used in compositing variables in cold water and El Niño situations. (From Julian and Chervin, 1978)

1.7 The Madden-Julian/Intraseasonal Oscillation

As well as fluctuations on an interannual basis, the Walker Circulation appears to undergo significant fluctuations on intraseasonal time scales. This discovery dates back to pioneering studies by Madden and Julian (1971, 1972) who found a 40-50 day oscillation in time series of sea-level pressure and rawinsonde data at tropical stations. They described the oscillation as consisting of global-scale eastward-propagating zonal circulation cells along the equator. The oscillation appears to be

associated with intraseasonal variations in tropical convective activity as evidenced in time series of rainfall and in analyses of anomalies in cloudiness and OLR.

The results of various studies to the mid-80s are summarized by Lau and Peng (1987). They list the key features of the intraseasonal variability as follows:

- i. There is a predominance of low-frequency oscillations in the broad range from 30-60 days;
- ii. The oscillations have predominant zonal scales of wavenumbers 1 and 2 and propagate eastward along the equator year-round.
- iii. Strong convection is confined to the equatorial regions of the Indian Ocean and western Pacific sector, while the wind pattern appears to propagate around the globe.
- iv. There is a marked northward propagation of the disturbance over India and East Africa during summer monsoon season and, to a lesser extent, southward penetration over northern Australia during the southern summer.
- v. Coherent fluctuations between extratropical circulation anomalies and the tropical 40-50 day oscillation may exist, indicating possible tropical-midlatitude interactions on the above time scale.
- vi. The 40-50 day oscillation appears to be phase-locked to oscillations of 10-20 day periods over India and the western Pacific. Both are closely related to monsoon onset and break conditions over the above regions.

Figure 1.24 shows a schematic depiction of the time and space variations of the circulation cells in a zonal plane associated with the 40-50 day oscillation as envisaged by Madden and Julian (1972).

Figure 1.25 shows the eastward propagation of the 40-50 day wave in terms of its velocity potential in the Eastern Hemisphere. The four panels, each separated by five days, show the distributions of the velocity potential at 850 mb. The centre of the ascending (descending) region of the wave is denoted by A (B). As the wave moves eastwards, it intensifies as shown by the increased gradient. Furthermore, and very important, as centre A moves eastwards from the southwest of India (which lies between 70°E and 90°E) to the east of India, the direction of the divergent wind over India changes from easterly to westerly. Notice also that as centre A moves across the Indian region that the gradient of velocity potential intensifies to the north as indicated by the movement of the stippled regions in panels 2 and 3. Thus, depending on where the centres A and B are located relative to the monsoon flow, the strength of the monsoon southwesterlies flowing towards the heated Asian continent will be strengthened or weakened. Thus we can see the importance of the phase of the MJO on the mean monsoonal flow.

According to Lau and Peng, the most fundamental features of the oscillation are the perennial eastward propagation along the equator and the slow time scale in the

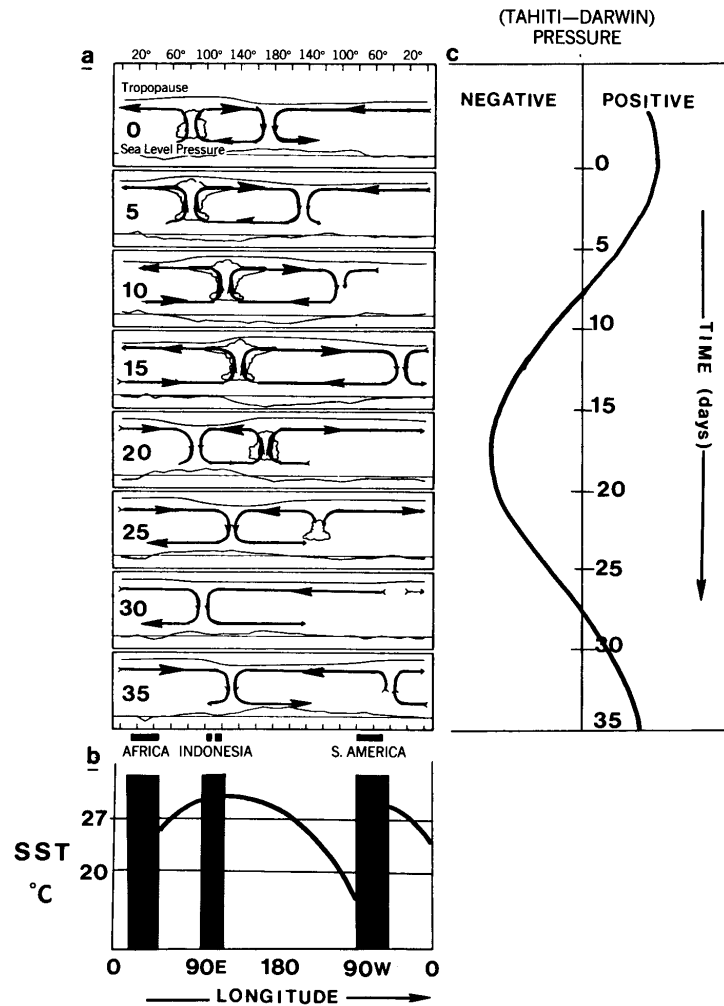


Figure 1.24: (a) Schematic depiction of the time and space variations of the disturbance associated with the 40-50 day oscillation along the equator. The times of the cycles (days) are shown to the left of the panels. Clouds depict regions of enhanced large-scale convection. The mean disturbance pressure is plotted at the bottom of each panel. The circulation on days 10-15 is quite similar to the Walker circulation shown in Fig. 1.15. The relative tropopause height is indicated at the top of each panel. (b) shows the mean annual SST distribution along the equator. The 40-50 day wave appears strongly convective when the SST is greater than 27°C as in panels 2-5 in (a). Panel (c) shows the variations of pressure difference between Darwin and Tahiti. The swing is reminiscent of the SO, but with a time scale of tens of days rather than years. (From Webster, 1987b)

range 30-60 days. To date, observational knowledge of the phenomenon has outpaced theoretical understanding, but it would appear that the equatorial wave modes to be discussed in Chapter 3 play an important role in the dynamics of the oscillation.

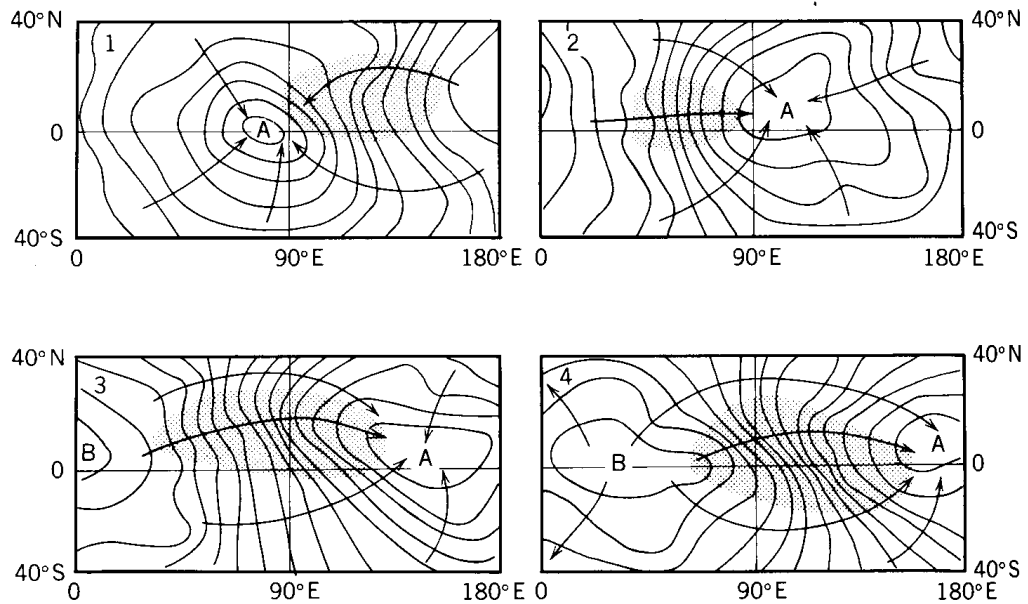


Figure 1.25: (a) The latitude-longitude structure of the 40-50 day wave in the Eastern Hemisphere in terms of 850 mb velocity potential. Units 10^{-6} s^{-1} . The arrows denote the direction of the divergent part of the wind and the stippled region the locations of maximum speed associated with the wave. Letters A and B depict the centres of velocity potential, which are seen to move eastwards. Centre A may be thought of as a region of rising air and B a region of subsidence. (From Webster 1987b)

Furthermore, because of the similar spatial and relative temporal evolution of atmospheric anomalies associated with the 40-50 day oscillation and those with ENSO, it is likely that the two phenomena are closely related (see. e.g. Lau and Chan, 1986). Indeed, one might view the atmospheric part of the ENSO cycle as fluctuations in a longer-term (e.g. seasonal average of the MJO). Two recent observational studies of the MJO are those of Knutson *et al.*, (1986) and Knutson and Weickmann (1987). A recent review of theoretical studies is included in the paper by Bladé and Hartmann (1993) and a recent reviews of observational studies are contained in papers by Madden and Julian (1994) and Yanai *et al.* (2000).

One might view the Walker Circulation as portrayed in Figs. 1.15 and 1.21 as an average of several cycles of the MJO.

1.8 More on Monsoons

The term monsoon originates from the Arabic “Mausim”, a season, and was used to describe the change in the wind regimes as the northeasterlies retreated to be replaced by the southwesterlies or vice versa. The term will be used here to describe

the westerly air stream (southwesterly in the NH, northwesterly in the SH) that results as the trade winds cross the equator and flow into the equatorial trough. Accordingly, the term refers to the *wind* regime and not to areas of continuous rain etc., which are associated with the monsoon. Figure 1.27 shows the typical low-level flow and other smaller scale features associated with the (NH) summer and winter monsoons in the Asian regions.

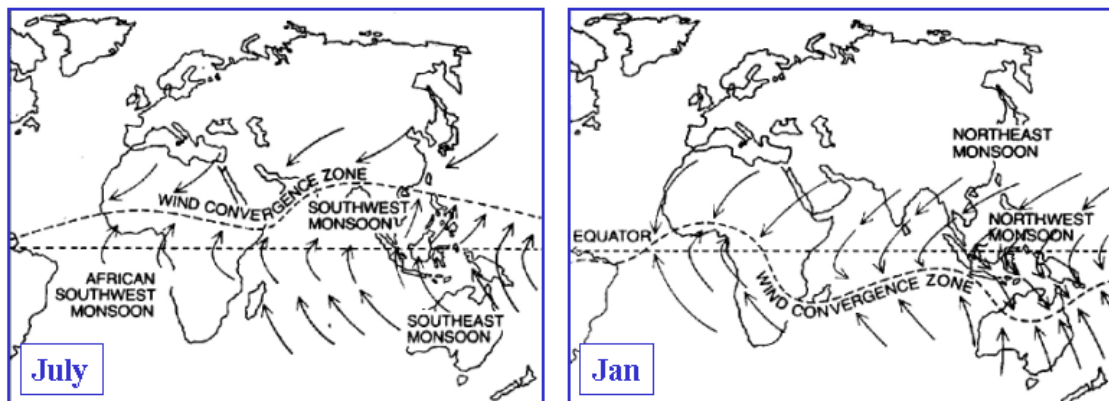


Figure 1.26: Schematic of low-level air flow patterns near the Equator in January and July showing the main regions of cross equatorial flow in the monsoon regions.

Two main theories have been advanced to account for the monsoonal perturbations.

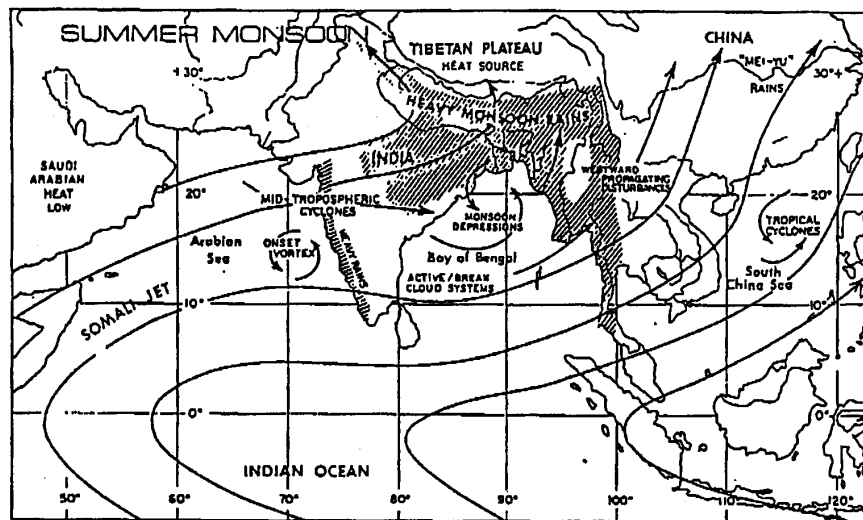
1.8.1 The Regional Theory

This regards the monsoon perturbations as low-level circulation changes resulting entirely from the large-scale heating and cooling of the continents relative to oceanic regions. In essence the monsoon is considered as a continental scale “sea breeze” where air diverges away from the cold winter continents and converges into the heat lows in the hot summer continents. The flow at higher levels is assumed to play a minor role.

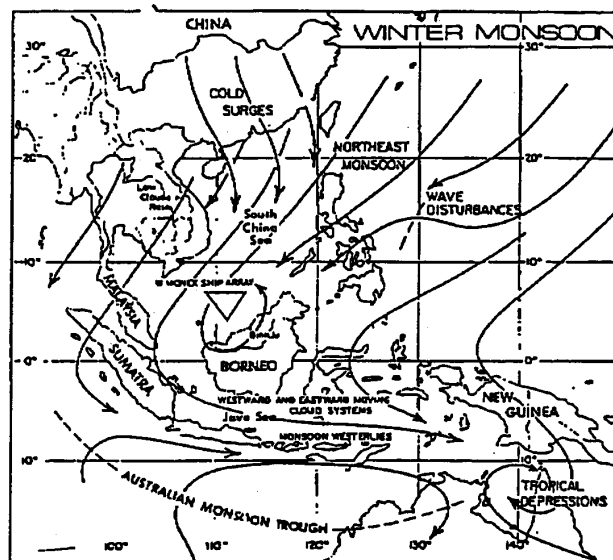
1.8.2 The Planetary Theory

With the great increase in upper air observations during the second half of this century, marked changes in the upper tropospheric flow patterns have been found to accompany the onset of monsoonal conditions in the lower levels. In particular, marked changes in the position of the subtropical jet stream accompany the advance of the monsoonal winds.

There are several objections to the regional theory. For example, monsoonal circulations are observed over the oceans, well removed from any land mass, and the



(a)



(b)

Figure 1.27: Air flow patterns and primary synoptic- and smaller scale features that affect cloudiness and precipitation in the region of (a) the summer monsoon, and (b) the winter monsoon. In (a), locations of June to September rainfall exceeding 100 cm the land west of 100°E associated with the southwest monsoon are indicated. Those over water areas and east of 100°E are omitted. In (b) the area covered by the ship array during the winter MONEX experiment is indicated by an inverted triangle. (From Houze, 1987)



heat low over the continents is often remote from the main monsoonal trough. Moreover, the seasonal displacement of surface and upper air features is well established from mean wind charts. This displacement is on a global scale, but is greatest over

the continental land masses, especially the extensive Asian continent. Hence an understanding of planetary circulation changes in conjunction with major continental perturbations is necessary in understanding the details of the monsoonal flow.

1.9 Monsoon variability

Superimposed upon the seasonal cycle are significant variations in the weather of the tropical regions. For example, in the monsoon regions the established summer monsoon undergoes substantial variations, vacillating between extremely active periods and distinct “lulls” in precipitation. The latter are referred to as “monsoon breaks”.

An example of this form of variability is shown in Fig 1.28 which summarizes the monsoon rains of two years, 1963 and 1971, along the west coast of India. The “active periods” are associated with groups of disturbances and the “breaks” with an absence of them. Usually, during the break, precipitation occurs far to the south of India and also to the north along the foothills of the Himalaya. Such variability as this appears characteristic of the precipitating regions of the summer and winter phases of the Asian monsoon and the African monsoon.

1.10 Synoptic-scale disturbances

The individual disturbances of the active monsoon and those associated with the near-equatorial troughs move westward in a fairly uniform manner. Such movement is shown clearly in Fig. 1.29. The westward movement is apparent in the bands of cloudiness extending diagonally from right to left across the time-longitude sections.

To illustrate the structure of propagating disturbances, Webster (1983) discusses a particular example taken from Winter-MONEX) in 1978. Figure 1.30 shows the Japanese geostationary satellite (GMS) infra-red (IR) satellite picture at 1800 UTC on 25 December 1978 for the Winter-MONEX region with the 2300 UTC surface pressure analysis underneath. Figure 1.31 shows the corresponding wind fields at 250 mb and 950 mb. What is striking is the existence of significant structures in the satellite cloud field which have no obvious signature in the surface pressure field. Indeed, the tropical portion of the pressure field is relatively featureless, except for the heat low in north-western Australia and the broad trough that spans the near equatorial region of the southern hemisphere just west of the date line. The most that one can say is that the major cloud regions appear to reside about the axis of a broad equatorial trough.

Webster considers three major regions of deep high cloudiness denoted by A, B and C which appear to be synoptic scale disturbances. He shows that these can be associated with areas of low-level convergence in the 950 mb wind field lying beneath areas of upper-level divergence at 200 mb. The implication is that these are each deep divergent systems. Such properties: lower tropospheric convergence, deep penetrative convection and upper-level divergence appear characteristic of the

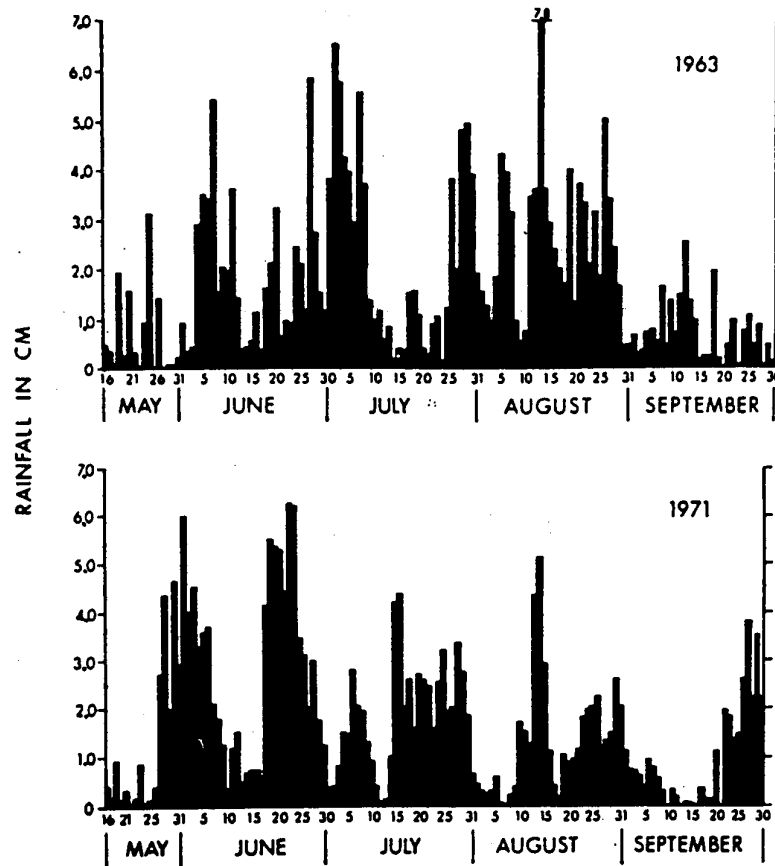


Figure 1.28: Daily rainfall (cm/day) along the western coast of India incorporating the districts of Kunkan, Coastal Mysore and Kerala for the summers of 1963 and 1971. (From Webster, 1983)

synoptic-scale tropical disturbances of the ITCZ and the major convective zones of the monsoon.

Figure 1.32 shows the surface pressure trace for Darwin from 23 - 28 December 1978, covering the period of the case study presented in Figs. 1.29 and 1.30. The major variation in the pressure is associated with the semi-diurnal oscillation which has an amplitude of about 4 mb. Little alteration to the semi-diurnal trend is apparent near 25 December 1978 which coincides with the existence there of the disturbance. Indeed at low latitudes only on rare occasions with the passage of a tropical cyclone will the synoptic-scale pressure perturbations be larger than the semi-diurnal variation.

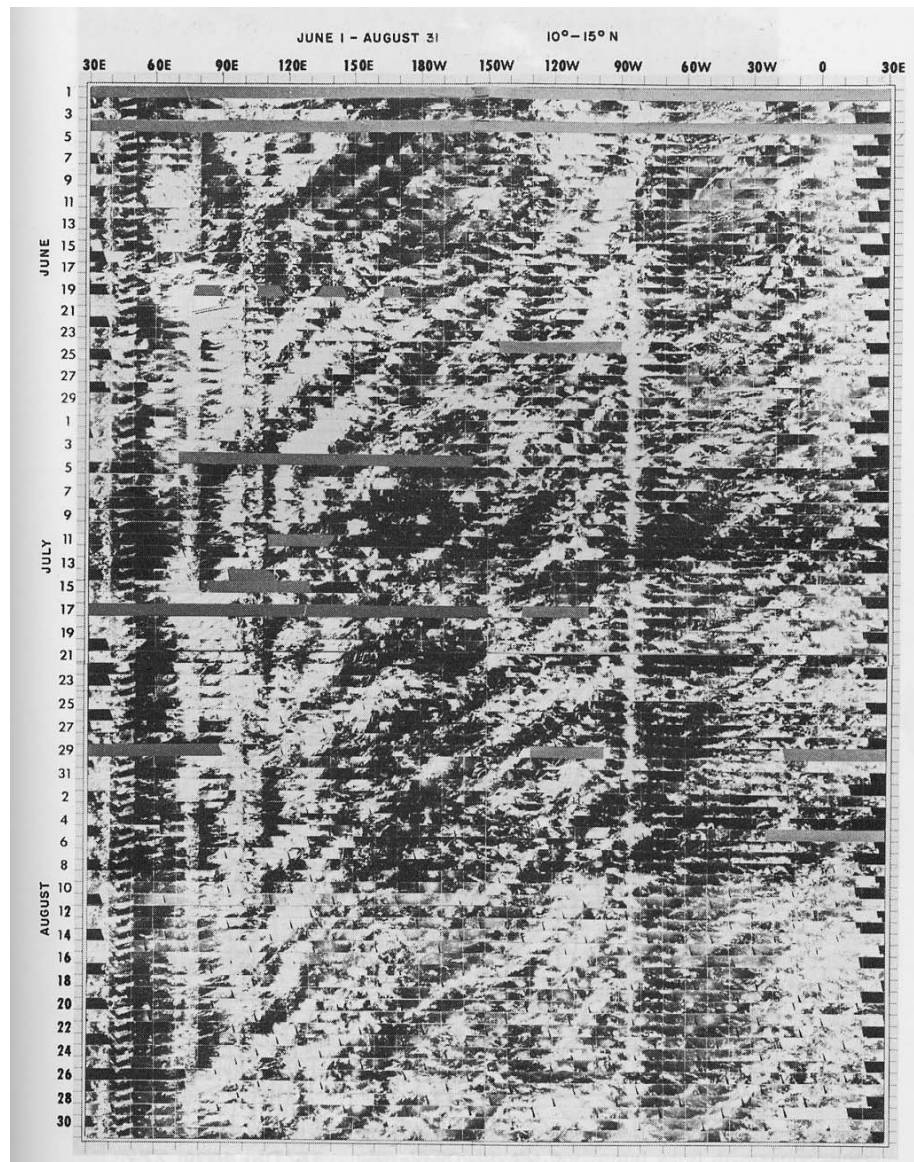


Figure 1.29: Time-longitude section of visible satellite imagery for the latitude band 10° - 15° N of the tropics. Cloud streaks moving from right to left with increasing time denotes westward propagation. Note that there is typically easterly flow at these latitudes. (From Wallace, 1970)

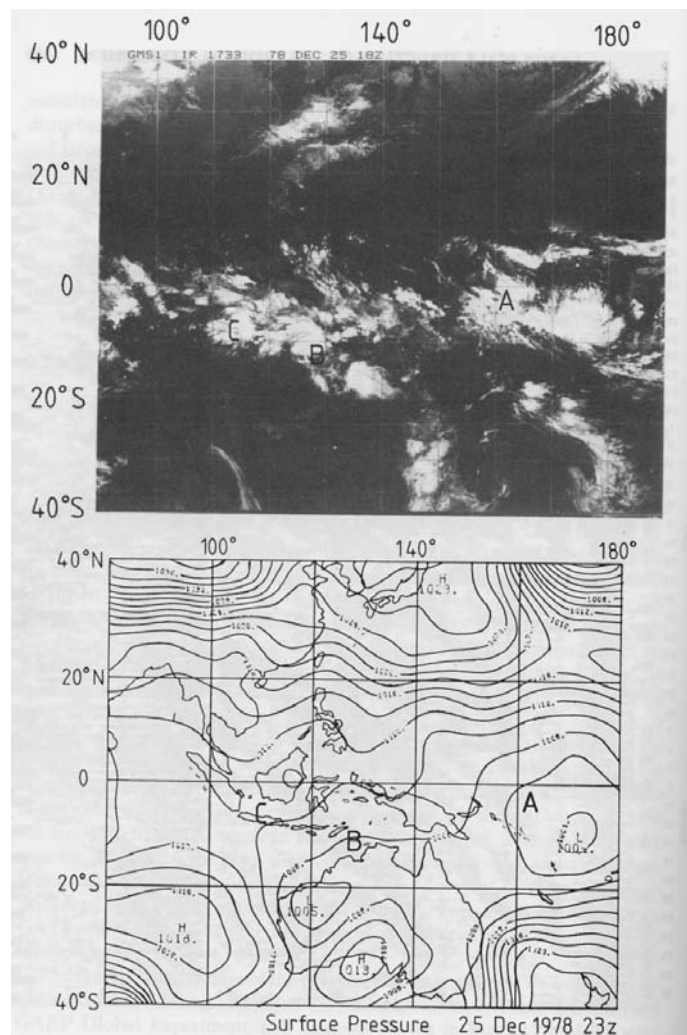


Figure 1.30: The winter MONEX region of 25 December 1978. Upper panel shows the GMS IR satellite picture with the surface-pressure pattern shown on lower panel. Both panels are on the same projection. Pressure analysis after McAvaney *et al.* (1981): Letters A, B and C identify synoptic-scale disturbances referred to in the text. (From Webster, 1983)

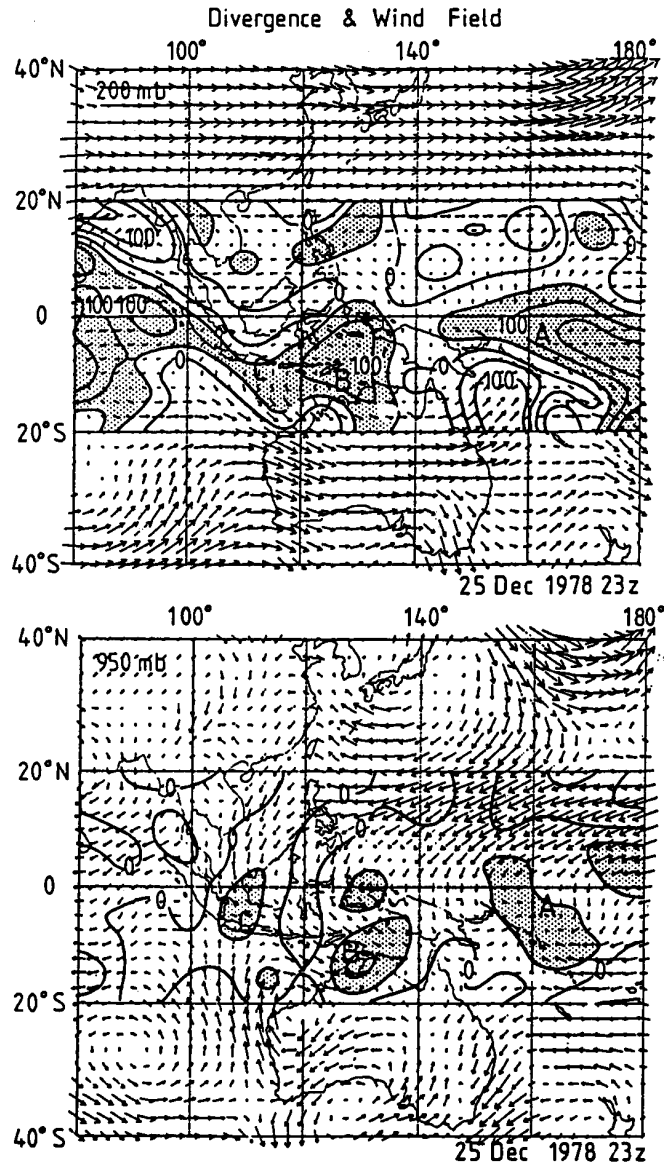


Figure 1.31: The 250 mb (upper panel) and 950 mb (lower panel) wind fields for the winter MONEX region of 25 December 1978 with the horizontal wind divergence superimposed in the 20°N - 20°S latitude strip. In the upper troposphere areas the divergence are stippled whereas in the lower troposphere areas of convergence are stippled. Stippled areas denote divergence magnitudes greater than $50 \times 10^{-5} s^{-1}$. (From Webster, 1983)

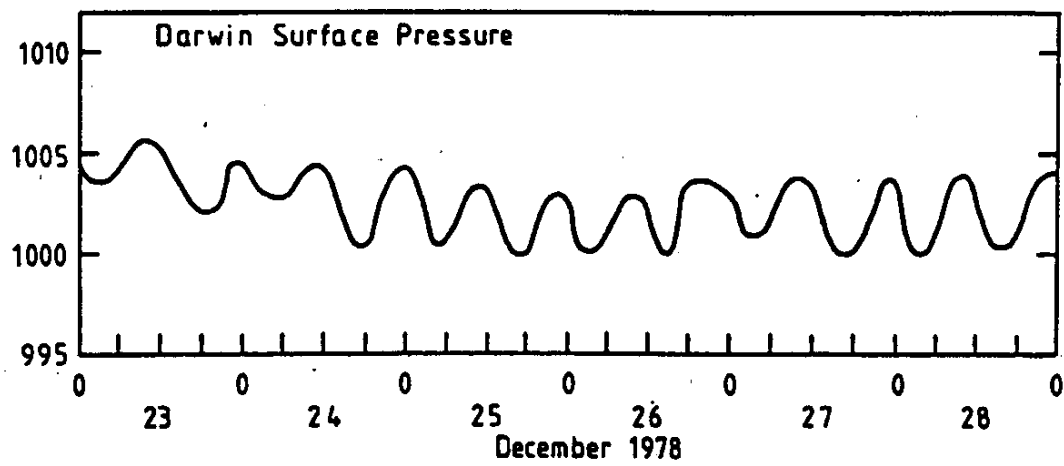


Figure 1.32: The variation of surface pressure at Darwin for the period 23 - 28 December 1978. The structure is dominated by the semi-diurnal atmospheric tide.

Chapter 2

EQUATIONS AND SCALING AT LOW LATITUDES

The governing equations of atmospheric and oceanic motion are intrinsically complicated, a reflection of the myriad of time and space scales they represent. Therefore, in order to study a specific phenomenon it is desirable to simplify the equations by a scale analysis, removing those terms which are unimportant for the phenomenon in question. The scaling to be described here is incomplete, but is aimed at comparing the dominant processes at low and higher latitudes. A scale analysis for midlatitude synoptic systems is described in DM, Chapter 3.

2.1 The governing equations on a sphere

The basic equations for the motion of a dry atmosphere are

$$\rho \frac{D\mathbf{u}}{Dt} = -\nabla p + \rho \mathbf{g} - \rho \boldsymbol{\Omega} \wedge \mathbf{u} + \mathbf{F}, \quad (2.1)$$

$$\frac{D\rho}{Dt} = -\rho \nabla \cdot \mathbf{u}, \quad (2.2)$$

$$c_p \frac{D}{Dt} \ln \theta = \frac{Q}{T}, \quad (2.3)$$

$$p = \rho RT. \quad (2.4)$$

The first three represent the conservation of momentum, the conservation of mass and the conservation of energy (first law of thermodynamics), respectively; the last is the equation of state. The variables \mathbf{u} , p , ρ , T and θ and Q represent the (three-dimensional) fluid velocity, total pressure, density, temperature, potential temperature, and diabatic heating rate, respectively; \mathbf{F} represents viscous and or turbulent stresses, and \mathbf{g} is the effective gravity. The potential temperature is related

to the temperature and pressure by the formula $\theta = T(p^*/p)^\kappa$, where $p^* = 1000$ mb and $\kappa = 0.2865$.

The shape of the earth's surface is approximately an oblate spheroid with an equatorial radius of 6378 km and a polar radius of 6357 km. The surface is close to a *geopotential surface*, i.e. a surface which is perpendicular to the effective gravity (see DM, Chapter 3). As far as geometry is concerned the equations of motion can be expressed with sufficient accuracy in a spherical coordinate system (λ, ϕ, r) , the components of which represent longitude, latitude and radial distance from the centre of the earth (see Fig. 2.1). The coordinate system rotates with the earth at an angular rate $\Omega = |\boldsymbol{\Omega}| = 7.292 \times 10^{-5} \text{ rad s}^{-1}$. An important dynamical requirement in the approximation to a sphere is that the effective gravity appears only in the radial equation of motion, i.e. we regard spherical surfaces as exact geopotentials so that the effective gravity has no equatorial component. Further details are found in Gill (1982; 4.12).

Alternatively, the equations may be written in coordinates (λ, ϕ, z) , where λ is the longitude of a point, ϕ the latitude, and z is the height above the earth's surface (or more precisely the geopotential height). Note that $r = a + z$, where a is the earth's radius. Since the atmosphere is very shallow compared with its radius (99% of the mass of the atmosphere lies below 30 km, whereas $a = 6367$ km), we may approximate r by a and replace $\partial/\partial r$ by $\partial/\partial z$. In (λ, ϕ, z) coordinates, the frictionless forms of Eqs. (2.1) and (2.2) are (Holton, 1979, p 35)

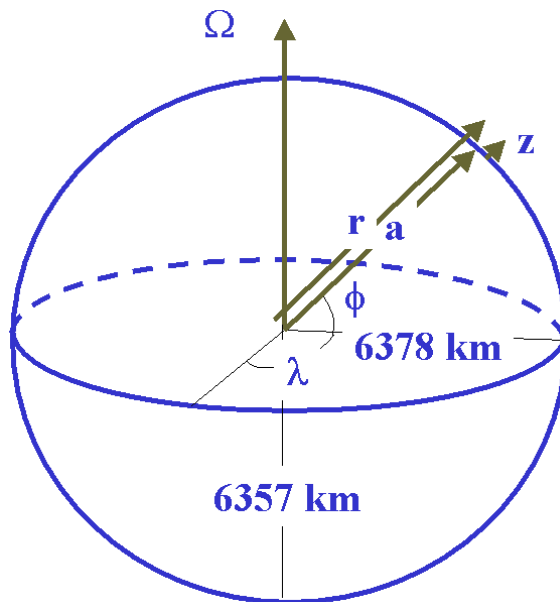


Figure 2.1: The (λ, ϕ, z) coordinate system

$$\frac{Du}{Dt} - \frac{uv \tan \phi}{a} + \frac{uw}{a} = -\frac{1}{\rho a \cos \phi} \frac{\partial p}{\partial \lambda} + 2\Omega v \sin \phi - 2\Omega \frac{w}{a} \cos \phi, \quad (2.5)$$

$$\frac{Dv}{Dt} + \frac{u^2 \tan \phi}{a} + \frac{vw}{a} = -\frac{1}{\rho a} \frac{\partial p}{\partial \phi} - 2\Omega u \sin \phi, \quad (2.6)$$

$$\frac{Dw}{Dt} - \frac{u^2 + v^2}{a} = -\frac{1}{\rho} \frac{\partial p}{\partial z} - g + 2\Omega \frac{u}{a} \cos \phi, \quad (2.7)$$

$$\frac{D\rho}{Dt} = -\frac{\rho}{a \cos \phi} \left[\frac{\partial u}{\partial \lambda} + \frac{\partial}{\partial \phi} (v \cos \phi) \right] - \rho \frac{\partial w}{\partial z} - 2\rho \frac{w}{a}, \quad (2.8)$$

where $\mathbf{u} = a \cos \phi \frac{d\lambda}{dt} \mathbf{i} + r \frac{d\phi}{dt} \mathbf{j} + \frac{dz}{dt} \mathbf{k} = u\mathbf{i} + v\mathbf{j} + w\mathbf{k}$. Here u, v and w represent the eastward, northward and vertical components of velocity, and $\frac{D}{Dt} \equiv \frac{\partial}{\partial t} + \mathbf{u} \cdot \nabla$, is the total-, or Lagrangian-, or material- derivative, following an air parcel. The terms with an asterisk beneath them will be referred to later.

2.2 The hydrostatic equation at low latitudes

In Chapter 1 we discussed the enormous diversity of motion scales which exists in low latitudes. We explore now the range of scales for which we may treat the motion as hydrostatic.

To carry out a scaling of (2.7) it is convenient to define a reference density and pressure, $\rho_0(z)$ and $p_0(z)$, characteristic of the tropical atmosphere and to define a perturbation pressure p' as the deviation of p from $p_0(z)$. Then $-g$ in Eq. (2.7) must be replaced by the buoyancy force per unit mass, $\sigma = -g(\rho - \rho_0(z))/\rho$, and p may be replaced by p' in Eqs. (2.5) and (2.6). Details may be found in DM, Ch. 3. Omitting primes, (2.7) may be written

$$\frac{Dw}{Dt} + \frac{1}{\rho} \frac{\partial p}{\partial z} - \sigma = \frac{u^2 + v^2}{a} + 2\Omega u \cos \phi. \quad (2.9)$$

To perform the necessary scale analysis we let $U, W, L, D, \delta p, \Sigma$ and τ represent typical horizontal and vertical velocity scales, horizontal and vertical length scales, a pressure deviation scale, a buoyancy scale and a time scale for the motion of a particular atmospheric system. The terms in (2.9) then have scales

$$\frac{W}{\tau} \frac{\delta p}{\rho D} \Sigma \frac{U^2}{a} \quad 2\Omega U \quad (2.10)$$

For a value of $\delta p \approx 1$ mb (10^2 Pa) over the troposphere depth (20 km), $\delta p/(\rho D) \approx 10^2 \div (1.0 \times 2.0 \times 10^4) = 0.5 \times 10^{-2} \text{ ms}^{-2}$. Also for $U \approx 10 \text{ ms}^{-1}$, $\Omega \approx 10^{-5} \text{ s}^{-1}$ and $a \approx 6 \times 10^6$ m, the last two terms are of the order of 10^{-4} and can be neglected.

The principal question is whether the vertical acceleration term can be neglected compared with the vertical pressure gradient per unit mass. To investigate this consider

$$\left| \frac{Dw}{Dt} / \left(\frac{1}{\rho} \frac{\partial p}{\partial z} \right) \right| \approx \frac{W}{\tau} / \left(\frac{1}{\rho} \frac{\delta p}{D} \right). \quad (2.11)$$

We obtain an estimate for δp from the horizontal equation of motion (2.1). This yields two possible scales, depending on whether the motion is quasi-geostrophic, i.e. $1/\tau \ll f$, or whether inertial effects predominate, $1/\tau \gg f$. In the latter case ($f\tau \ll 1$),

$$\delta p \approx P_1 = \rho LU/\tau;$$

while in the former case ($1 \ll f\tau$)

$$\delta p \approx P_2 = \rho LU f.$$

If $1/\tau = f$, then, of course, $\delta p \approx P_1 = P_2$. With the foregoing scales for P we can calculate the ratio in (2.11). Using P_1 we find that

$$\frac{W}{\tau} / \frac{1}{\rho} \frac{P_1}{D} = \frac{W}{U} \frac{D}{L}$$

Thus in the *high frequency limit* ($f\tau \ll 1$), hydrostatic balance will occur if $W \ll U$ and/or $D/L \ll 1$, provided that the other ratio is no more than $O(1)$. As we shall see later, this allows gravity waves to be treated hydrostatically, but the approximation is not valid for cumulus clouds.

In the *low frequency limit* ($1 \ll f\tau$) we use P_2 , and obtain

$$\frac{W}{\tau} / \frac{1}{\rho} \frac{P_2}{D} = \frac{W}{U} \frac{D}{L} \frac{\tau}{f}.$$

Now, even if $W \approx U$ and $D \approx L$, the hydrostatic approximation is justified provided $1 \ll f\tau$; which was the approximation that allowed us to obtain P anyhow. For synoptic-scale ($L \approx 10^6$), or planetary-scale ($L \approx a$) motions, for both of which $L \gg D$, the hydrostatic approximation is valid even if $1/\tau \approx f$, and therefore as f decreases towards the equator. Thus we are well justified in treating planetary motions as hydrostatic.

We must be careful, however. We note that (2.5) has a component of the Coriolis force that is a maximum at the equator, i.e. although $2\Omega v \sin\phi \rightarrow 0$ as $\phi \rightarrow 0$, $2\Omega w \cos\phi \rightarrow 2\Omega w$. But in invoking the hydrostatic approximation we neglect the term $2\Omega u \cos\phi$ in (2.7). Thus forming the total kinetic energy equation with our new hydrostatic set we will produce an inconsistency. It appears in the following manner. Multiplying (2.5) $\times u$, (2.6) $\times v$ and (2.7) $\times w$ and adding, we obtain

$$\frac{D}{Dt} \left[\frac{1}{2} (u^2 + v^2 + w^2) \right] = -\frac{1}{\rho} \left[\frac{u}{a \cos \phi} \frac{\partial p}{\partial \lambda} + \frac{v}{a} \frac{\partial p}{\partial \phi} + w \frac{\partial p}{\partial z} \right] - gw. \quad (2.12)$$

We notice that *all geometric terms and Coriolis terms* have vanished by cancellation between the equations. This is as it should be as these terms are products of the geometry or are a consequence of Newton's second law being expressed in an accelerating frame of reference. That is, the terms would not appear as forces in an inertial frame and may not change the kinetic energy of the system.

The problem is: if we make the assumption that the system is hydrostatic and note that for large scale flow, $|w| \ll |u|, |v|$, then the total kinetic energy may be written as

$$\frac{1}{2} \frac{D}{Dt} (u^2 + v^2) = -\frac{1}{\rho} \left[\frac{u}{a \cos \phi} \frac{\partial p}{\partial \lambda} + \frac{v}{a} \frac{\partial p}{\partial \phi} \right] - \left[2\Omega uw \cos \phi - \left(\frac{u^2 + v^2}{a} \right) w \right]. \quad (2.13)$$

The last term in square brackets represents a fictitious or spurious energy source that arises from the lack of consistency in scaling the system of equations. Since each equation is interrelated to the others, it is incorrect to scale one without consideration of the others. Therefore, if the hydrostatic equation is used, energetic consistency requires that certain curvature and Coriolis terms must be omitted also. These are the terms marked underneath by a star in Eqs. (2.5) - (2.8). Similar considerations to these are necessary when "sound - proofing" the equations (see e.g. ADM, Ch. 2).

The hydrostatic formulation of the momentum equations with friction terms included then becomes

$$\frac{Du}{Dt} = -\frac{1}{\rho a \cos \phi} \frac{\partial p}{\partial \lambda} + \left(2\Omega + \frac{u}{a \cos \phi} \right) v \sin \phi + F_\lambda, \quad (2.14)$$

$$\frac{Dv}{Dt} = -\frac{1}{\rho a} \frac{\partial p}{\partial \phi} - \left(2\Omega + \frac{u}{a \cos \phi} \right) u \sin \phi + F_\phi, \quad (2.15)$$

$$0 = -\frac{1}{\rho} \frac{\partial p}{\partial z} - g. \quad (2.16)$$

The need to neglect certain terms in the u and v equations to preserve energetic consistency has not been always appreciated. Many early numerical models, which were hydrostatic, could not conserve the total energy (i.e. kinetic and potential energy). The problem was traced to the inconsistency noted above.

2.3 Scaling at low latitudes

We consider now a more formal scaling of the hydrostatic equations in the vector form

$$\left(\frac{\partial}{\partial t} + \mathbf{V} \cdot \nabla_h \right) \mathbf{V} + w \frac{\partial}{\partial z} \mathbf{V} + f \mathbf{k} \wedge \mathbf{V} = -(1/\rho) \nabla_h p \quad (2.17)$$

$$0 = -\frac{1}{\rho} \frac{\partial p}{\partial z} - g \quad (2.18)$$

$$\left(\frac{\partial}{\partial t} + \mathbf{V} \cdot \nabla_h \right) \rho + \rho \nabla_h \cdot \mathbf{V} + \frac{\partial}{\partial z} (\rho w) = 0 \quad (2.19)$$

$$\left(\frac{\partial}{\partial t} + \mathbf{V} \cdot \nabla_h \right) \ln \theta + w \frac{\partial}{\partial z} \ln \theta = Q / (c_p T). \quad (2.20)$$

Here \mathbf{V} is the horizontal wind vector, w the vertical velocity component and ∇_h is the horizontal gradient operator. We recognize that perturbations of pressure and density from the basic state $p_0(z)$, $\rho_0(z)$ are relatively small, but seek to estimate their sizes for low- and middle-latitude scalings in terms of flow parameters.

We define a *pressure height scale* H_p such that $1/H_s = -(1/p_0)(dp_0/dz)$ and note that, using the hydrostatic equation for the basic reference state, $H_p = p_0/g\rho_0$. With quasi-geostrophic scaling appropriate to middle-latitudes, Eq. (2.17) gives $\delta p \approx \rho_0 fUL$, whereupon

$$\frac{\delta p}{p_0} \approx \frac{fUL}{gH_p} = \frac{F^2}{Ro} \Big|_{Ro \ll 1} \quad (2.21)$$

where $Ro = \frac{U}{fL}$ is the *Rossby number*,

and

$F = \frac{U}{(gH_p)^{1/2}}$ is a *Froude number*.

Note that (2.21) is satisfied even if $Ro \approx 1$, because $\delta p \approx \rho_0 fUL$ then provides the same scale as the inertial scale $\delta p \approx \rho_0 U^2$.

Hydrostatic balance expressed by (2.18) implies hydrostatic balance of the perturbation from the basic state, i.e. $\partial p'/\partial z = -g\rho'$, whereupon it follows that $\delta p/D \approx g\delta\rho$, and therefore

$$\frac{\delta\rho}{\rho_0} \approx \frac{\delta p}{gD\rho_0} \approx \frac{\delta p}{p_0} \left(\frac{H_s}{D} \right) \approx \frac{\delta p}{p_0} = \frac{F^2}{Ro} \Big|_{Ro \ll 1}, \quad (2.22)$$

assuming $D \approx H_p$.

Finally, since from the definition of θ , $(1 - \kappa) \ln p = \ln \rho + \ln \theta + \text{constant}$,

$$\frac{\delta\theta}{\theta_0} \approx -\kappa \frac{\delta p}{p_0} \approx \frac{F^2}{Ro} \Big|_{Ro \ll 1}. \quad (2.23)$$

Typically, $g \approx 10 \text{ ms}^{-2}$, $H_p \approx 10^4 \text{ m}$ whereupon, for $U \approx 10 \text{ ms}^{-1}$, $f \approx 10^{-4} \text{ s}^{-1}$ (a middle-latitude value), $Ro = 0.1$ and $F^2 = 10^{-3}$. It follows that in middle latitudes,

$$\frac{\delta\rho}{\rho_0} \approx \frac{\delta p}{p_0} \approx \frac{\delta\theta}{\theta_0} \approx 10^{-2}, \quad (2.24)$$

confirming that for geostrophic motions, fluctuations in p , ρ and θ may be treated as small.

At low latitudes, $f \approx 10^{-5} \text{ s}^{-1}$ so that for the same scales of motion as above, $Ro = 1$. In this case, advection terms in (2.17) are comparable with the horizontal pressure gradient. However, as we have seen, the foregoing scalings remain valid for $Ro \approx 1$ and therefore

$$\frac{\delta\rho}{\rho_0} \approx \frac{\delta p}{p_0} \approx \frac{\delta\theta}{\theta_0} \approx 10^{-3}. \quad (2.25)$$

Accordingly, we can expect fluctuations in p , ρ and θ to be an order of magnitude smaller in the tropics than in middle latitudes. The comparative smallness of the low-latitude perturbation may be associated with of the rapidity of the adjustment of the tropical motions to a pressure gradient imbalance; the adjustment being less constrained by rotational effects than at higher latitudes.

Consider now the adiabatic form of (2.20), i.e., put $Q = 0$. The scaling of this equation implies that

$$\frac{U}{L} \frac{\delta\theta}{\theta_0} \approx W \frac{1}{\theta_0} \frac{d\theta_0}{dz}.$$

Using (2.23) and defining

$$N^2 = \frac{g}{\theta_0} \frac{d\theta_0}{dz},$$

where N is the *buoyancy frequency* and,

$$Ri = \frac{N^2 H_p^2}{U^2},$$

is a *Richardson number*, we have

$$\frac{U}{L} \frac{F^2}{Ro} \approx W \frac{N^2}{g}, \quad \text{mathrm{or}} \quad W \approx \frac{UD}{L} \frac{1}{Ro Ri}, \quad (2.26)$$

an estimate that is valid for $Ro = 1$. It follows that, for the same scales of motion and *in the absence of convective processes of substantial magnitude*, we may expect the vertical velocity in the equatorial regions to be considerably smaller than in the middle latitudes. For example, for typical scales $U = 10 \text{ ms}^{-1}$, $D = 10 \text{ km}$, $L = 1000 \text{ km}$, $H_p = 10 \text{ km}$, $N = 10^{-2} \text{ s}^{-1}$, $Ri = 10^2$ and $W = 10^{-3}/Ro \text{ ms}^{-1}$. In the tropics, $Ro \approx 1$ so that (2.26) would imply vertical velocities on the order of 10^{-3} ms^{-1} , which is exceedingly tiny.

2.4 Diabatic effects, radiative cooling

We shall see that in the tropics it is important to consider diabatic processes. We consider first the diabatic contribution in regions away from active convection so that the *net* diabatic heating is associated primarily with *radiative cooling to space* alone. Figure 2.2 shows the annual heat balance of the earth's atmosphere. Of the 100 units of incoming short wave (SW) radiation, 31 units are reflected while the atmosphere radiates 69 units of long wave (LW) radiation to space. Accordingly, at the outer limits of the atmosphere, there exists radiative equilibrium. Altogether 46 units of SW radiation are *absorbed* at the surface. The surface emits 115 units of radiation in the long wave part of the spectrum, but 100 units of this are returned from the atmosphere. It is clear that, on average, there is a *net radiative cooling* of the atmosphere, amounting to 31 units, or 31% of the *available incident radiation*. On average, this cooling is balanced by a transfer of sensible heat (7 units) and latent heat (24 units) to the atmosphere from earth's surface. The incoming solar radiation of 1360 Wm^{-2} (the solar constant) intercepted by the earth ($\pi a^2 \times 1360$) W is distributed, when averaged over a day or longer, over an area $4\pi a^2$ (see Fig. 2.3).

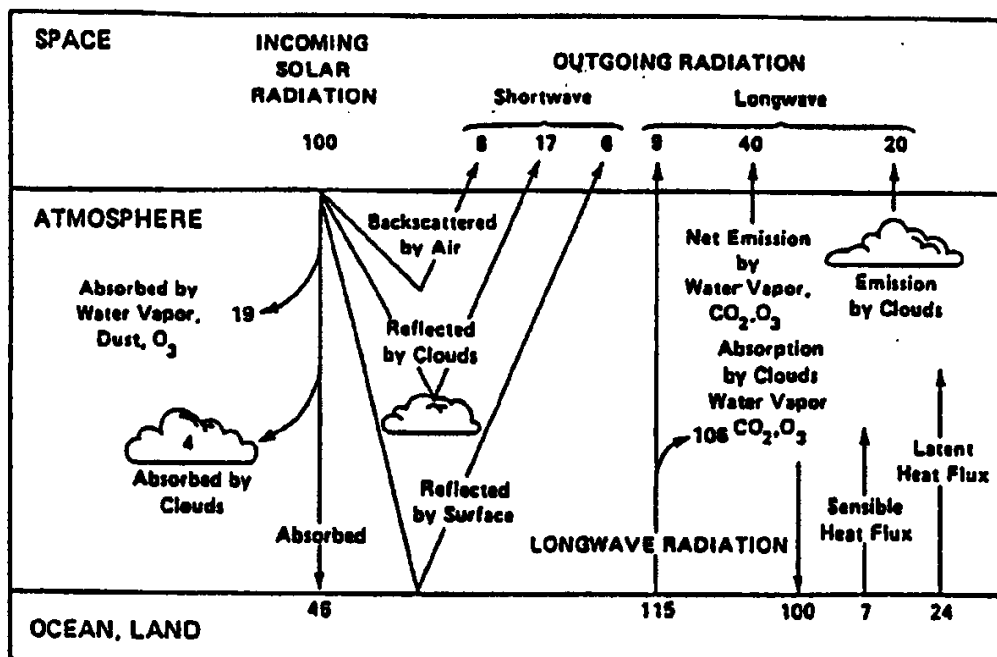


Figure 2.2: Schematic representation of the atmospheric heat balance. The units are percent of incoming solar radiation. The solar fluxes are shown on the left-hand side, and the longwave (thermal IR) fluxes are on the right-hand side (from Lindzen, 1990).

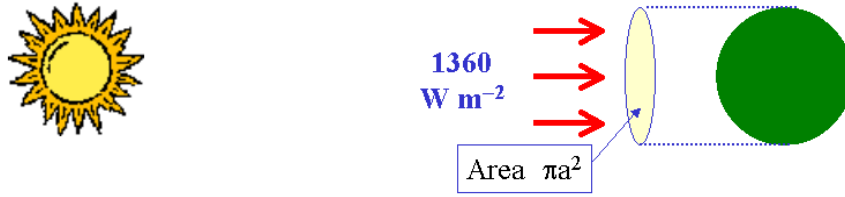


Figure 2.3: Distribution of solar radiation over the earth's surface.

As discussed above, the atmosphere loses heat by radiation over 1 day or longer at the rate $\Delta Q = 0.31 \times 0.25 \times 1360 \text{ W/m}^2$. In unit time, this corresponds to a temperature change ΔT given by $\Delta Q = c_p M \Delta T$, where M is the mass of a column of atmosphere 1 m^2 in cross-section. Since $M = (\text{mean surface pressure})/g$, we find that

$$\Delta T = -\frac{0.31 \times 0.25 \times 1360 \times 24 \times 3600}{1005 \times 1.013 \times 10^4} \approx -0.9 \text{ K/day}.$$

Actually, the rate of cooling varies with latitude. From the surface to 150 mb (i.e. for $\approx 85\%$ of the atmosphere's mass), $\Delta T \approx -1.2 \text{ K/day}$ from $0 - 30^\circ$ lat., -0.88 K/day from $30 - 60^\circ$ lat., and -0.57 K/day from $60 - 90^\circ$ lat. The stratosphere and mesosphere warm a little on average, but even together they have relatively little mass.

The estimate (2.25) suggests that for synoptic scale systems in the tropics, we can expect potential temperature changes associated with *adiabatic* changes of no more than a fraction of a degree. The estimate (2.26) shows that associated vertical motions are on the order $DU/(LRi)$ which is typically $10^4 \times 10 \div (10^6 \times (10^{-4} \times 10^8 \div 10^2)) \approx 10^{-3} \text{ ms}^{-1}$.

In contrast, radiative cooling at the rate $Q/c_p = -1.2 \text{ K/day}$ would lead to a subsidence rate which we estimated from (2.20) as

$$WN^2/g \approx (Q/c_p)/T,$$

whereupon

$$W \approx -\frac{g}{N^2} \times \frac{1.2}{300} \times \frac{1}{24 \times 3600} = -0.5 \text{ cm/sec}.$$

It follows that we may expect *slow* subsidence over much of the tropics and that the vertical velocities associated with radiative cooling are somewhat larger than those arising from synoptic-scale adiabatic motions.

We consider now the implications of the foregoing scaling on the vertical structure of the atmosphere. The vertical component of the vorticity equation corresponding with (2.17) and (2.18) is

$$\begin{aligned}
 \left(\frac{\partial}{\partial t} + \mathbf{V} \cdot \nabla \right) \zeta + \left[\zeta \nabla \cdot \mathbf{V} + w \frac{\partial \zeta}{\partial z} \zeta + \mathbf{k} \cdot \nabla w \wedge \frac{\partial \mathbf{V}}{\partial z} \right] + \mathbf{V} \cdot \nabla f + f \nabla \cdot \mathbf{V} \\
 = \mathbf{k} \wedge \left[(1/\rho) \nabla \rho \wedge (1/\rho) \nabla p \right]
 \end{aligned} \tag{2.27}$$

We compare the scales of each term in this equation with the scale for term A for $Ro \ll 1$ and $Ro \approx 1$ (see Table 2.1).

Table 2.1: Ratio of terms in Eq. (2.27).

Term	A	B	C	D	E
Generally	1	$\frac{L}{U} \frac{W}{D}$	$\left(\frac{2\Omega}{U} \frac{L^2}{a} \cos \phi \right)$	$\frac{L}{U} \frac{W}{D} \frac{1}{Ro}$	$\frac{F^2}{Ro^2}$
Midlatitudes $Ro \ll 1$	1	$\frac{1}{RiRo}$	(")	$\frac{1}{RiRo^2}$	$\frac{F^2}{Ro^2}$
Low latitudes $Ro \approx 1$	1	$\frac{1}{Ri}$	(")	$\frac{1}{Ri}$	F^2

Using typical values chosen earlier ($Ri = 10^2$, $F^2 = 10^{-3}$) term C is $O(1)$, while terms B, D and E are of order 10^{-1} , 1 and 10^{-1} in the middle latitudes and of order 10^{-2} , 10^{-2} and 10^{-3} in the tropics, respectively. Thus, for $R \ll 1$, we have a general balance

$$\left(\frac{\partial}{\partial t} + \mathbf{V} \cdot \nabla \right) (\zeta + f) + (f + \zeta) \nabla \cdot \mathbf{V} = 0, \tag{2.28}$$

whereas for $Ro \geq 1$, the term D is reduced by more than two orders of magnitude and then

$$\left(\frac{\partial}{\partial t} + \mathbf{V} \cdot \nabla \right) (\zeta + f) = 0. \tag{2.29}$$

This is an important result. It tells us that outside regions where condensation processes are important, not only is the vertical velocity exceedingly small, the flow is almost barotropic. The implications are considerable. Such motions *cannot* generate kinetic energy from potential energy; they must obtain their energy either from barotropic processes such as lateral coupling or from barotropic instability.

We consider now the role of diabatic source terms. Again we *assume that* it is sufficient to approximate (2.20) by

$$w (N^2/g) = Q / (c_p T), \tag{2.30}$$

but this time we assume that Q arises from precipitation in a disturbed region.

Budget studies have shown that three quarters of the radiative cooling of the tropical troposphere is balanced by latent heat release. From figures given earlier, this means for 0-30° latitude, the warming rate is about 0.9 K/day. Gray (1973) estimated that tropical weather systems cover about 20% of the tropical belt. This would imply a warming rate Q/c_p **approx** $5 \times 0.9 = 4.5$ K/day in weather systems.

First let us calculate the rainfall that this implies. A rainfall rate of 1 cm/day (i.e. 10^{-2} m/day) implies 10^{-2} m³ /day per unit area (i.e. m⁻²) of vertical column. This would imply a latent heat release $\Delta Q \approx L \nabla m$ per unit area per day, where $L = 2.5 \times 10^6$ J/kg is the latent heat of condensation and Δm is the mass of condensed water. Since the density of water is 10^3 kg/m³, we have $\Delta Q \approx 2.5 \times 10^6$ J/kg $\times 10^{-2}$ m³ $\times 10^3$ kg/m³ per unit area = 2.5×10^7 J/unit area/day. This is equivalent to a mean temperature rise δT in a column extending from the surface to 150 mb given by $c_p m_a \Delta T \approx 2.5 \times 10^7$ J/unit area/day where $m_a = (1000 - 150)$ mb/g is the mass of air unit area in the column. With $c_p = 1005$ J/K/kg we obtain $\Delta T \approx 2.9^\circ\text{K/day}$. Therefore, a heating rate of 0.9°K/day requires a rainfall of about 1/3 cm/day averaged over the tropics, or 1.5 cm/day averaged over weather systems. Returning to (2.30) and, using the same parameters as before we find that a heating rate of 4.5 K/day leads to a vertical velocity of about 1.5 cm/sec, although the effective N^2 is smaller in regions of convection which would make the estimate for w a conservative one.

We can use these simple concepts to obtain an estimate for the horizontal area occupied by precipitating disturbances (see Fig. 2.3). Simply from mass conservation, the ratio of the area of ascent to descent must be inversely proportional to the ratio of the corresponding vertical velocities. Using the figures given above, this ratio is 1/3, but allowing for a smaller N in convective regions will decrease this somewhat, closer to Gray's estimate of 1/5.

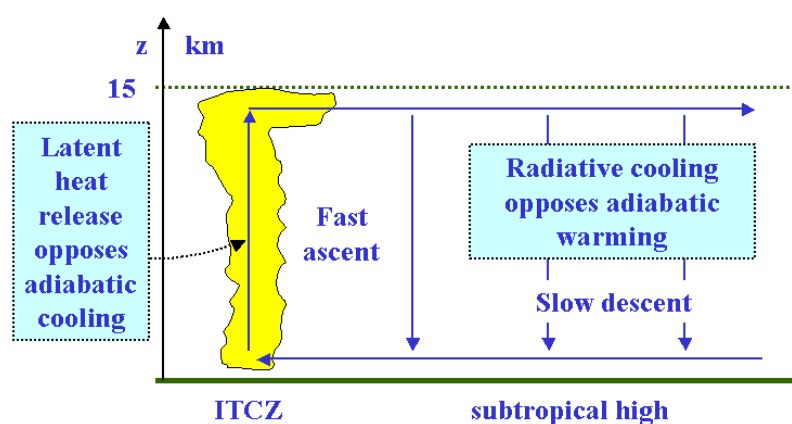


Figure 2.4: Schematic diagram showing relatively strong updraughts occupying a much smaller horizontal area than the much weaker compensating downdraughts.

2.5 Some further notes on the scaling at low latitudes

1. In mid-latitudes $Ro \ll 1$ and it is a convenient small parameter for asymptotic expansion. However, generally at low latitudes as $f \rightarrow 0$, $Ro \approx 1$ and we must seek other parameters. One such parameter, $(RiRo)^{-1}$ is *always* small, even if $L \approx 10^7$ m.
2. The vorticity equation contains useful information. It tells us that synoptic-scale phenomena ($L \approx 10^6$ m) are nearly uncoupled in the vertical except in circumstances that limit (2.29). These are:
 - a. Q/c_p large. Then w is scaled from the thermodynamic equation such that $wN^2/g \approx Q/(c_pT)$.
 - b. For planetary-scale motions ($L \approx 10^7$) of the type discussed in Chapter 1, we have again $Ro \ll 1$. Then, if $D \approx H_p$ as before, the quasi-geostrophic scaling (e.g., 2.24) applies once more. Moreover, the appropriate vorticity equation is (2.28) instead of (2.29). In this case, coupling in the vertical is re-established.
 - c. If the motions involve vertically-propagating gravity waves with $D \ll H_p$, but still with $L \approx 10^7$ m and if $U \rightarrow 0$, then again $Ro \ll 1$ and vertical coupling occurs.

As a consequence of (2.29), the atmosphere is governed by barotropic processes. That is, the usual baroclinic way of producing kinetic energy from potential energy, i.e., the lifting of warm air and the lowering of cold air, does not occur. It follows then that energy transfers are strictly limited. How then can the kinetic energy be generated in the tropics? Obviously the answer lies in convective processes. But if this is so, why are the thermal fields so flat? This will be addressed later. However it is interesting at this point to gain some insight into this feature of the tropical atmosphere.

If $wN^2/g \approx Q/(c_pT)$, then $\langle w'T' \rangle \approx g \langle Q'T' \rangle / (N^2c_pT)$. Now $\langle w'T' \rangle$ measures the rate of production of kinetic energy and $g \langle Q'T' \rangle$ is proportional to the rate of production of potential energy (i.e. heating where it is hot and cooling where it is cold). Thus the statement $\langle w'T' \rangle \approx g \langle Q'T' \rangle / (N^2c_pT)$ implies that, in the tropics, potential energy is converted to kinetic energy as soon as it is generated. In other words there is no storage of potential energy. We know from scaling principles that $wN^2/g \approx Q/(c_pT)$, as $\partial\theta/\partial t$ and $\mathbf{V} \cdot \nabla\theta$ are relatively small in the tropics (see section 2.3). Since large precipitation implies large Q , it follows that w must be comparatively large as well.

If ∇T were large, a third term would enter such that $\langle w'T' \rangle + (g/N^2) \langle T'\mathbf{V}' \cdot \nabla T \rangle \approx \langle Q'T' \rangle / (c_pT)$ and this is tantamount to having storage even if \mathbf{V} is the same in both cases.

2.6 The weak temperature gradient approximation

One can derive a balanced theory for motions in the deep tropics by assuming that $\partial\theta/\partial t$ and $\mathbf{V} \cdot \nabla\theta$ are much less than $w(\partial\theta/\partial z)$, whereupon

$$w \frac{\partial\theta}{\partial z} = \frac{D\theta}{Dt} = S_\theta, \quad (2.31)$$

where $S_\theta = Q/(c_p\pi)$, $\pi = (p/p_o)^\kappa$ is the Exner function, and $p_o = 1000$ mb. The vorticity equation (2.28) may be written

$$\left(\frac{\partial}{\partial t} + \mathbf{V} \cdot \nabla \right) (\zeta + f) = (\zeta + f) D \quad (2.32)$$

where D is the horizontal divergence $\nabla \cdot \mathbf{V}$, and the continuity equation gives

$$D = \nabla \cdot \mathbf{V} = -\frac{1}{\rho} \frac{\partial(\rho w)}{\partial z}. \quad (2.33)$$

Using (2.31) the vorticity equation becomes

$$\left(\frac{\partial}{\partial t} + \mathbf{V} \cdot \nabla \right) (\zeta + f) = \frac{(\zeta + f)}{\rho} \frac{\partial}{\partial z} \left(\frac{\rho S_\theta}{\partial\theta/\partial z} \right). \quad (2.34)$$

If there were no diabatic heating ($S_\theta = 0$), the right-hand-side of (2.33) would be zero and absolute vorticity values would be simply advected around at fixed elevation by the horizontal wind. The role of heating is to produce vertical divergence, which, in turn, decreases the absolute vorticity if the divergence is positive and increases it if the divergence is negative (i.e. if there is horizontal convergence). If the divergence and the horizontal wind fields are known, it is therefore possible to predict the evolution of the absolute vorticity field.

The final difficulty is predicting the horizontal wind field. The horizontal wind components can be written as sums of parts derived from a streamfunction ψ and parts derived from a velocity potential χ :

$$v_x = -\frac{\partial\psi}{\partial y} + \frac{\partial\chi}{\partial x} \quad v_y = \frac{\partial\psi}{\partial x} + \frac{\partial\chi}{\partial y}. \quad (2.35)$$

However, ψ and χ may be written in terms of ζ_a and D :

$$\nabla^2\psi = \zeta_a - f \quad (2.36)$$

$$\nabla^2\chi = D \quad (2.37)$$

where ∇^2 is the horizontal Laplacian operator. Equations (2.36) and (2.37) are readily solved for ψ and χ using standard numerical methods, after which the horizontal velocity may be determined from (2.35). Given the horizontal velocity and the divergence, we have the tools needed to completely solve the vorticity equation. In

practice, (2.34), stepped forward in time and the diagnostic equations (2.36) and (2.37) are solved after each time step to enable the velocity field to be updated using (2.35). All that is required to close the system is a method of specifying the heating term S_θ .

The principal determinant of the sign of the horizontal divergence in (2.33) is the sign of $\partial S_\theta / \partial z$. If heating increases with height, divergence is negative, and the magnitude of the absolute vorticity increases with time, whereas S_θ decreasing with height results in positive divergence and decreasing absolute vorticity. Deep convection generally results in increasing vorticity or spinup in the lower troposphere and spindown in the upper troposphere, whereas other regions typically dominated by radiative cooling and shallow convection tend to experience the reverse.

In spite of the fact that tropical storms don't formally obey the weak temperature gradient approximation, the above picture holds qualitatively for them as well. However, gravity wave dynamics are not encompassed by this picture, so the wind perturbations associated with these waves are not captured. Furthermore, consideration of frictional effects is important to the quantitative prediction of tropical flows, especially in the long term. In spite of these deficiencies, the above picture of tropical dynamics should be useful for understanding the short-term evolution of most tropical weather systems. In a later chapter we approach the problem of determining the pattern of heating associated with moist convection. More details on the weak temperature gradient approximation can be found in papers by Sobel and Bretherton (2000), Sobel *et al.* (2001) and Raymond and Sobel (2001).

Chapter 3

MORE ON DIABATIC PROCESSES

In general the total diabatic heating rate may be written as the sum of three components,

$$Q_{total} = Q_{rad} + Q_{cond} + Q_{sen} \quad \text{☺}$$

the contributions on the right-hand-side being from radiative, condensational and sensible heating, respectively. Figure 3.1 shows schematically the typical vertical distribution of these contributions.

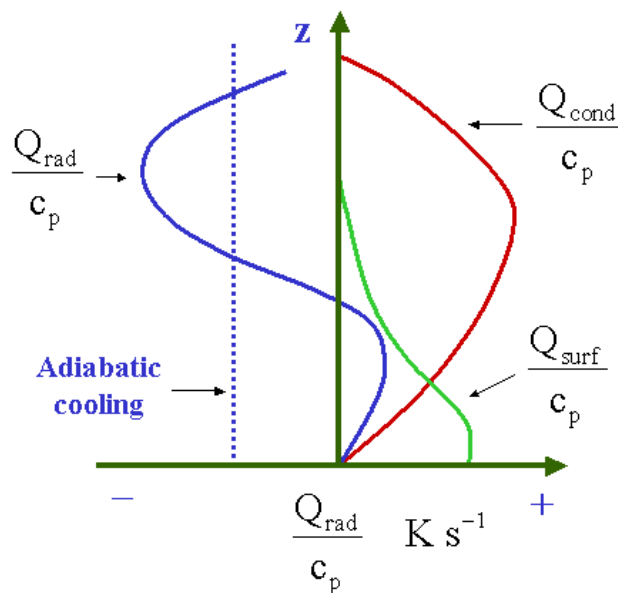


Figure 3.1: Vertical distribution of radiative, condensational and sensible heating.

While diabatic processes drive atmospheric motion, it is important to emphasize that the contributions Q_{rad} , Q_{cond} , Q_{sen} are not *pure* external functions, but are

strongly coupled to the flow configuration they produce. This interdependence reflects a redistribution of the only pure external heating function, the solar energy, which impinges on the atmosphere from space (S_0). In order to understand the full relevance of diabatic process and how the drive atmospheric motions, it is necessary to understand the manner in which S_0 is redistributed.

If we assume that the atmosphere is in radiative equilibrium with outer space and note that the earth is a sphere, it is clear that considerably more energy will reach the surface near the equator than near the poles. Consequently, heat energy must be transferred poleward if there is to be an approximate steady state. The question arises, how is the energy S_0 redistributed in the vertical? We consider first the effects of radiation alone.

Figure 3.2 shows a highly simplified radiation model in which we have neglected the absorption of short wave radiation, since it is at the earth's surface that the major effect of S_0 occurs. Pure radiative balance at the surface would require that

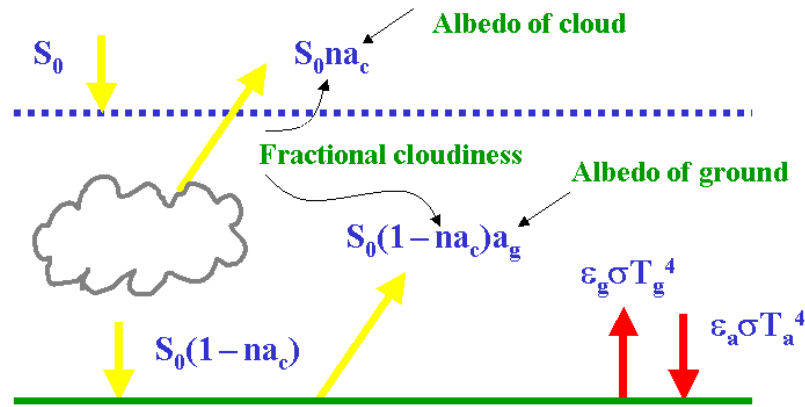


Figure 3.2: A highly simplified radiation model.

$$S_0(1 - na_c)(1 - a_g) = \varepsilon_g \sigma T_g^4 - \varepsilon_a \sigma T_a^4, \quad (3.1)$$

where n denotes the fractional area of cloud, T_s and T_a are the temperatures of the surface and the atmosphere ¹, respectively, a_c and a_a are the albedos of cloud and the ground surface, ε_c and ε_s , are the corresponding emissivities, and σ is the Stefan-Boltzmann constant. This equation says that the net short wave flux into the atmosphere is balanced by the net outward long wave flux. Now $\varepsilon_a \sigma T_a^4$ represents the re-radiation of the atmosphere back to the surface. As $\varepsilon_a \approx 0.7$, we cannot neglect this term. In fact such long wave absorption has a major impact on the distributions shown in Fig. 3.1. However, the solar radiation (the left hand side of Eq. (3.1) may be disposed of in other ways besides being merely radiated upwards (i.e. $\varepsilon_g \sigma T_g^4$) as long wave radiation. Adjacent to the surface there will be diffusion of heat to

¹For simplicity it is assumed here that the atmosphere is isothermal.

or from the atmosphere and possibly convective mixing upwards to the atmosphere. Over moist ground or over the ocean, evaporation may occur and there will be an evaporative flux of heat away from the surface (Fig. 3.3). In this case the total energy balance at the surface is

$$S_0(1 - na)(1 - a_g) = \epsilon_g \sigma T_g^4 - \epsilon_a \sigma T_a^4 + F_s + F_L, \quad (3.2)$$

where F_s , and F_L are the sensible and latent heat fluxes, respectively. The former quantity, F_s , depends on the magnitude and sign of temperature difference $\Delta T = T_g - T_a$. The behaviour is roughly as sketched in Fig. 3.4. If $\Delta T > 0$, $F_s > 0$ and there is convective heat transfer to the air, If $\Delta T < 0$, $F_s < 0$, but the heat transfer is then diffusive and relatively small (i.e. $|F_{s\text{ conv.}}| \gg |F_{s\text{ diff.}}|$).

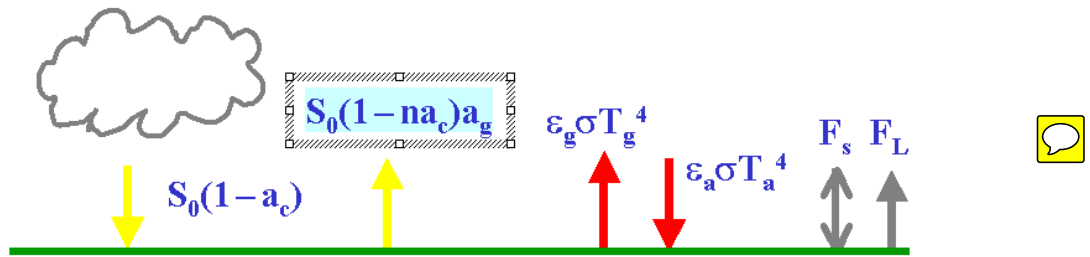


Figure 3.3: Energy balance at the earth's surface.

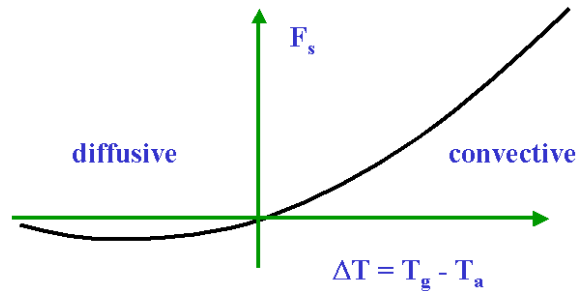
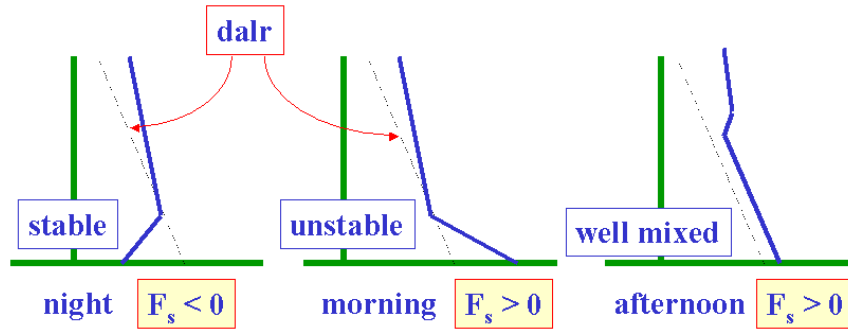


Figure 3.4: $F_s = F_s(\Delta T)$.

Generally, $F_L \geq F_s$. Thus F_s , and F_L are usually net fluxes of heat away from the surface. Note that they effectively change radiative diabatic heating into other types of heat transfer, which then contribute to redistributing the heat. Both F_s , and F_L have important effects on the total columnar heating rates, Q_g and Q_L , and both are functions of atmospheric motion and structure. The dependence of F_s on ΔT and on the temperature structure is depicted in Fig. 3.5. Note that the greater ΔT , the greater is the degree of convective instability within the boundary layer, a feature seen also in Fig. 3.5.

The functions F_s and F_L can be parameterized as

Figure 3.5: Atmospheric conditions influencing F_s .

$$F_s = \rho C_D |V| (T_g - T_a), \quad (3.3)$$

$$F_L = \rho C_g |V| (q_s - q_a), \quad (3.4)$$

where \mathbf{V} is the wind speed near the surface, T_a , and q_a are the temperature and specific humidity of the air near the surface, T_g , and q_g , are the sea surface temperature and saturated specific humidity at the sea surface temperature, respectively, and C_D , C_E are empirical coefficients that depend on the surface characteristics (and over the sea on wind speed). The coefficient C_D is called the *drag coefficient* and C_E is called the *heat transfer coefficient*. Generally, the fluxes F_s and F_L depend on

- the degree of surface roughness,
- the wind speed,
- and in the case of moisture there is a dependency on the degree of saturation in the vertical.

The *sensible heating*, Q_{sen} , tends to be confined to the lowest 1-2 km, except over dry continental surfaces where it may be as high as 4 km. Further it represents an immediate acquisition of heat by the column.

The *latent heating*, Q_{cond} , is not immediate, but requires saturation in order to accomplish the heat release. This is a process that is highly dependent on the dynamics. There are three main ways of producing condensation: two are associated with advection, the other (non-dynamic) by radiative cooling (Fig. 3.6).

Most of the latent heat release in the tropical atmosphere is associated with moist convection, vertical advective process. We will restrict our attention to this form of Q_L . The actual region of moist ascent is rather small and rather vigorous. Most of the tropics is involved in the flux of latent heat (F_L), but only a small part is involved in its release. The situation is depicted in the moisture cycle, shown schematically in Fig. 3.7.

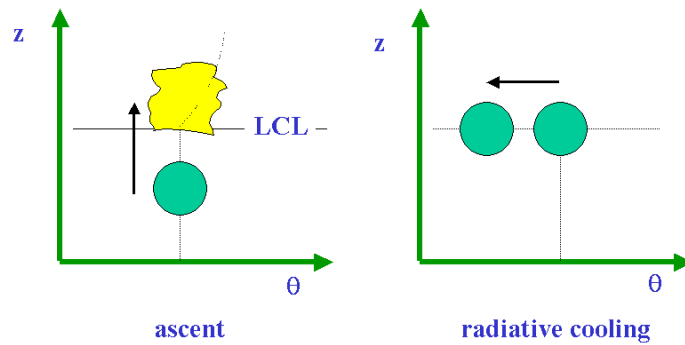


Figure 3.6: Schematic illustration of process leading to condensation.

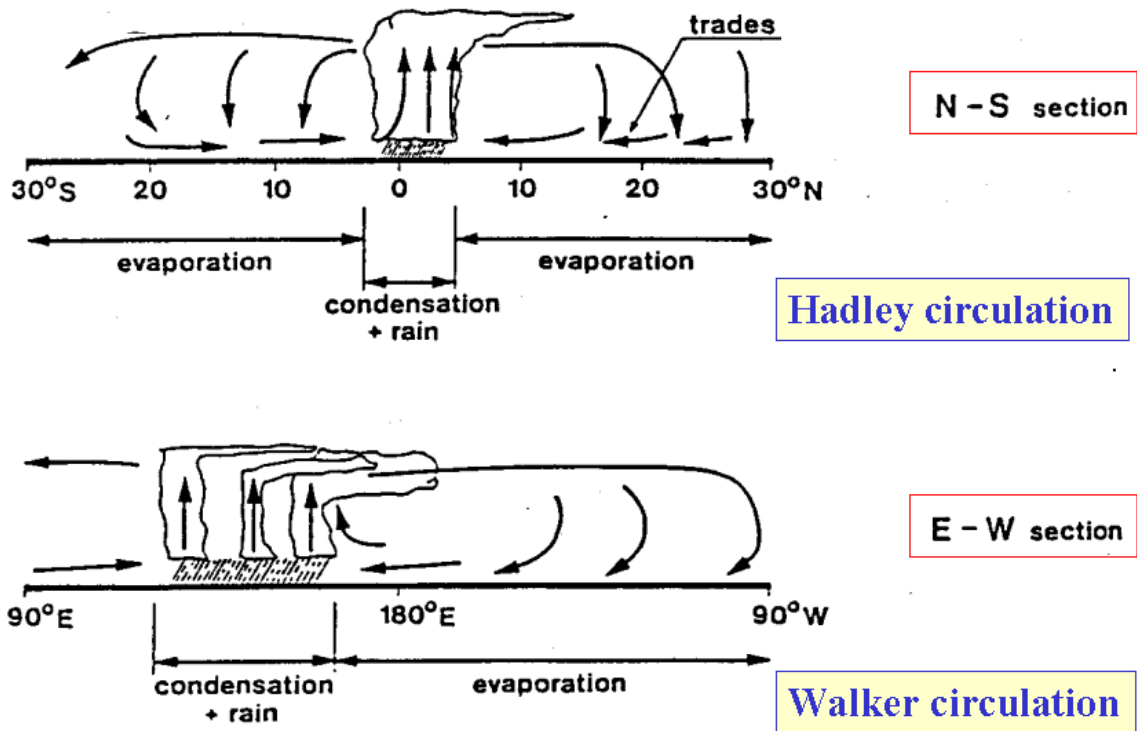


Figure 3.7: The moisture cycle in the tropics.

In summary, there are two major forms of Q . These are Q_{rad} , principally the longwave component thereof, and Q_L , which is an indirect manifestation of S_0 via F_L . Figures 3.8 and 3.9 indicate something of their disposition in the east-west and north-south cross-sections. Of particular importance in Fig. 3.8 is that the *longitudinal gradient* of net flux is of the same magnitude as the *latitudinal gradient*. Most of the variation in the latitudinal profile may be accounted for in the latitudinal gradient of the solar input. However, as the solar input is constant along 25°N ,

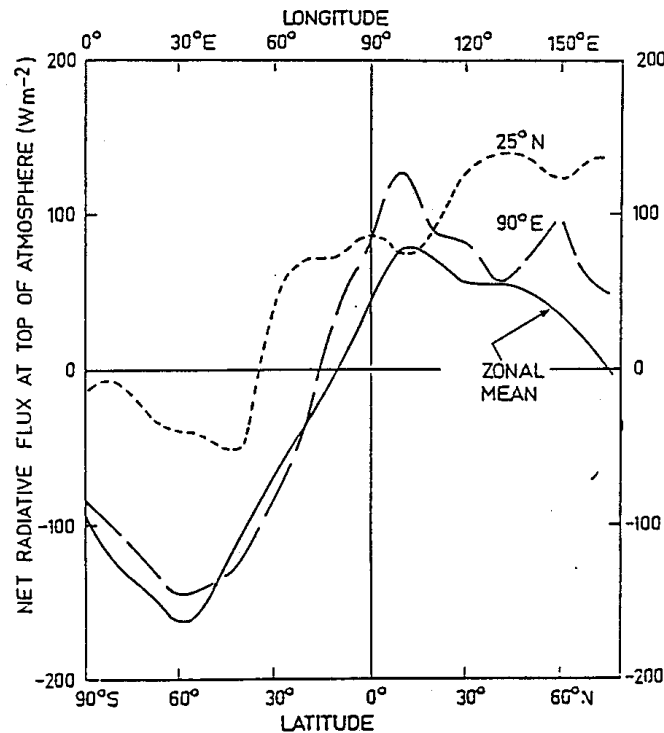


Figure 3.8: The distribution of the net radiative flux at the top of the atmosphere inferred from NIMBUS 3. Plots of the zonally averaged net flux (solid line), the flux along 90° E (largest dashed line) and along 20° N (dashed curve) for July 1969 are shown. (From Webster & Stephens, 1979).

the longitudinal variation in net flux must be due to other effects such as ground albedo and cloud cover; the latter being closely associated with the dynamical system. Note that the desert regions (10° E to 50° E) appear as net radiative sinks with the outgoing longwave radiation (OLR) greater than the net incoming solar flux. On the other hand, the convective monsoon regions (80° E to 18° E) act as net radiative heat sources. In the case shown the radiative heating distribution is probably indicative of the total heating field. The condensational heating will be a maximum in the monsoon regions as Q_{cond} will be strongly tied to the precipitation patterns. **In the desert regions** the sensible heating will act in a sense opposite to that of radiative cooling, but this component will be smaller and restricted to at most the lowest few kilometres of the atmosphere. Thus atmospheric columns above the deserts should be continually cooling and the columns in the monsoon regions continually heating. A dynamic response is necessary to rectify the imbalance. Recall that from the scaling of Chapter 2, [see Eq. (2.29)], $N^2 w \approx Q/(c_p T)$, which states that the diabatic heating ($Q_{rad} + Q_{cond}$) is nearly exactly balanced by w . As a consequence, dynamical processes are involved and, consistent with mass continuity, a circulation develops.

Note, however, that Q_{cond} will depend on w so that feedback loops are extremely important. To determine the form of the dynamic response, Webster and Stephens (1979) used data from Newell *et al.* (1972) to calculate the heat convergence into the longitudinal section between the arid regions of Saudi Arabia (I), the Arabian Sea (II) and the Bay of Bengal (III). The resultant fluxes, together with the estimates of the vertical profiles of the components of the total heating are shown in Fig. 3.9.

The dynamic response to the heating imbalance is such as to converge heat into the upper troposphere of the desert regions and out of the convective regions. The net radiative cooling is compensated by adiabatic warming over the deserts and an adiabatic cooling over the Bay of Bengal. In other words, the dynamic response to the longitudinal imbalance of total heating is the generation of a rather vigorous thermally-forced circulation.

More details about the role and representation of moist processes and, in particular, moist convection are given in a later chapter.

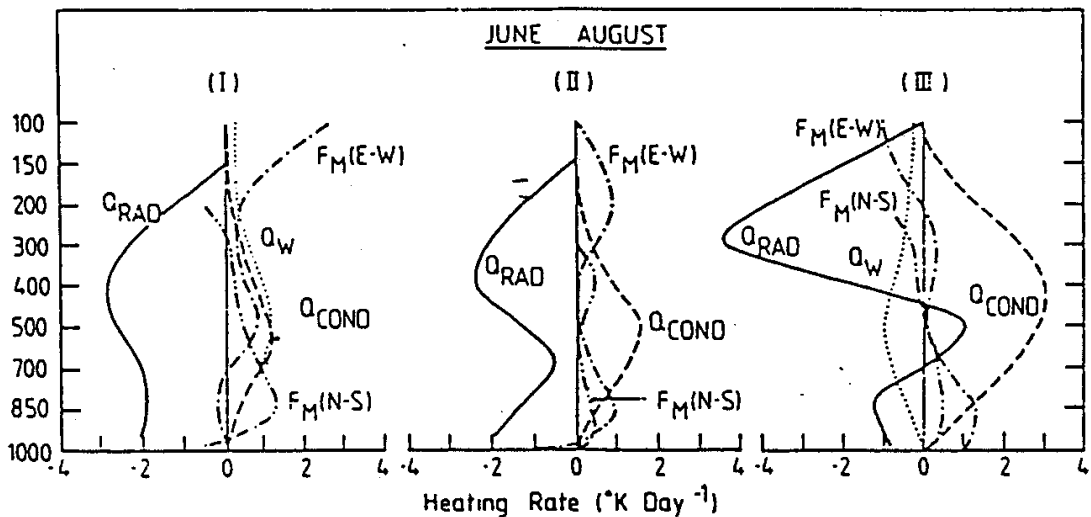


Figure 3.9: The vertical distribution of the heating components in the atmospheric column above Saudi Arabia (I), the Arabian Sea (U) and the Bay of Bengal (III). The quantities Q_{rad} , Q_{cond} , $F_M(E-W)$ and $F_M(N-S)$ refer to heating due to radiation, condensation and heat flux convergence due to mean zonal ($E-W$) and meridional ($N-S$) motions.

Chapter 4

THE HADLEY CIRCULATION

The early work on the mean meridional circulation of the tropics was motivated by observations of the trade winds. Halley (1686) and Hadley (1735) concluded that the trade winds are part of a large-scale circulation which results from the latitudinal distribution of solar heating. This circulation, now known as the Hadley circulation, consists of upward motion at lower latitudes, poleward motion aloft, sinking motion at higher latitudes and low-level equatorial flow. Despite the absence of upper-air observations Hadley deduced that the upper-level flow has a westerly component due to the effect of the earth's rotation.

The mean zonally-averaged circulation of the atmosphere is illustrated in Fig. 4.1. The annual mean (Fig. 4.1c) shows two thermally-direct circulations, the Hadley Cells, with ascent at the equator and descent at 30°N and 30°S . The Hadley cells are broadly symmetric about the equator in the annual mean, although with a slight displacement into the northern hemisphere. In each hemisphere there is a subtropical westerly upper-level jet located just polewards of the descending branch of the Hadley cell. In the northern hemisphere winter (DJF) (Fig. 4.1a) the northern Hadley cell is much stronger and broader than the southern cell. The location of the ascending branch has moved south of the equator into the summer hemisphere. The westerly jet in the northern hemisphere is stronger and further south than in the annual mean. In the southern hemisphere winter (Fig. 4.1b) the southern Hadley cell dominates the tropical circulation, the northern Hadley cell is weak and very narrow. The maximum ascent is north of the equator in the summer hemisphere and the southern hemisphere westerly jet shows a double jet structure with a maximum at the location of the descending branch of the Hadley cell and a second maximum further south.

In the tropical troposphere the departure from zonal symmetry is much smaller than that in midlatitudes. This is illustrated in Fig. 4.2 which shows the departures from zonal symmetry of the time-averaged geopotential height. The cross-section at 45°N shows substantial eddy activity¹ throughout the troposphere. In contrast, at 25°N the eddy activity has much smaller amplitude in the troposphere. Thus we can use an axisymmetric model to develop a simple model of the Hadley circulation.

¹Substantial in the sense that fluctuations about the mean are comparatively large.

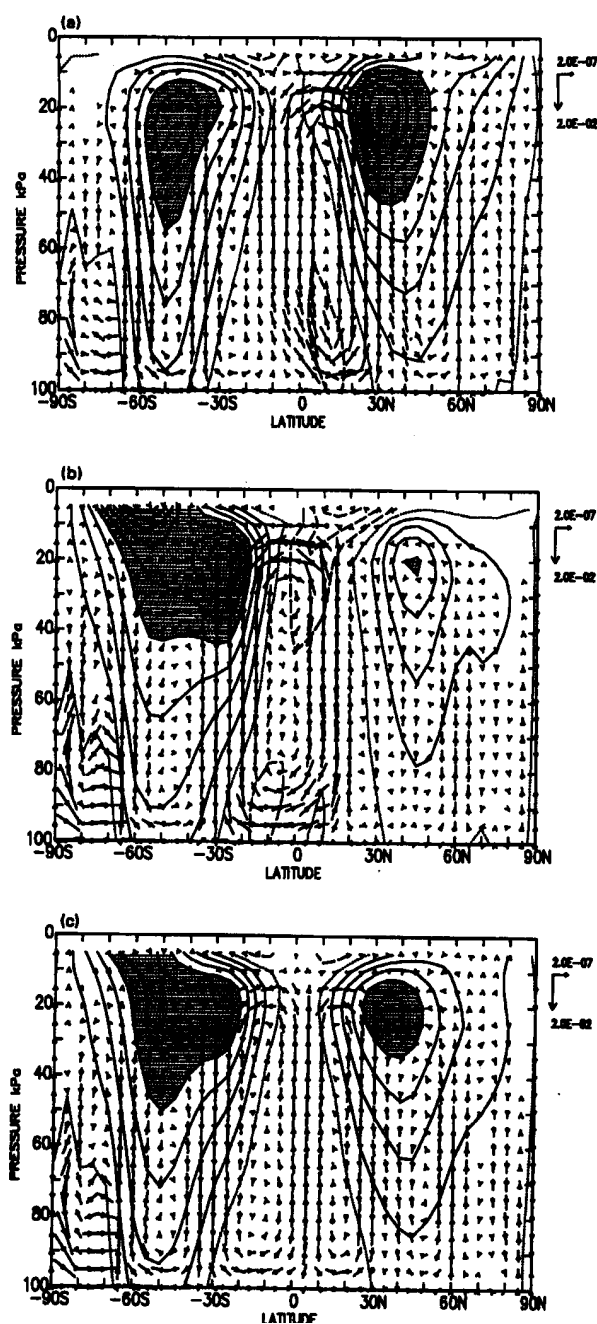


Figure 4.1: The zonal mean zonal wind and vectors of the meridional wind for (a) December-January-February, (b) June-July-August, and (c) the annual mean, based on six years of ECMWF data. Contour interval 5 m s^{-1} , with values in excess of 20 m s^{-1} shaded. The horizontal sample arrow indicates a meridional wind of 3 m s^{-1} , and the vertical sample arrow a vertical velocity of 0.03 Pa s^{-1} . (From James, 1994)

Such a model was developed by Held and Hou (1980). The description of this model given here closely follows that of James (1994).

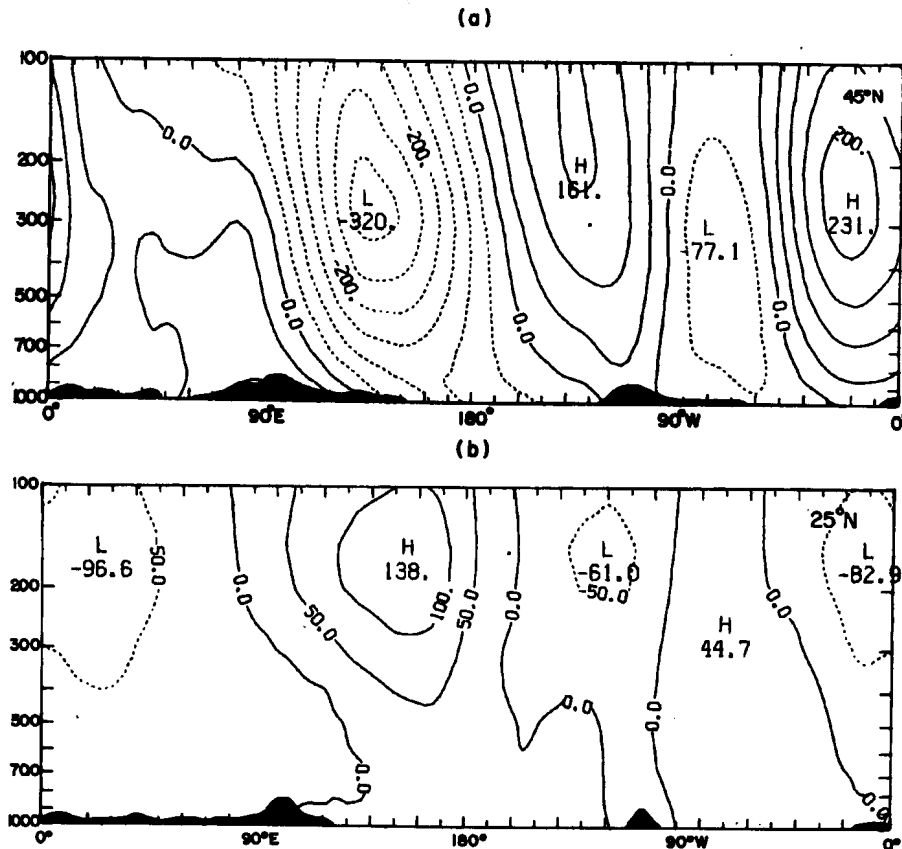


Figure 4.2: Longitude-height cross-sections of the departure from zonal symmetry of the time-averaged geopotential height taken along (a) 45°N and (b) 25°N . The contour interval is 50 m. The local orography is depicted at the bottom of the figures. (From Gill, 1982)

4.1 The Held-Hou Model of the Hadley Circulation.

The Held-Hou model is symmetric about the equator and assumes steady, linear, axisymmetric flow in hydrostatic balance. The main features of the model are a simplified representation of solar heating and the use of angular momentum conservation and thermal wind balance. *The model aims to predict the strength and the width of the Hadley circulation.*

The Held-Hou model is a two-level model on the sphere with equatorward flow at the surface and poleward flow at height H , as illustrated in Fig. 4.3. The radius of the earth is a , the angular velocity of the earth Ω , and the latitude φ . The thermal structure is described by the mid-level potential temperature, θ . Radiative processes are represented in the model using a Newtonian cooling formulation in which the potential temperature of the model is driven towards a prescribed radiative equilibrium potential temperature profile, θ_E , on a time scale τ_E . Mathematically, we write

$$\frac{D\theta}{Dt} = \frac{\theta_E - \theta}{\tau_E}, \quad (4.1)$$

where

$$\theta_E(\varphi) = \theta_0 - \frac{1}{3} \Delta\theta (3 \sin^2 \varphi - 1). \quad (4.2)$$

In the latter expression, θ_0 is the global mean radiative equilibrium temperature and $\Delta\theta$ the equilibrium pole-to-equator temperature difference.

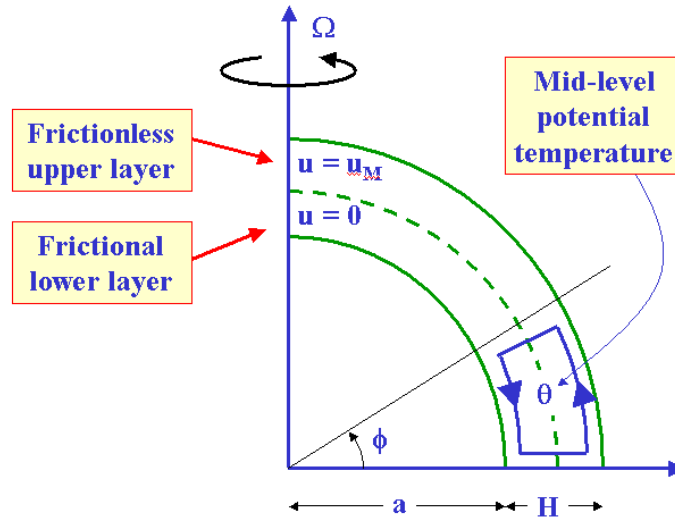


Figure 4.3: Schematic illustration of the Held-Hou model. (From James, 1994)

It is assumed that, as a result of friction at the ground, the zonal wind at the surface is much smaller than the zonal wind at height H and can be neglected. The zonal flow at height H , U_M , is calculated on the assumption of conservation of angular momentum as follows. Let u be the zonal velocity of a ring of air at latitude φ . Then the specific² absolute angular momentum of the ring is given by $(\Omega a \cos \varphi + u)a \cos \varphi$, where a is the radius of the earth (see Fig. 4.4).

If we assume that $u = 0$ at the equator, the zonal flow at latitude φ is given by

²Specific means per unit mass.

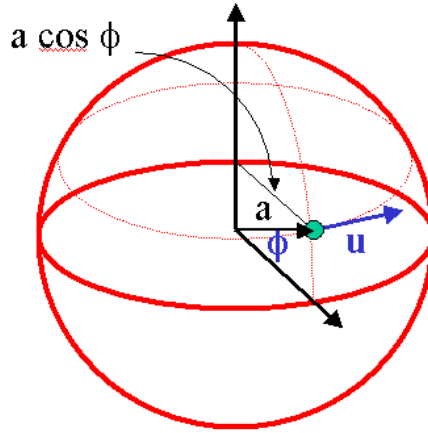


Figure 4.4: Illustrating the absolute angular momentum of a parcel in spherical coordinates. The relative angular momentum is $ua \cos \phi$ and the angular momentum associated with the Earth's rotation is $\Omega(a \cos \phi)^2$.

$$u(\varphi) = \Omega a \frac{\sin^2 \varphi}{\cos \varphi}. \quad (4.3)$$

We simplify the algebra by assuming that φ is small (i.e. $\varphi \approx \sin \varphi \approx y/a$). Thus (4.2) becomes

$$\theta_E(y) = \theta_{E0} - \Delta\theta \frac{y^2}{a^2}, \quad (4.4)$$

with $\theta_{E0} = \theta_0 + \Delta\theta/3$ and from (4.3), the upper-level zonal wind is

$$U_M = \frac{\Omega}{a} y^2. \quad (4.5)$$

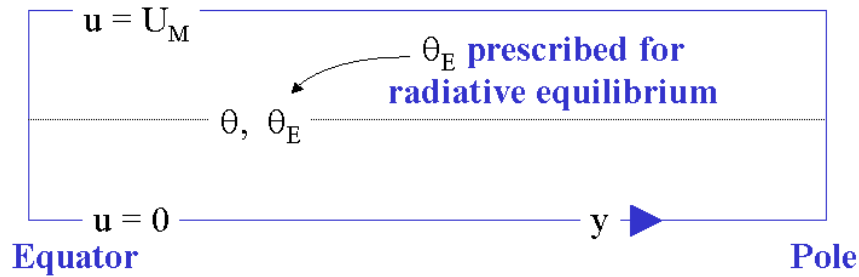


Figure 4.5: Rectangular configuration of the Held-Hou model.

The rectangular configuration of the model is sketched in Fig. 4.5. The potential temperature structure at the middle level of the model is calculated from thermal

wind balance³. With the assumptions of steady, linear, axisymmetric flow in hydrostatic balance, the thermal wind relation is satisfied even at low latitudes. As we have assumed that the zonal flow at the surface is much smaller than that at upper levels, the vertical shear in the zonal direction is

$$\frac{\partial u}{\partial z} = \frac{U_M}{H} = \frac{\Omega}{aH} y^2.$$

Then thermal wind balance gives the meridional potential temperature gradient

$$\frac{\partial \theta}{\partial y} = -\frac{2\Omega^2 \theta_0}{a^2 g H} y^3.$$

We can integrate this expression to obtain the potential temperature field

$$\theta_M = \theta_{M0} - \frac{\Omega^2 \theta_0}{2a^2 g H} y^4, \quad (4.6)$$

where the constant of integration, θ_{M0} , is the temperature at the equator. The subscript M is used here to remind us that the potential temperature field has been derived using conservation of angular momentum.

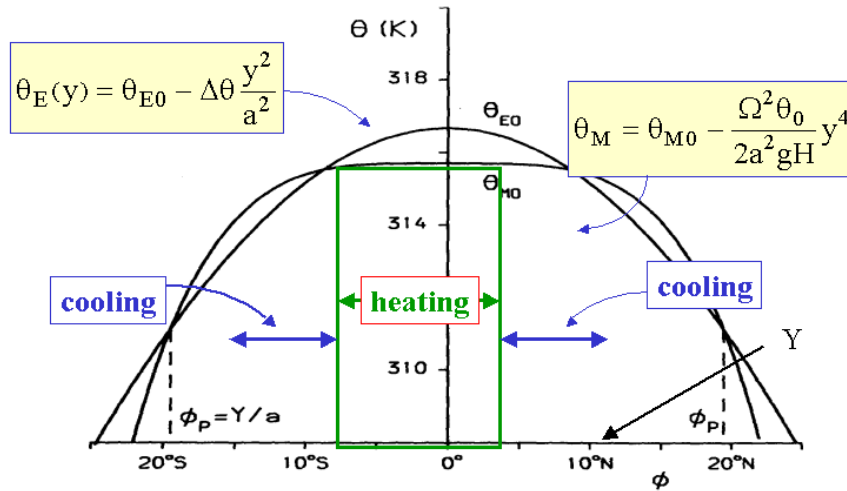


Figure 4.6: Showing θ_E and θ_M as a function of poleward distance for the Held and Hou model. The constant θ_{M0} must be chosen so that the areas between the two curves are equal, i.e. so that there is no net heating of air parcels. (Adapted from James, 1994).

Figure 4.6 shows the equilibrium temperature, θ_E , and the model temperature, θ_M . The temperature curves intersect each other twice in each hemisphere, with

³The approximation used is that $f(\partial u / \partial z) = -(g / \theta_0)(\partial \theta / \partial y)$, where θ is the potential temperature, θ_0 is some reference potential temperature, $f = 2\Omega \sin \phi \approx 2\Omega y / a$, and g is the acceleration due to gravity.

$\theta_E > \theta_M$ between the equator and the first crossing point, and $\theta_E < \theta_M$ between the first and second crossing points. From (4.1) we see that there is heating between the equator and the first crossing point, and cooling between the equator and the second crossing point. Heating occurs at latitudes higher than the second crossing point. Since this is unphysical we assume that the second crossing point, $y = Y$, marks the poleward boundary of the Hadley circulation. For $y > Y$ the temperature is given by the radiative equilibrium temperature, θ_E .

We have now two unknowns: the width of the Hadley cell, Y , and the equatorial temperature, θ_{M0} (see Fig. 4.7). Since the model assumes a steady state, there can be no net heating of an air parcel when it completes a circuit of the Hadley cell, i.e.

$$\int_0^Y \frac{D\theta}{Dt} dy = 0,$$

and from (4.1), assuming that τ_E is a constant,

$$\int_0^Y \theta_M dy = \int_0^Y \theta_E dy.$$

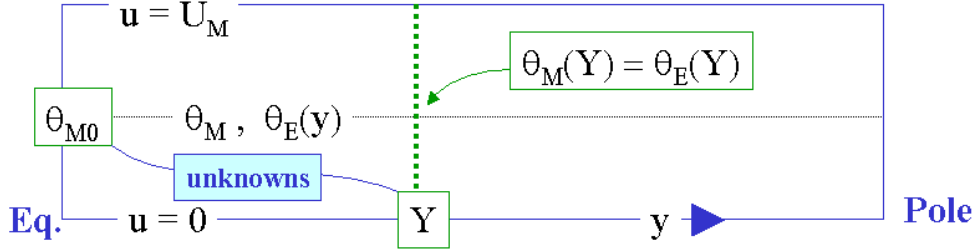


Figure 4.7: The unknowns in the Held-Hou problem and the constraint at $y = Y$.

Using (4.4) and (4.6) we obtain

$$\theta_{M0} - \frac{\Omega^2 \theta_0}{10a^2 g H} Y^4 = \theta_{E0} - \frac{\Delta \theta}{3a^2} Y^2. \quad (4.7)$$

We assume continuity of potential temperature at $y = Y$ so that $\theta_M(Y) = \theta_E(Y)$. This gives

$$\theta_{M0} - \frac{\Omega^2 \theta_0}{2a^2 g H} Y^4 = \theta_{E0} - \frac{\Delta \theta}{a^2} Y^2. \quad (4.8)$$

From (4.7) and (4.8) we obtain the width of the Hadley cell

$$Y = \left(\frac{5\Delta\theta g H}{3\Omega^2 \theta_0} \right)^{1/2}, \quad (4.9)$$

and the equatorial temperature

$$\theta_{M0} = \theta_{E0} - \frac{5\Delta\theta^2 gH}{18a^2\Omega^2\theta_0}. \quad (4.10)$$

Taking $\theta_0 = 255$ K, $\Delta\theta = 40$ K, and $H = 12$ km gives the width of the Hadley cell to be approximately 2400 km and the equatorial temperature to be about 0.9 K cooler than the equilibrium equatorial temperature. The width of the Hadley cell from the simple model is roughly in agreement with observations (see Fig. 4.1), although it is somewhat too small.

The meridional variation of the zonal wind is given by (4.5) for $y \leq Y$ (see Fig. 4.8). The zonal wind increases quadratically with y to reach a maximum value of approximately 66 ms^{-1} at $y = Y$. At higher latitudes the zonal wind can be calculated from thermal wind balance using the equilibrium temperature θ_E given by (4.4). This gives the zonal wind for $y \geq Y$

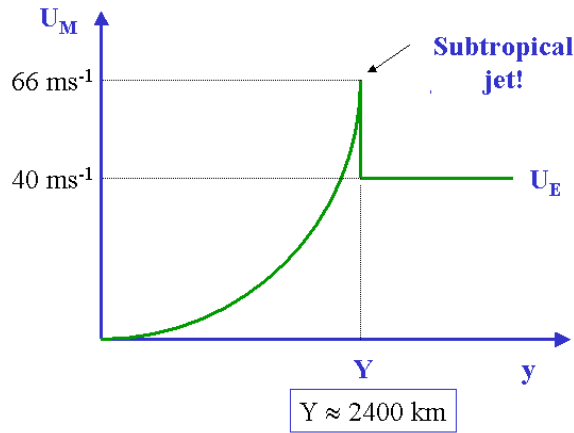


Figure 4.8: Zonal wind structure, $U(y)$, in the solution of the Held-Hou model.

$$U_E = \frac{\Delta\theta gH}{\Omega a\theta_0}. \quad (4.11)$$

For the parameter values given above U_E is 40 m s^{-1} . Thus we see that there is a discontinuity in the zonal wind at the poleward boundary of the Hadley circulation. Although this discontinuity is not physical we could think of it as representing the upper-level jet observed in nature. Such a sharp jet would not be observed either in nature or in a more sophisticated model since it would be very unstable.

The strength of the Hadley circulation in the Held-Hou model can be estimated as follows. By symmetry, $v = 0$ at the equator and (4.1) can be expressed as

$$w \frac{\partial\theta}{\partial z} = \frac{\theta_{E0} - \theta_{M0}}{\tau_E}.$$

Assuming constant Brunt-Väisälä frequency, N , the middle-troposphere vertical velocity at the equator, $w_{H/2}$ is given by

$$w_{H/2} = \frac{g}{\theta_0 N^2} \frac{(\theta_{E0} - \theta_{M0})}{\tau_E}.$$

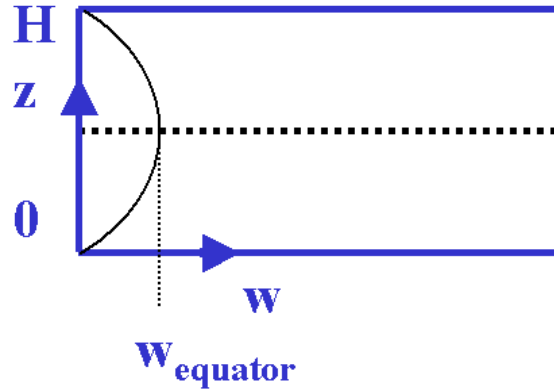


Figure 4.9: Zonal wind structure, $U(y)$, in the solution of the Held-Hou model.

Using $\tau_E \sim 15$ days and $N \sim 10^{-2} \text{ s}^{-1}$ gives $w_{H/2} \sim 0.27 \text{ mm s}^{-1}$. Assuming that the vertical velocity varies quadratically with height, i.e., $w = 4w_{H/2}z(H - z)/H^2$, then $(\partial w/\partial z)_{z=H} = -4w_{H/2}/H$ (see Fig. 4.9). From continuity, $v_{z=H} \sim 4Yw_{H/2}/H \sim 21.6 \text{ cm s}^{-1}$. Observations show that the strength of the meridional flow in the Hadley circulation is approximately 1 m s^{-1} . Thus although the Held-Hou model provides a reasonable estimate of the geometry of the Hadley circulation it gives a poor estimate of the strength of the circulation. Part of the reason may be the use of the Boussinesq approximation.

The Held-Hou model predicts that the width of the Hadley cell is inversely proportional to the planetary rotation rate (see (4.9)). This prediction has been confirmed in more realistic models of planetary atmospheres. At low rotation rates the Hadley cells extend far polewards and account for most of the heat transport from equator to pole. At high rotation rates the Hadley cells are confined near the equator and baroclinic waves polewards of the Hadley circulations are responsible for a significant proportion of the heat transport. For more details see, for example, James (1994, Ch. 10).

4.2 Extensions to the Held-Hou Model

Although the Held-Hou model gives a reasonable estimate for the size of the Hadley circulation it gives a very poor estimate of its strength. A better model can be formulated by relaxing one of the assumptions of the Held-Hou model, namely that of

symmetry about the equator. Although the annual mean solar heating is symmetric about the equator, the heating at any given time is generally not and thus the response to the solar forcing is not necessarily symmetric about the equator. Figure (4.1) shows that although the annual mean Hadley circulation is symmetric about the equator, the monthly mean Hadley circulation may be very asymmetric. Lindzen and Hou (1988) extended the Held-Hou model to allow for such an asymmetry whilst retaining the other assumptions described above.

The extended model is sketched in Fig. (4.10). The removal of the symmetry constraint means that the locations of maximum heating, maximum ascent, and the streamline dividing the summer and winter Hadley cells need not coincide. The solar heating is maximum at $y = Y_0$. The streamline dividing the summer and winter cells is located at $y = Y_1$ and the poleward extent of the summer and winter cells are given by Y_+ and Y_- respectively. Radiative processes are represented by (4.1) as before, but the equilibrium potential temperature is given by

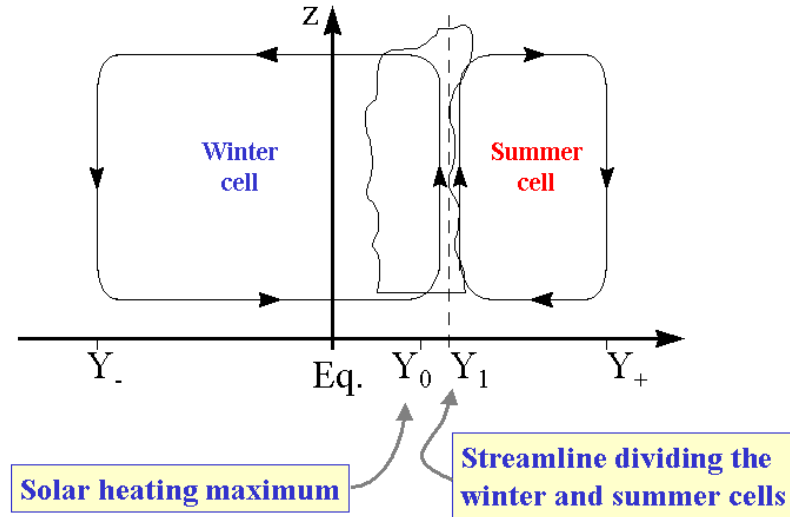


Figure 4.10: Schematic illustration of the Held-Hou model without the assumption of symmetry about the equator. Y_0 denotes the latitude of maximum heating, Y_1 the dividing streamline between the summer and winter cells. Y_+ and Y_- give the poleward extent of the summer and winter cells respectively.

$$\theta_E = \theta_{E0} - \frac{\Delta\theta}{a^2} (y^2 - Y_0^2). \quad (4.12)$$

so that θ_E is maximum at Y_0 . Conservation of angular momentum is used as before to calculate the upper-level zonal flow, with the assumption that the zonal wind is zero at the dividing streamline between the winter and summer cells, i.e. at $y = Y_1$. The upper-level zonal flow for small y is

$$U_M = \frac{\Omega}{a} (y^2 - Y_1^2). \quad (4.13)$$

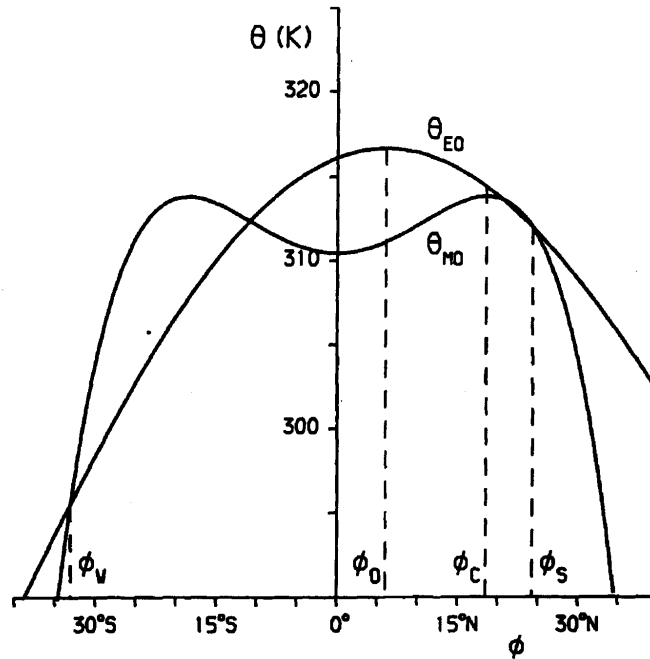


Figure 4.11: The Held-Hou model for asymmetric heating with maximum value at 6° N. Here ϕ_W, ϕ_0, ϕ_C and ϕ_S correspond with Y_-, Y_0, Y_1 and Y_+ in Fig. (4.10). (From James, 1994)

Using thermal wind balance we obtain the potential temperature

$$\theta_M(y) = \theta_M(Y_1) - \frac{2\theta_0\Omega^2}{4a^2gH} (y^2 - Y_1^2)^2. \quad (4.14)$$

Note that both U_M and θ_M are asymmetric about the equator. The asymmetry in the solution arises from the different size of the summer and winter cells. For $|y| < |Y_1|$, Eq. (4.13) gives $U_M < 0$, i.e. there are upper-level easterlies at the equator. The form of θ_E and θ_M is shown in Fig. (4.11). The poleward extent of each Hadley cell is defined as the second crossing point of the two potential temperature curves to the north or south of the latitude of maximum heating. Note that the magnitude of heating and cooling in the summer cell is much smaller than that in the winter cell. Figure (4.11) shows a strong asymmetry in the size of the summer and winter cells when the maximum heating is at 6° N.

We have now four unknowns: Y_1, Y_+, Y_- , and $\theta_M(Y_1)$. These can be found using the conditions of no net heating for an air parcel completing a circuit of each cell

$$\int_{Y_-}^{Y_1} (\theta_E - \theta_M) dy = 0 \quad \text{and} \quad \int_{Y_1}^{Y_+} (\theta_E - \theta_M) dy = 0$$

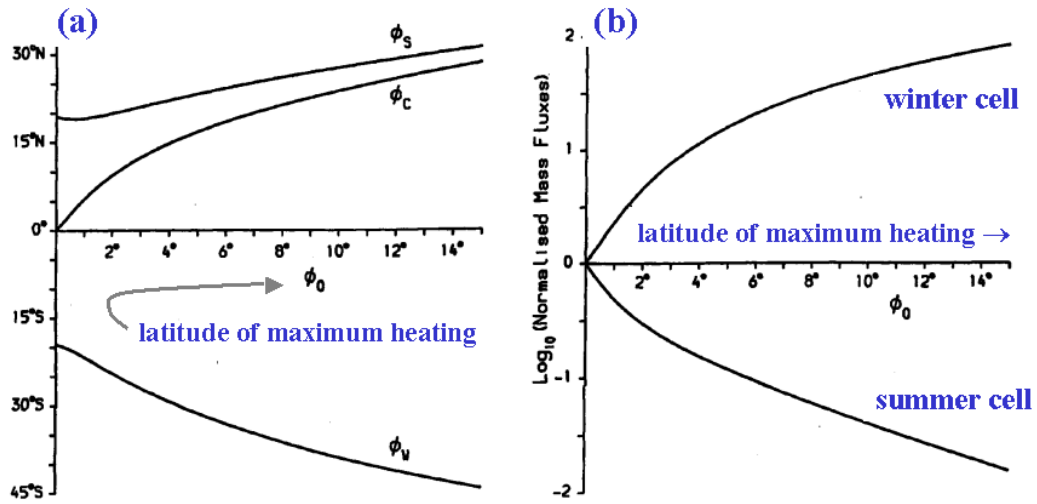


Figure 4.12: Results of the Held-Hou model for asymmetric heating with varying latitude of maximum heating. (a) Variation of the poleward extent of the summer and winter circulations and of the latitude of the dividing streamline. (b) Variation of the mass flux carried by the winter and summer cells. Here φ_W , φ_0 , φ_C and φ_S correspond with Y_- , Y_0 , Y_1 and Y_+ in Fig. (4.10). (From James, 1994)

and of continuity of potential temperature at $y = Y_+$ and $y = Y_-$.

The poleward extent of the two cells and the latitude of the dividing streamline are shown in Fig. (4.12a) for varying latitude of maximum heating. As the latitude of maximum heating increases the width of the summer cell decreases significantly. For maximum heating only 2° away from the equator, the winter cell is over three times as wide as the summer cell. The relative width of the winter and summer cell changes most significantly for small displacements away from the equator of the latitude of maximum heating. The dividing streamline is always polewards of the latitude of maximum heating. The mass flux in the winter and summer cells is shown in Fig. (4.12b), normalized by the mass flux for symmetric heating. As the latitude of maximum heating moves away from the equator the mass flux carried by the winter cell increases strongly and that carried by the summer cell decreases. For maximum heating 4° away from the equator the mass flux in the winter cell is over an order of magnitude larger than that in the summer cell. When the maximum heating is 6° from the equator the difference in the mass fluxes is two orders of magnitude. Figure 4.12 shows that both the strength and the width of the Hadley circulations are related to the latitude of maximum heating in a highly nonlinear manner. The Hadley circulation in the *symmetric* Held-Hou model is too weak because the annually averaged response to solar heating is much stronger than the response to the annually averaged heating. Discrepancies exist still between the results of this simple model and the observations. For example, the upper-level equatorial easterlies are too strong. However, it is perhaps more surprising that

the model can reproduce many of the observed features of the zonally symmetric circulation, when one considers the nature of the approximations made.

Further improvements to the Held-Hou model can be made by including the effects of friction in the upper atmosphere and of moisture. Inclusion of these effects in the axisymmetric framework is discussed in James (1994 Section 4.3).

A more serious drawback of such simple models of large-scale overturning is that they are not consistent with the observed vertical profile of equivalent potential temperature, as discussed by Holton (1992, Ch. 11). The simple model requires air from the lower troposphere to rise uniformly and then move polewards, transporting heat from equator to pole. The vertical profile of equivalent potential temperature, θ_e , in the tropics (Fig. 4.13) exhibits a mid-tropospheric minimum. Large-scale ascent in this environment would lead to an increase in θ_e in the lower troposphere and a decrease in the upper troposphere, in other words, the observed distribution of θ_e could not be maintained.

In reality the ascending motion of the Hadley circulation takes place in deep convection in the ITCZ. Air parcels from the boundary layer which ascend in cumulonimbus towers through the environment shown in Fig. (4.13) can arrive at the tropopause with positive buoyancy. Riehl and Malkus (1958) estimated that of the order of 1500 - 5000 cumulonimbus towers are required simultaneously around the ITCZ to account for the required vertical heat transport.

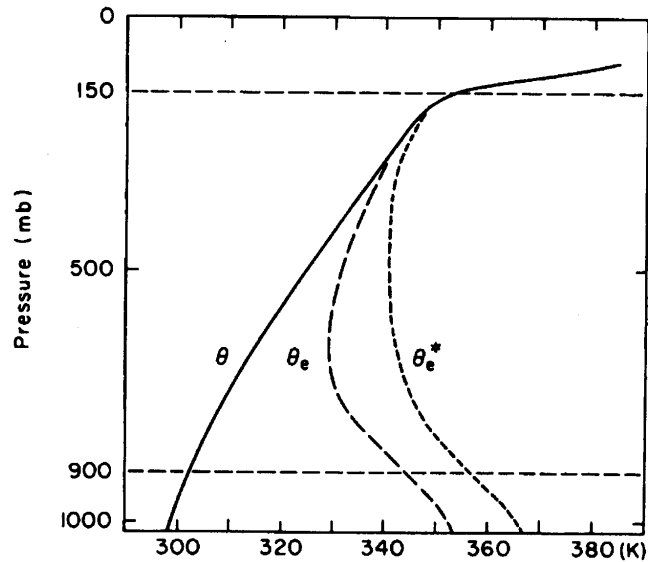


Figure 4.13: Typical sounding in the tropical atmosphere showing the vertical profiles of potential temperature θ , equivalent potential temperature θ_e , and the saturated equivalent potential temperature θ_e^* . (From Holton (1992), after Ooyama, 1969)

Chapter 5

WAVES AT LOW LATITUDES

A characteristic of the atmosphere is its shallow depth; 99% of the mass lies below a height of 30 km whereas the mean earth radius is 6,380 km. Over this 30 km which extends into the middle stratosphere there is a considerable variation in the vertical structure. However much can be learned about low latitude motions by considering the atmosphere to be a uniform layer of fluid with variable depth. Put another way, consideration of the *horizontal structure* of the vertical mean atmosphere yields rich information about the predominant wave modes, especially at low latitudes. The classical papers on this subject are those of Matsuno (1966) and Longuet-Higgins (1968) with important contributions also from Webster (1972) and Gill (1980) amongst others. A recent review is given by Lim and Chang (1987).

Although we begin our study by assuming a uniform vertical structure, we shall find that the effort is not in vain for it turns out that the solutions to the divergent barotropic system are, in fact, the horizontal part of the *baroclinic* modes.

In contrast to Longuet-Higgins (1968) and Webster (1972) who use full-spherical geometry, we follow Matsuno (1966) and Gill (1980) and consider motions on an equatorial beta plane. To begin with, we review the theory of wave motions in a divergent barotropic fluid on an f -plane or on a mid-latitude β -plane as described in DM, Chapter 11. The basic flow configuration is shown in Fig. 5.1. The fluid layer has undisturbed depth H .

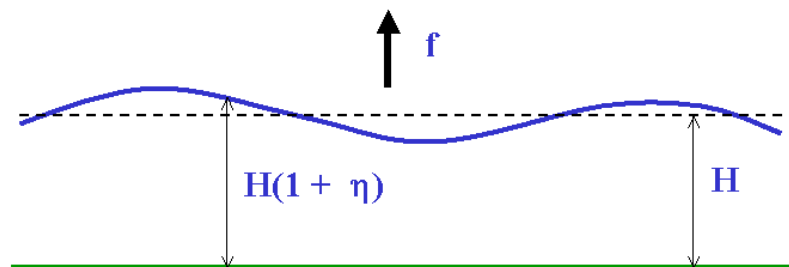


Figure 5.1: Configuration of a one-layer fluid model with a free surface.

We consider small amplitude perturbations about a state of rest in which the free surface elevation is $H(1 + \eta)$. As shown in DM, the linearized “shallow-water” equations take the form

$$\frac{\partial u}{\partial t} - fv = -c^2 \frac{\partial \eta}{\partial x}, \quad (5.1)$$

$$\frac{\partial v}{\partial t} + fu = -c^2 \frac{\partial \eta}{\partial y}, \quad (5.2)$$

$$\frac{\partial \eta}{\partial t} + \frac{\partial u}{\partial x} + \frac{\partial v}{\partial y} = 0, \quad (5.3)$$

where $c = \sqrt{gH}$ is the phase speed of long waves in the absence of rotation ($f = 0$).

On an f -plane, Eqs. (5.1) - (5.3) have sinusoidal travelling wave solutions in the x -direction with *wavelength* $2\pi/k$ and *period* $2\pi/\omega$ (*wavenumber* k , *frequency* ω) of the form

$$v = \hat{v} \sin(kx - \omega t) \quad (5.4)$$

$$(u, \eta) = (\hat{u}, \hat{\eta}) \cos(kx - \omega t), \quad (5.5)$$

where \hat{u} , \hat{v} , $\hat{\eta}$ are constants, provided

$$\omega (\omega^2 - f^2 - c^2 k^2) = 0. \quad (5.6)$$

This dispersion relation yields $\omega = 0$, which corresponds with a steady ($\partial/\partial t = 0$) geostrophic flow, or $\omega^2 = f^2 + c^2 k^2$, corresponding with inertia - gravity waves. The phase speed of these waves, c_p , is given by

$$c_p = \frac{\omega}{k} = \pm \sqrt{\left(c^2 + \frac{f^2}{k^2}\right)} = \pm c \sqrt{\left(1 + \frac{1}{L_R^2 k^2}\right)}, \quad (5.7)$$

where $L_R = c/f$ is the Rossby radius of deformation. Clearly, the importance of inertial effects compared with gravitational effects is characterized by the size of the parameter $L_R^2 k^2$, i.e. by the wavelength of waves compared with the Rossby radius of deformation.

On a mid-latitude β -plane where f is a function of y (specifically, where $f = f_0 + \beta y$, $f_0 \neq 0$), it is inconsistent to seek a solution of the form (5.4) - (5.5) with \hat{u} , \hat{v} and $\hat{\eta}$ as constants, unless meridional particle displacements are relatively small. In that case, the effects of variable f can be incorporated by replacing the second equation of (5.1) - (5.3) by the vorticity equation

$$\frac{\partial \zeta}{\partial t} + \beta v = f_0 \frac{\partial v}{\partial t}, \quad (5.8)$$

where

$$\zeta = \frac{\partial v}{\partial x} - \frac{\partial u}{\partial y}, \quad (5.9)$$

Note that variations of f are included only in so much as they appear in the advection of planetary vorticity by the meridional velocity component. Substituting again (5.4) into (5.1), (5.8) and (5.9) shows that, solutions are possible now only if ω satisfies the equation

$$(\omega^2 - c^2 k^2) (\omega k + \beta) - f_0^2 \omega k = 0. \quad (5.10)$$

It is convenient to scale ω by f_0 and k by $1/L_R$, say $\omega = f_0 \nu$, $k = m/L_R$. Then (5.10) reduces to

$$(\nu^2 - \mu^2)(\nu\mu + \varepsilon) - \nu\mu = 0 \quad (5.11)$$

where $\varepsilon = \beta L_R / f_0$. At latitude 45° , $\beta / f_0 = 1/a$, where a is the earth's radius. It follows that for Rossby radii $L_R \ll a$, then $\varepsilon \ll 1$.

When $\varepsilon = 0$, implying that $\beta = 0$, Eq. (5.11) has solutions $\nu = 0$ and $\nu = \mu^2 + 1$ as before.

If $\varepsilon \ll 1$, there is a root of $0(\varepsilon)$ which emerges if we set $\nu = \varepsilon \nu_0$, where ν_0 is $0(1)$ and neglect higher powers of ε . It follows easily that

$$\nu = -\frac{\varepsilon \mu}{1 + \mu^2} \quad (5.12)$$

which in dimensional form, $\omega = -\beta k / [k^2 + 1/L_R^2]$, is the familiar dispersion relation for *divergent Rossby waves*. The other two roots for small ε are the same as when $\varepsilon = 0$, and again correspond with inertia-gravity wave modes. We consider now a rather special wave type that owes its existence to the presence of a boundary - the so-called Kelvin wave. Consider the flow configuration on an f -plane sketched in Fig. 5.2. The equation set (5.1) - (5.3) has a solution in which $v \equiv 0$. In that case, they reduce to

$$\frac{\partial u}{\partial t} = -c^2 \frac{\partial \eta}{\partial x}, \quad (5.13)$$

$$f u = -c^2 \frac{\partial \eta}{\partial y}, \quad (5.14)$$

$$\frac{\partial \eta}{\partial t} + \frac{\partial u}{\partial x} = 0. \quad (5.15)$$

Cross-differentiating (5.13) and (5.15) to eliminate u gives

$$\frac{\partial^2 \eta}{\partial t^2} = c^2 \frac{\partial^2 \eta}{\partial x^2}, \quad (5.16)$$

which has a general travelling-wave solution of the form

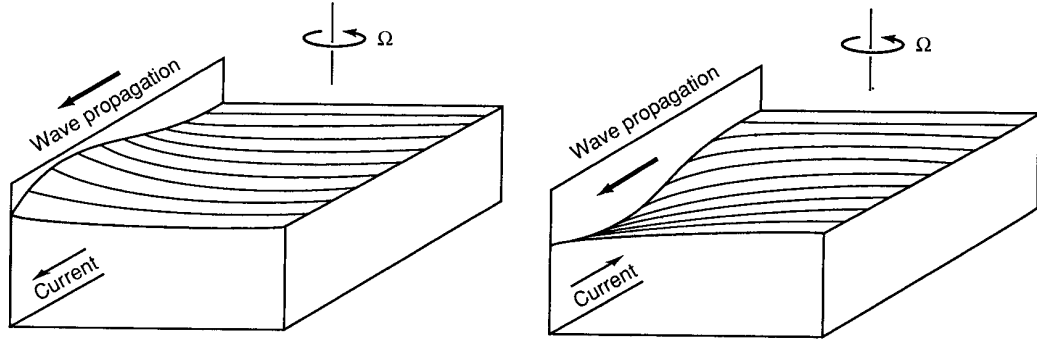


Figure 5.2: Flow configuration of a Kelvin wave.

$$\eta = F(x - ct, y) + G(x + ct, y), \quad (5.17)$$

where F and G are arbitrary functions. Define $X = x - ct$ and $Y = x + ct$. Then using (5.15) we have

$$\frac{\partial u}{\partial x} = c \left(\frac{\partial F}{\partial X} - \frac{\partial G}{\partial Y} \right) = c \left(\frac{\partial F}{\partial x} - \frac{\partial G}{\partial x} \right),$$

$$u = c(F - G), \quad (5.18)$$

which may be integrated partially with respect to x to give ignoring an arbitrary function of y and t . Substitution of (5.18) in (5.14) gives

$$fc[F - G] = c^2 \left[\frac{\partial F}{\partial y} + \frac{\partial G}{\partial y} \right],$$

and since F and G are arbitrary functions we must have

$$\frac{\partial F}{\partial y} + (f/c) F = 0, \quad (5.19)$$

and

$$\frac{\partial G}{\partial y} - (f/c) G = 0. \quad (5.20)$$

These first order equations in y may be integrated to give the y dependence of F and G , i.e.

$$F = F_0(X) e^{-fy/c}, \quad G = G_0(Y) e^{fy/c}.$$

In the configuration shown in Fig. 5.2, we must reject the solution G as this is unbounded as $y \rightarrow \infty$. In this case, the solution is

$$\eta = F_0 (x - ct) e^{-fy/c}. \quad (5.21)$$

This represents the surface elevation of a wave that moves in the *positive* x -direction with speed c and decays exponentially away from the boundary with decay scale c/f which is simply the Rossby radius of deformation, L_R . The solution for u from (5.18) is simply

$$u = cF_0 (x - ct) e^{-fy/c}. \quad (5.22)$$

The Kelvin wave is essentially a gravity wave that is “trapped” along the boundary by the rotation. The velocity perturbation u is always such that geostrophic balance occurs in the y direction, expressed by (5.14). If the fluid occupies the region $y < 0$, then the appropriate solution is the one for which $F_0 \equiv 0$ and then

$$u = cF_0 (x - ct) e^{-fy/c}. \quad (5.23)$$

Again this represents a trapped wave moving at speed c with the boundary on the right (left) in the Northern (Southern) Hemisphere when $f > 0$ ($f < 0$).

5.1 The equatorial beta-plane approximation

At the equator, $f_0 = 0$, but β is a maximum. In the vicinity of the equator, (5.1)-(5.3) must be modified by setting $f = \beta y$. This constitutes the *equatorial beta-plane approximation* that may be derived from the equations for motion on a sphere (see e.g. Gill, 1982, §11.4). The perturbation equations are now

$$\frac{\partial u}{\partial t} - \beta y v = -c^2 \frac{\partial \eta}{\partial x}, \quad (5.24)$$

$$\frac{\partial v}{\partial t} + \beta y u = -c^2 \frac{\partial \eta}{\partial y}, \quad (5.25)$$

$$\frac{\partial \eta}{\partial t} + \frac{\partial u}{\partial x} + \frac{\partial v}{\partial y} = 0, \quad (5.26)$$

$$\frac{\partial}{\partial t} (\zeta - f\eta) + \beta v = 0, \quad (5.27)$$

where again

$$\zeta = \frac{\partial v}{\partial x} - \frac{\partial u}{\partial y}. \quad (5.28)$$

Taking

$$-\frac{\beta y}{c} \frac{\partial}{\partial t} (5.24) + \frac{1}{c} \frac{\partial^2}{\partial t^2} (5.25) - c \frac{\partial^2}{\partial y \partial t} (5.26) - c \frac{\partial}{\partial x} (5.27)$$

and using (5.28) and remembering that $f = \beta y$ gives

$$\frac{\partial}{\partial t} \left[\frac{1}{c^2} \left(\frac{\partial^2 v}{\partial t^2} + f^2 v \right) - \left(\frac{\partial^2 v}{\partial x^2} + \frac{\partial^2 v}{\partial y^2} \right) \right] - \beta \frac{\partial v}{\partial x} = 0, \quad (5.29)$$

which has only the dependent variable v . We follow the usual procedure and look for travelling-wave solutions of the form

$$v = \hat{v}(y) \exp [i(kx - \omega t)], \quad (5.30)$$

whereupon $\hat{v}(y)$ has to satisfy the ordinary differential equation obtained by substituting (5.30) into (5.29). Note that, unlike the previous case we cannot assume that \hat{v} is a constant because Eq.(5.29) has a *coefficient* (namely f^2) that depends on y . The equation for $\hat{v}(y)$ is

$$\frac{d^2 \hat{v}}{dy^2} + \left[\frac{\omega^2}{c^2} - k^2 - \frac{\beta k}{\omega} - \frac{\beta^2 y^2}{c^2} \right] \hat{v} = 0. \quad (5.31)$$

Before attempting to find solutions to this equation we scale the *independent* variables t, x, y , using the time scale $(2\beta c)^{-1/2}$ and length scale $(c/2\beta)^{-1/2}$, the latter defining the *equatorial Rossby radius* L_E . This scaling necessitates scaling $\omega = (2c\beta)^{-1/2} \nu$ and $k = \mu(c/2\beta)^{-1/2}$ also. Then the equation becomes

$$\frac{d^2 \hat{v}}{dy^2} + \left[\nu^2 - \mu^2 - \frac{\mu}{\nu} - y^2 \right] \hat{v} = 0 \quad (5.32)$$

which is the same form as Schrödinger's equation that arises in the theory of quantum mechanics. The solutions are discussed succinctly by Sneddon (1961, see especially Chapter V). A brief sketch of the main results that we require are given in an appendix to this chapter. There it is shown that solutions for \hat{v} that are bounded as $|y| \rightarrow \infty$ are possible only if

$$\nu^2 - \mu^2 - \mu \nu^{-1} = 2n + 1, \quad (n = 0, 1, 2, \dots). \quad (5.33)$$

These solutions have the form of parabolic cylinder functions. In dimensional terms,

$$v(x, y, t) = H_n \left((2\beta/c)^{1/2} y \right) \exp \left(-\beta y^2 / 2c \right) \cos(kx - \omega t), \quad (5.34)$$

which on multiplication by $2^{-n/2}$ can be written as

$$v(x, y, t) = D_n \left((2\beta/c)^{1/2} y \right) \cos(kx - \omega t), \quad (5.35)$$

where D_n is the parabolic cylinder function of order n and H_n is the Hermite polynomial of order n . In dimensional form the corresponding dispersion relation, (5.33), is

$$\omega^2 / c^2 - k^2 - \beta k / \omega = (2n + 1) \beta / c. \quad (5.36)$$

Like (5.10), this is a cubic equation for ω for each value of n and evidently a whole range of wave modes is possible. We shall consider the structure of these presently.

5.2 The Kelvin Wave

First we note that (5.32) has a trivial solution $\hat{v} = 0$. As in the case of the Kelvin wave discussed earlier, this solution corresponds with a nontrivial wave mode. To see this we substitute $\hat{v} = 0$ into Eqs. (5.24) - (5.26) to obtain

$$\frac{\partial u}{\partial t} = -c^2 \frac{\partial \eta}{\partial x}, \quad (5.37)$$

$$\beta y u = -c^2 \frac{\partial \eta}{\partial y}, \quad (5.38)$$

$$\frac{\partial \eta}{\partial t} + \frac{\partial u}{\partial x} = 0. \quad (5.39)$$

These equations are identical with (4.12) if we set $f = \beta y$ in (5.14). In particular the solutions for η and u are exactly the same as (5.17) and (5.18), respectively. Then (5.38) gives

$$\frac{\partial F}{\partial y} + (\beta y/c) F = 0, \quad (5.40)$$

and

$$\frac{\partial G}{\partial y} - (\beta y/c) G = 0, \quad (5.41)$$

analogous to (5.19) and (5.20). Now (5.40) has the solution

$$F = F_0(X) \exp(-\beta y^2/2c), \quad (5.42)$$

whereas the solution for G is unbounded as $y \rightarrow \pm \infty$. Therefore Eqs. (5.37) - (5.39) have a solution

$$\left. \begin{aligned} \eta(x, y, t) &= F_0(x - ct) \exp(-\beta y^2/2c), \\ u(x, y, t) &= cF_0(x - ct) \exp(-\beta y^2/2c), \\ v(x, y, t) &= 0 \end{aligned} \right\} \quad (5.43)$$

This solution is called an *equatorial Kelvin wave*. It is an eastward propagating gravity wave that is trapped in the *equatorial waveguide* by Coriolis forces. Note that it is nondispersive and has a meridional scale on the order of $L_E = (c/2\beta)^{1/2}$.

5.3 Equatorial Gravity Waves

We return now to the dispersion relation (5.36). For $n \geq 1$, the waves subdivide into two classes like the solutions of (5.10). There are two solutions for which $\beta k/\omega$ is small, whereupon the dispersion curves are given approximately by

$$\omega^2 \approx (2n + 1) \beta c + k^2 c^2. \quad (5.44)$$

The form is similar to that for inertia-gravity waves (sometimes called Poincaré waves also - e.g., in Gill, 1982). These waves are *equatorially-trapped gravity waves*, or *equatorially-trapped Poincaré waves*.

5.4 Equatorial Rossby Waves

There are solutions also of (5.36) for which ω^2/c^2 is small. Then the dispersion relation is approximately

$$\omega \approx -\beta k / [k^2 + (2n + 1) \beta / c]. \quad (5.45)$$

These modes are called equatorially trapped planetary waves or equatorially trapped Rossby waves. The various dispersion curves are plotted in Fig. 5.3. This figure includes also the dispersion curves for the case $n = 0$ described below and for the Kelvin wave.

5.5 The mixed Rossby-gravity wave

When $n = 0$, Eq. (5.33) may be written

$$(\nu + \mu) (\nu - \mu - 1/\nu) = 0. \quad (5.46)$$

The solution $\nu = -\mu$ must be excluded since it leads to an indeterminate solution for u (see later). Therefore the solutions are, in dimensional form,

$$\omega_+ = \frac{1}{2} kc + \left[\frac{1}{4} k^2 c^2 + c\beta \right]^{1/2}, \quad (5.47)$$

which represents an eastward propagating inertia-gravity wave, and

$$\omega_- = \frac{1}{2} kc - \left[\frac{1}{4} k^2 c^2 + c\beta \right]^{1/2}, \quad (5.48)$$

which represents an inertia-gravity wave if k is small and a Rossby wave if k is large (see Ex. 5.2). Note that as $k \rightarrow 0$, $\omega_- \approx -(c\beta)^{1/2}$, which agrees with the long wavelength limit of the inertia-gravity wave solution (5.44), while as $k \rightarrow \infty$, $\omega_- \approx -\beta/k$, which agrees with the limit of the Rossby wave solution (5.45). The solution $n = 0$ is called therefore a *mixed Rossby-gravity wave*. The phase velocity of this mode can be either eastward or westward, but the group velocity is always eastward (Ex. 5.2). The Kelvin wave solution is sometimes called the $n = -1$ wave because (5.36) is satisfied by the Kelvin-wave dispersion relation (i.e. $\omega = kc$) when $n = -1$.

To calculate the complete structure of the various wave modes we need to obtain solutions for u and η corresponding to the solution for v in Eq. (5.34).

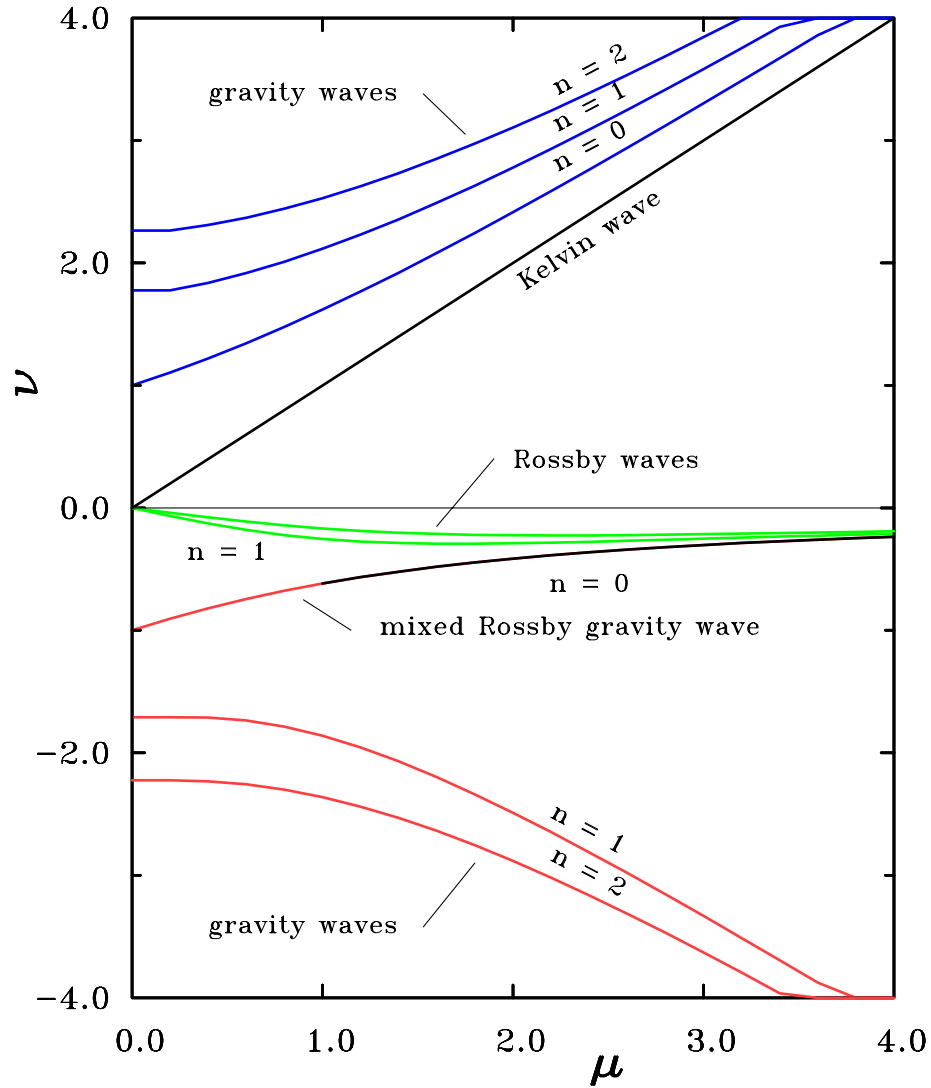


Figure 5.3: Nondimensional frequencies ν from (5.36) as a function of nondimensional wavenumber μ .

We return to the linearized equations (5.24)-(5.28). The substitution

$$v = \hat{v} \sin(kx - \omega t), \quad (u, \eta) = (\hat{u}, \hat{\eta}) \cos(kx - \omega t)$$

in (5.24) and (5.26) gives

$$\omega \hat{u} - \beta y \hat{v} = kc^2 \hat{\eta}, \quad (5.49)$$

$$\omega \hat{\eta} - k \hat{u} + \frac{d\hat{v}}{dy} = 0, \quad (5.50)$$

which may be solved for \hat{u} and $\hat{\eta}$ in terms of \hat{v} and $d\hat{v}/dy$, i.e.,

$$(\omega^2 - k^2 c^2) \hat{u} = \omega \beta y \hat{v} - k c^2 \frac{d\hat{v}}{dy}, \quad (5.51)$$

$$(\omega^2 - k^2 c^2) \hat{\eta} = k \beta y \hat{v} - \omega \frac{d\hat{v}}{dy}. \quad (5.52)$$

With the previously introduced scaling and $y = L_E Y$, these become

$$(\nu^2 - \mu^2) \hat{u} = \nu Y \hat{v} - \mu \frac{d\hat{v}}{dY}, \quad (5.53)$$

and

$$(\nu^2 - \mu^2) \hat{\eta} = \mu Y \hat{v} - \nu \frac{d\hat{v}}{dY}. \quad (5.54)$$

Also, from (5.34)

$$\hat{v}(Y) = \hat{v}_n = \exp\left(-\frac{1}{2}Y^2\right) H_n(Y), \quad (5.55)$$

whereupon

$$\frac{d\hat{v}}{dY} = -Y \hat{v}_n + \exp\left(-\frac{1}{2}Y^2\right) \frac{dH_n}{dY}. \quad (5.56)$$

We use now two well-known properties of the Hermite polynomials:

$$\frac{dH_n}{dY} = 2nH_{n-1}(Y), \quad (5.57)$$

and

$$H_{n+1}(Y) = 2YH_n(Y) - 2nH_{n-1}(Y). \quad (5.58)$$

It follows that

$$(\nu^2 - \mu^2) \hat{u}_n = \frac{1}{2}(\nu + \mu) \hat{v}_{n+1} + n(\nu - \mu) \hat{v}_{n-1} \quad (5.59)$$

and

$$(\nu^2 - \mu^2) \hat{\eta}_n = \frac{1}{2}(\nu + \mu) \hat{v}_{n+1} - n(\nu - \mu) \hat{v}_{n-1} \quad (5.60)$$

Figure 5.4 shows the horizontal structure of the Kelvin wave and of a westward propagating mixed Rossby-gravity wave. Air parcels move parallel to the equator in the case of the Kelvin wave and move clockwise around elliptical orbits in the case of the mixed wave. Plots for other equatorial wave modes are shown in Figs. 5.5 and 5.6.

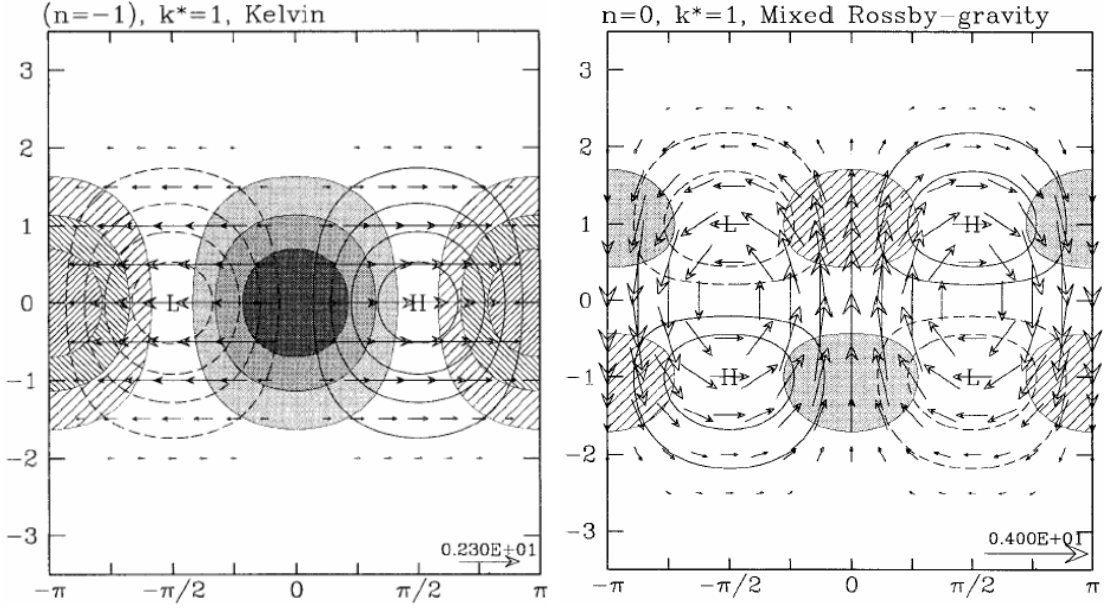


Figure 5.4: The theoretical equatorially-trapped Kelvin wave solution (panel a) and mixed Rossby gravity wave solution (panel b) to the shallow water equations on an equatorial β -plane for a nondimensional zonal wavenumber 1. Hatching is for convergence and shading for divergence, with a 0.6 unit interval between successive hatching and shading, and with the zero divergence contour omitted. Unshaded contours are for geopotential, with a contour interval of 0.5 units. Negative contours are dashed and the zero contour is omitted. The dimensional scales are as in Matsuno (1966). (From Wheeler *et al.* 2000).

5.6 The equatorial waveguide

The equatorial wave-guide equation (5.31) has the form

$$\frac{d^2\hat{v}}{dy^2} + \frac{\beta^2}{c^2} (y_c^2 - y^2) \hat{v} = 0, \quad (5.61)$$

where

$$\beta^2 y_c^2 = \omega^2 - k^2 c^2 - \frac{\beta k c^2}{\omega} = (2n + 1) \beta c, \quad (5.62)$$

using (5.36). Solutions thereto have a wave-like structure in the meridional (y -) direction if $y < y_c$ and an exponential structure if $y > y_c$. Thus y_c corresponds with a critical latitude for a particular mode, a latitude beyond which wave-like propagation is not possible. If the phase of a particular wave changes rapidly enough with y , we can define a local meridional wavenumber κ for each value of y , the assumption being that κ varies only slowly with y . One may then use the WKB

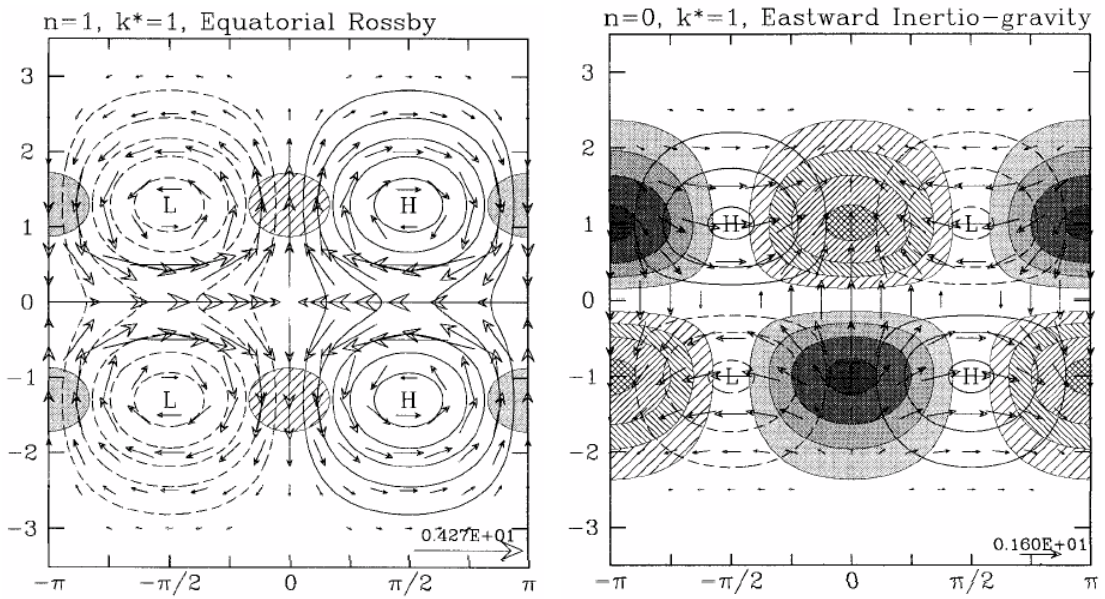


Figure 5.5: Legend as in Fig. 5.4, but for (a) Rossby wave with $n = 1$, and (b) the eastward inertia-gravity wave with $n = 0$, the westward inertia-gravity wave with $n = 1$.

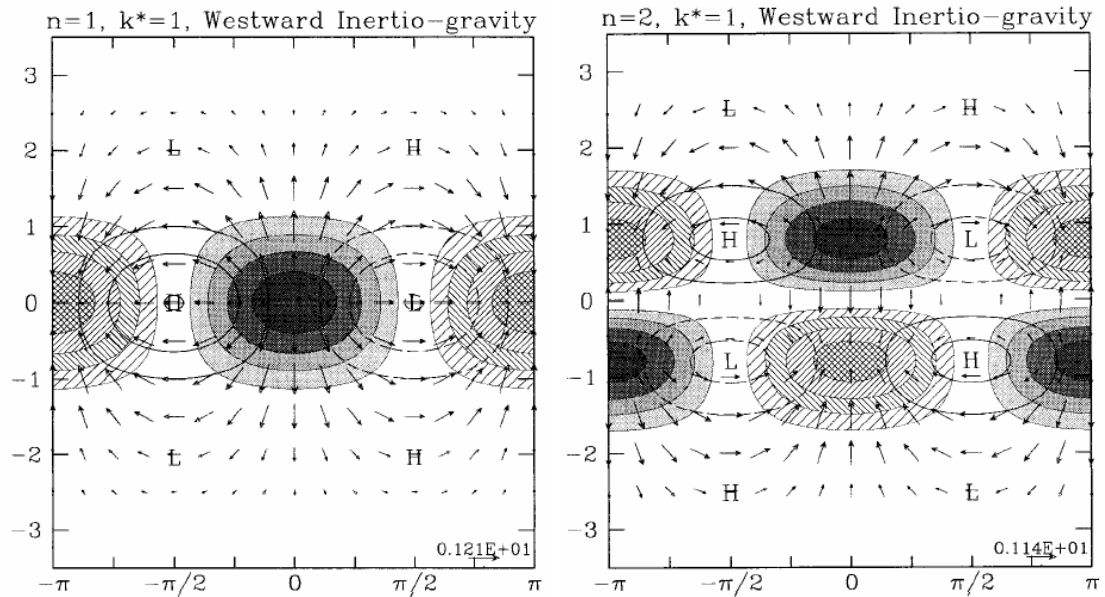


Figure 5.6: Legend as in Fig. 5.4, but for (a) the westward inertia-gravity wave with $n = 1$, and (b) the westward inertia-gravity wave with $n = 2$.

technique outlined in Gill (1982, §8.12, pp 297-302) to find approximate solutions to (5.61). Such solutions have the form

$$\hat{v} = \kappa^{-1/2} \exp \left[i \left\{ kx + \int \kappa dy - \omega t \right\} \right], \quad (5.63)$$

where

$$\kappa^2 = \frac{\beta^2}{c^2} (y_c^2 - y^2). \quad (5.64)$$

This approximate solution is valid provided that

$$\delta = \kappa^{-3/2} \frac{d^2}{dy^2} (\kappa^{-1/2}) \ll 1. \quad (5.65)$$

At the equator $\delta = 1/[2(2n+1)^2]$ i.e. the approximate solution is valid provided n is large. The group velocity of waves follows from (5.62), i.e.,

$$\mathbf{c}_g = \frac{(2k + \beta/\omega, 2\kappa)}{2\omega/c^2 + \beta k/\omega^2} \quad (5.66)$$

whereupon wave packets propagate along rays defined by $d\mathbf{x}/dt = \mathbf{c}_g$, or in this case,

$$\frac{dy}{dx} = \frac{\kappa}{k + \beta/2\omega} \quad (5.67)$$

Using (5.64) it follows readily that ray paths have the form

$$y = y_c \sin [c^{-1}\beta x / (k + \beta/2\omega)] \quad (5.68)$$

i.e., they are sinusoidal paths about the equator in which wave energy is reflected at the critical latitudes $y = \pm y_c$. Figure (6.3) shows an example of this type of behaviour for the case of gravity waves with no variation in x , i.e. $k = 0$. Then the term $\beta/2\omega$ can be ignored in (5.66) and (5.68). Since $k = 0$ the group velocity is given by

$$\mathbf{c}_g = (0, c_{gy}) = \frac{(0, 2\kappa)}{2\omega/c^2 + \beta k/\omega^2}. \quad (5.69)$$

Suppose a uniform wind stress is suddenly applied over the ocean over a small range of latitudes that are remote from the equator (5.7). This results in the generation of inertial waves. The path followed by these waves can be calculated from $dy/dt = c_{gy}$. Integration of (5.69) with respect to time shows that the path followed by the waves is sinusoidal in time about the equator (see Fig. 5.12). The waves move backwards and forwards across the equator along ray paths that are described quite well by a sinusoidal function.

Another effect of the waveguide is the discretization of modes $n = 1, 2, \dots$ in the meridional direction. For long inertia-gravity waves ($k \rightarrow 0$) this implies a discrete set of frequencies given by

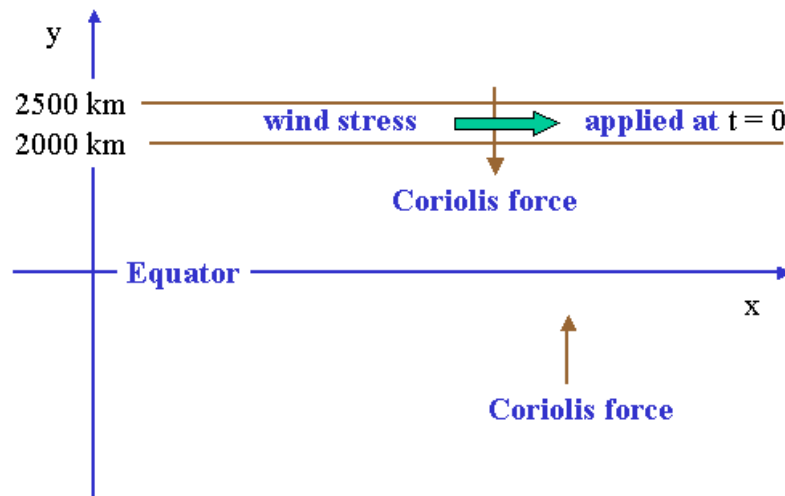


Figure 5.7: A uniform wind stress is suddenly applied over the ocean over the latitude belt between 2000 km - 2500 km north of the equator. The wave response is shown in Fig. 5.8 and discussed in the text.

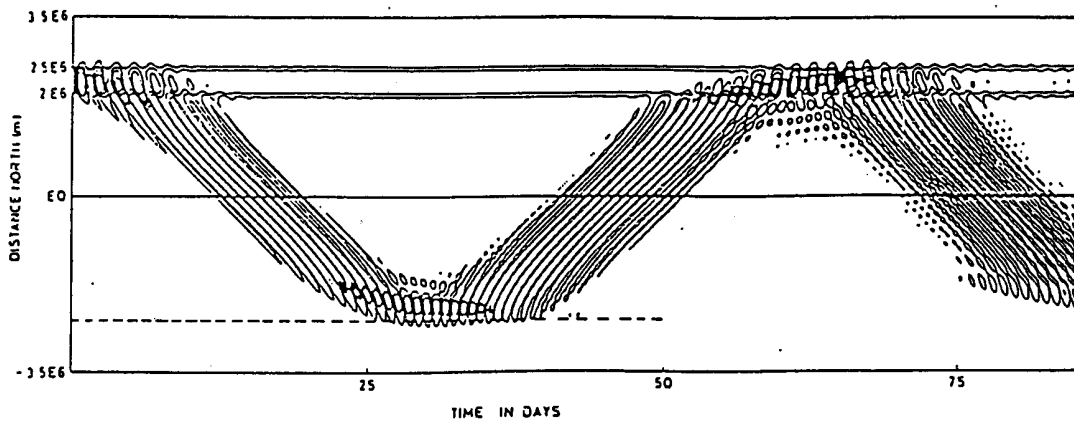


Figure 5.8: An illustration of beta dispersion of gravity waves. An eastward wind stress is applied in the strip $2000 \text{ km} < y < 2500 \text{ km}$ from $t = 0$. At first local inertial waves are generated as on an f -plane, but the variation of f with latitude causes the waves to propagate backward and forward across the equator. Contours are of the meridional velocity. (from Gill, 1982)

$$\omega^2 \approx (2n + 1) \beta c, \tag{5.70}$$

obtained from (5.62). Gill (1982, p 442) notes that this frequency selection shows up in Pacific sea-level records because variations associated with the first baroclinic

mode have magnitudes of the order of centimeters which is large enough to be detected. For these modes $c \approx 2.8 \text{ m s}^{-1}$ giving periods of $5\frac{1}{2}$, 4 and 3 days for $n = 1$, 2 and 3, respectively. See Gill (1982, p442) for further details.

5.7 The planetary wave motions

Planetary waves have the approximate dispersion relation (5.45) which, in the long-wave *limit* ($k \rightarrow 0$), is $\omega \approx -kc/(2n + 1)$. The phase speed ω/k is in the opposite direction to the Kelvin wave (i.e. westward) and the amplitudes are reduced by factors 3, 5, 7 etc. For example, for the first baroclinic mode in the Pacific Ocean, $c = 2.8 \text{ m s}^{-1}$, so that the planetary wave with $n = 1$ has speed 0.9 m s^{-1} . This mode would require 6 months to cross the Pacific Ocean from east to west. Other modes would be slower. These facts have implications for the coupled atmospheric-ocean response to perturbations in the tropics.

Figure 5.9 shows the dispersion curve (5.45) for the planetary wave modes. Differentiating (5.45) with respect to k gives

$$\frac{1}{\omega} \frac{d\omega}{dk} = \frac{1}{k} - \frac{2k}{[k^2 + (2n + 1)\beta/c]}.$$

Thus the curve has zero slope where

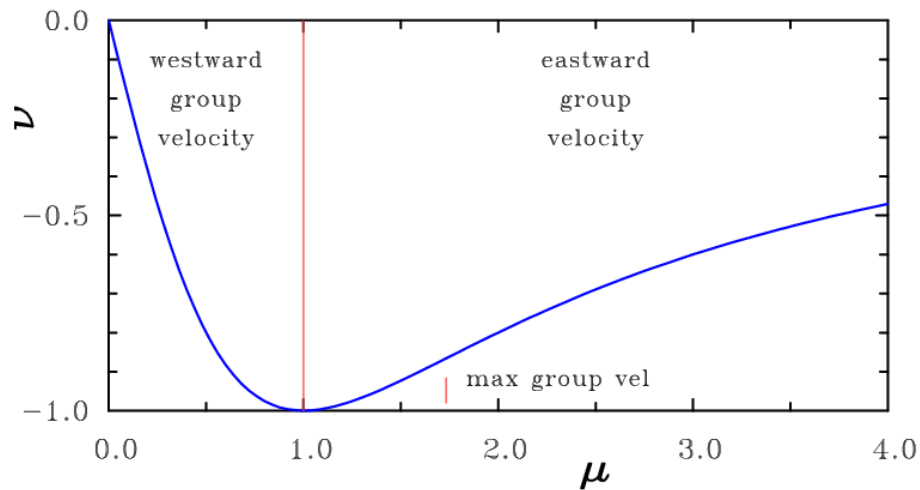


Figure 5.9: Graph of the planetary wave dispersion relation (5.45). The units are defined by the expression (5.70) and (5.71), i.e. $\mu = k/k_*$ and $v = \omega/\omega_*$.

$$k_* = (2n + 1)^{1/2}/L_E = f_c/c, \quad (5.71)$$

$f_c = \beta y_c$, and y_c is defined by (5.62).

At the point $k = k_*$ the frequency has a *maximum* absolute value

$$\omega_* = \frac{1}{2}\beta/[(2n+1)\beta/c]^{1/2} = \frac{1}{2}\beta c/f_c. \quad (5.72)$$

For example when $n = 1$, this corresponds to a minimum period of 31 days for a first baroclinic ocean mode with $c = 2.8 \text{ m s}^{-1}$, 74 days for a higher mode with $c = 0.5 \text{ m s}^{-1}$, and 12 days for an atmospheric mode with $c = 20 \text{ m s}^{-1}$.

For waves with wavelength shorter than $2\pi/k$, the group velocity ($\partial\omega/\partial k$) is positive (i.e. eastward) and therefore in the direction opposite to the phase velocity. The maximum group velocity is $c_g = \frac{1}{8}c/(2n+1)$ when $k = [3(2n+1)/L_E^2]^{1/2}$. Thus only short waves can carry information eastwards and then at only one eighth of the speed at which long waves can carry information westwards.

5.8 Baroclinic motions in low latitudes

The equations for small amplitude perturbations to an incompressible stratified fluid at rest are

$$\frac{\partial u}{\partial t} - fv = -\frac{\partial P}{\partial x}, \quad (5.73)$$

$$\frac{\partial v}{\partial t} + fu = -\frac{\partial P}{\partial y}, \quad (5.74)$$

$$\frac{\partial \sigma}{\partial t} + N^2\omega = 0, \quad (5.75)$$

$$\frac{\partial P}{\partial z} - \sigma = 0, \quad (5.76)$$

$$\frac{\partial u}{\partial x} + \frac{\partial v}{\partial y} + \frac{\partial w}{\partial z} = 0, \quad (5.77)$$

where $P = p/\bar{\rho}$. Elimination of w and σ from (5.75) - (5.77) gives

$$\frac{\partial u}{\partial x} + \frac{\partial v}{\partial y} - \frac{\partial}{\partial t} \left[\frac{\partial}{\partial z} \left(\frac{1}{N^2} \frac{\partial P}{\partial z} \right) \right] = 0. \quad (5.78)$$

If we choose P to satisfy the equation (5.79)

$$\frac{\partial}{\partial z} \left(\frac{1}{N^2} \frac{\partial P}{\partial z} \right) + \frac{P}{c^2} = 0 \quad (5.79)$$

then (5.32) becomes

$$\frac{\partial P}{\partial t} + c^2 \left(\frac{\partial u}{\partial x} + \frac{\partial v}{\partial y} \right) = 0, \quad (5.80)$$

whereupon Eqs. (5.73), (5.74) and (5.80) have exactly the same form as the shallow-water equations (5.1) - (5.3) if we identify $c^2\eta$ in the latter with P in the former. Equation (5.79) with appropriate boundary conditions leads to an eigenvalue problem for the vertical structure of wave perturbations and the corresponding eigenvalue c . Consider the case of an isothermal atmosphere with $N^2 = \text{constant}$. Then differentiating (5.79) with respect to z and t and using (5.75) and (5.76) to eliminate P in preference to w gives

$$\frac{\partial^2 w}{\partial z^2} + \frac{N^2}{c^2} w = 0. \quad (5.81)$$

For a liquid layer bounded by rigid horizontal boundaries at $z = 0$ and $z = H$, where $w = 0$, Eq. (5.81) has the solution

$$w = \hat{w}_n(x, y, t) \sin\left(\frac{n\pi z}{H}\right), \quad (n = 1, 2, 3, \dots), \quad (5.82)$$

and the corresponding eigenvalues are

$$c = c_n = \frac{NH}{n\pi}, \quad (n = 1, 2, 3, \dots)$$

As usual, the gravest mode (the one with the largest phase speed, the case $n = 1$) has a single vertical velocity maximum in the middle of the layer, $z = \frac{1}{2}H$. Taking typical values for $N (= 10^{-2} \text{ s}^{-1})$ and H (the tropical tropopause = 16 km), the phase speed of the gravest mode $c_1 = 51 \text{ m s}^{-1}$.

It is easily verified that (5.81) holds even if N is a function of z , but the eigenvalue problem will then be more difficult to solve.

5.9 Vertically-propagating wave motions

In an unbounded vertical domain and when N is a constant, Eq. (5.81) has solutions proportional to $\exp(\pm imz)$, where $m^2 = N^2/c^2$. Therefore, the system of equations (5.73) - (5.77) have solutions in which, for example,

$$v = D_n \left(\frac{y}{L_e}\right) \exp[i(kx + mz - \omega t)], \quad (5.83)$$

where

$$c = N/|m|. \quad (5.84)$$

Note that c is a property of the mode in question and is equal to the phase speed *only* in special cases such as the Kelvin wave. For an isothermal compressible atmosphere, Eq. (5.81) is a little more complicated, but is still given by (5.84) to a good approximation provided that $1/(4m^2 H_s^2) \ll 1$, where H_s is the scale height. Even for vertical wavelength of 20 km, this number is only about 0.03, so that the incompressible approximation is reasonable.

Now consider the dispersion relation $\omega = \omega(\mathbf{k})$ for the various types of waves with vector wavenumber $\mathbf{k} = (k, m)$. It is convenient to scale the wavenumber components by writing $k = (\beta/\omega)k_*$ and $m = (\beta N/\omega^2)m_*$. Then, the dispersion relation for the Kelvin wave, $\omega = kc$ becomes

$$m_* = k_* . \quad (5.85)$$

For the mixed Rossby- gravity wave ($n = 0$), $\omega m/N - k - \beta/\omega = 0$ from (5.46), which becomes,

$$m_* = k_* + 1 . \quad (5.86)$$

The remaining waves satisfy (5.36)

$$m_*^2 - (2n + 1)m_* = k_*^2 + k_* ,$$

or

$$m_* = n + \frac{1}{2} + \left[\left(k_* + \frac{1}{2} \right)^2 + n(n + 1) \right]^{1/2} . \quad (5.87)$$

It can be shown that modes corresponding with the positive root in (5.87) are gravity waves while those corresponding with the negative root are planetary waves. The full set of dispersion curves is shown in Fig. 5.10. The gravity wave curves are the hyperbolae in the upper part of the diagram. The planetary wave curves are hyperbolae also and are shown on the expanded plot in the inset. The corresponding curves in the \mathbf{k} -plane are the curves of constant frequency. The group velocity $\mathbf{c}_g = \nabla_k \omega$ is at right angles to these curves and in the direction of increasing ω . The corresponding directions are shown in Fig. 5.10.

We carry out the calculations for the Kelvin wave and mixed Rossby-gravity waves.

5.9.1 Kelvin wave

$$\omega = \frac{Nk}{|m|} = \frac{N}{m}k \operatorname{sgn}(m)$$

Then

$$c_{g1} = \frac{\partial \omega}{\partial k} = \frac{N}{|m|} = c_{3p} , \text{ say } , \text{ and } c_{g3} = \frac{\partial \omega}{\partial m} = -\frac{N}{m^2}k \operatorname{sgn}(m) ,$$

whereupon

$$c_g = \left(\frac{\partial \omega}{\partial k}, \frac{\partial \omega}{\partial m} \right) = \frac{N}{|m|} \left(1, -\frac{k}{m} \right) .$$

Note that $c_{g3} > 0$ if $m < 0$, i.e. the Kelvin wave solution that propagates energy vertically upwards has phase lines that slope upward in the eastward direction (5.11). Figure 5.11 shows the structure of this mode.

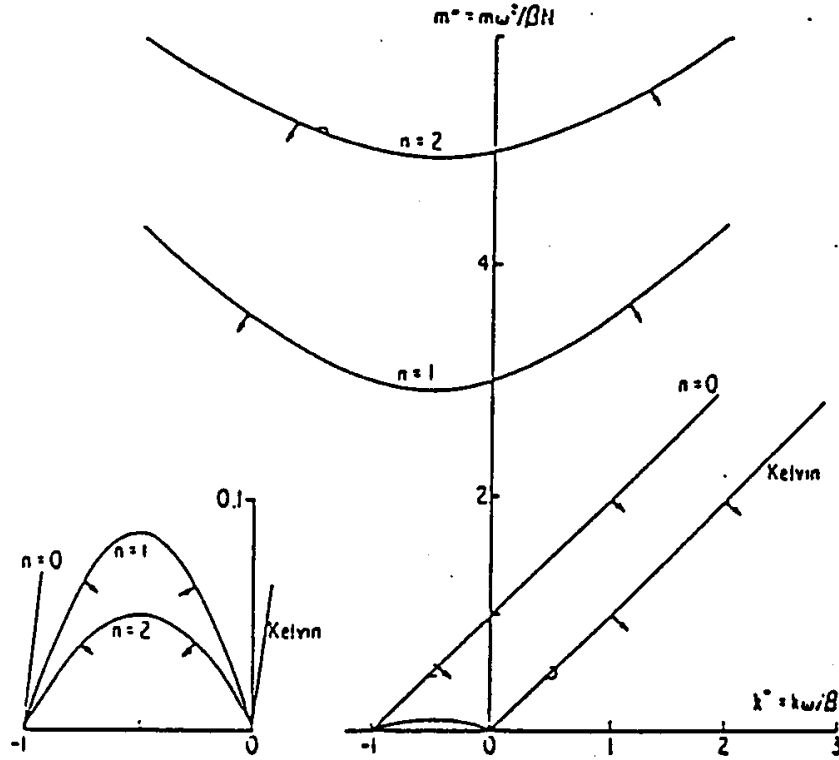


Figure 5.10: Dispersion curves for vertically-propagating equatorially-trapped waves. m is the vertical wavenumber and λ the eastward wavenumber. The curves collapse into a single set when scaled with the frequency ω , buoyancy frequency N , and beta as indicated. The direction of the group velocity, being the gradient of frequency in wavenumber space, is as indicated. The curves for m negative are obtained by reflection in the k^* axis and have an upward-directed group velocity. The inset at the left is a blowup of the region near the origin to show the planetary waves $n = 1, 2$. The upper $n = 1, 2$ curves are the corresponding gravity waves. The circles represent observed waves.

5.9.2 Mixed Rossby-gravity wave

ω satisfies

$$\frac{\omega m}{N} \operatorname{sgn}(m) - k - \frac{\beta}{\omega} = 0, \tag{5.88}$$

whereupon

$$\frac{\partial \omega}{\partial k} = 1 / \left(\frac{|m|}{N} + \frac{\beta}{\omega^2} \right),$$

i.e.

$$\underline{c}_g = \left(1, -\frac{\omega}{N} \operatorname{sgn}(m) \right) / \left(\frac{|m|}{N} + \frac{\beta}{\omega^2} \right). \quad (5.89)$$

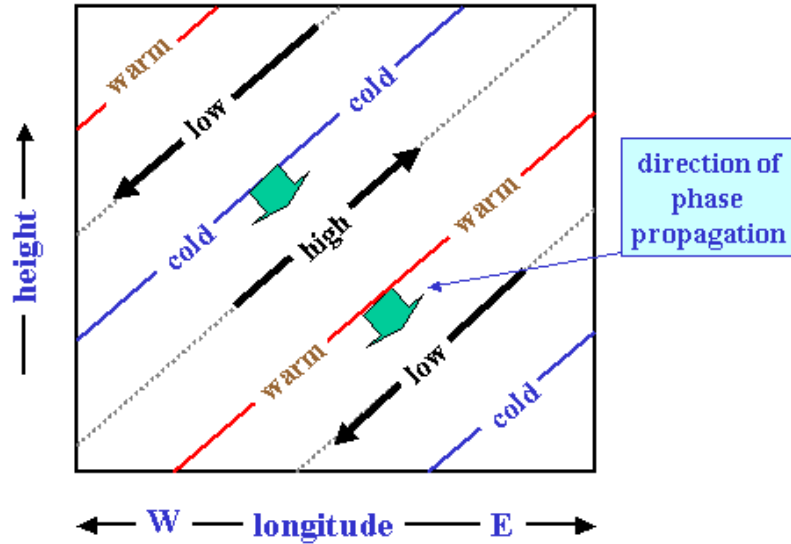


Figure 5.11: Longitudinal-height section along the equator showing pressure, temperature and perturbation wind oscillations in the Kelvin wave. Thick arrows indicate direction of phase propagation. (After Wallace, 1973).

Now (5.88) gives

$$\omega = \frac{1}{2}k \frac{N}{|m|} \pm \left(\frac{1}{4}k^2 \frac{N^2}{|m|^2} + \beta \frac{N}{|m|} \right)^{1/2},$$

from which it follows that the mixed Rossby-gravity wave, i.e. the solution for the negative square root, has $\omega < 0$. From (5.89) we see that this has an upward-directed group velocity if $m > 0$. Thus the phase lines of the mixed Rossby-gravity wave tilt westward with height (Fig. 5.12). Figure 5.12 shows the structure of this mode also. Note that poleward-moving air is correlated with positive temperature perturbations so that the eddy heat flux $v'T'$ averaged over a wave is positive. The mixed Rossby-gravity wave removes heat from the equatorial region.

Both Kelvin wave and mixed Rossby-gravity wave modes have been identified in observational data from the equatorial stratosphere. The observed Kelvin waves have periods in the range 12-20 days and appear to be primarily of zonal wavenumber 1. The corresponding observed phase speeds of these waves relative to the ground are on the order of 30 m s^{-1} . In applying our theoretical formulas for the meridional and vertical scales, however, we must use the Doppler-shifted phase speed $c_p - U$, where

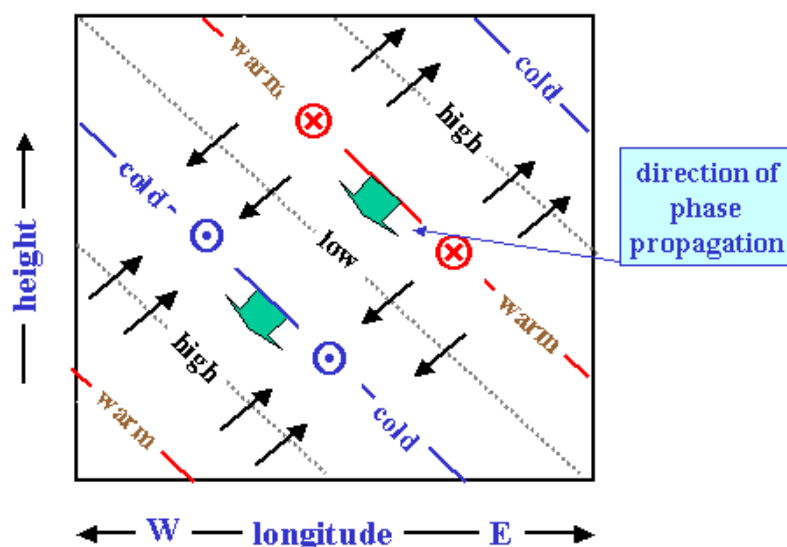



Figure 5.12: Longitudinal-height section at a latitude north of the equator showing pressure, temperature and perturbation wind oscillations in the mixed Rossby-gravity wave. Meridional wind components are indicated by arrows pointed into the page (northward) and out of the page (southward). Thick arrows indicate direction of phase propagation.

U is the mean zonal wind speed. Assuming $u = -10 \text{ m s}^{-1}$, $c_p - U = 40 \text{ m s}^{-1}$, whereupon $L_E = \sqrt{[(c_p - U)/\beta]} \approx 1300 \text{ km}$. This corroborates with observational evidence that the Kelvin waves have significant amplitude only within about 20° latitude of the equator. Knowledge of the observed phase speed also allows one to calculate the theoretical vertical wavelength of the Kelvin wave. Assuming that $N = 2 \times 10^{-2} \text{ s}^{-1}$ (a stratospheric value) we find that

$$\frac{2\pi}{|m|} = 2\pi \frac{(c_p - U)}{N} \approx 12 \text{ km},$$

which agrees with the vertical wavelength deduced from observations. (Note that for the Kelvin wave, $c_p = c$).

 Figure (5.13) shows an example of zonal wind oscillations associated with the passage of Kelvin waves at a station near the equator. During the observational period shown in the westerly phase of the so-called quasi-biennial oscillation is descending so that at each level there is a general increase of the mean zonal wind with time. Superposed on this trend is a large fluctuating component with a period between speed maxima of about 12 days and a vertical wavelength (computed from the tilt of the oscillations with height) of about 10-12 km. Observations of the temperature field for the same period reveal that the temperature oscillation leads the zonal wind oscillation by one quarter of a cycle (that is, the maximum temperature occurs one-quarter of a period prior to maximum westerlies), which is just the phase relationship

required for Kelvin waves (see Fig. 5.11). Furthermore, additional observations from other stations indicate that these oscillations do propagate eastward at about 30 m s^{-1} . Therefore there can be little doubt that the observed oscillations are Kelvin waves.

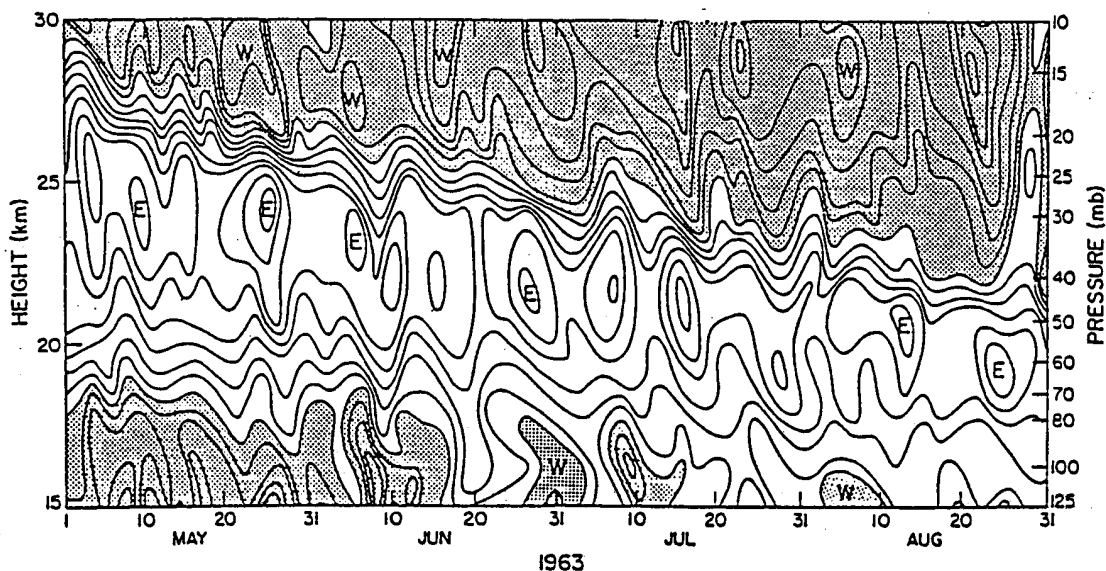


Figure 5.13: Time-height section of zonal wind at Kwajalein (9° latitude). Isotachs at intervals of m s^{-1} . Westerlies are shaded. (After Wallace and Kousky, 1968).

The existence of the mixed Rossby-gravity mode has been confirmed also in observational data from the equatorial Pacific. This mode is most easily identified in the meridional wind component, since v is a maximum for it at the equator. The observed waves of this mode have periods in the range of 4-5 days and propagate westward at about 20 m s^{-1} . The horizontal wavelength appears to be about 10,000 km, corresponding to zonal wavenumber-4. The observed vertical wavelength is about 6 km, which agrees with the theoretically derived wavelength within the uncertainties of the observations. These waves appear to have significant amplitudes only within about 20° latitude of the equator also, which is consistent with the e-folding width $\sqrt{2L_E} = 2300 \text{ km}$. Note that in this case, $c = c_p$, but using (5.88) and (5.84), for the mixed Rossby-gravity wave mode. At present it appears that both the Kelvin waves and the mixed Rossby-gravity waves are excited by oscillations in the large-scale convective heating pattern in the equatorial troposphere. Although these waves do not contain much energy compared with typical tropospheric disturbances, they are the predominant disturbances of the equatorial stratosphere. Through their vertical energy and momentum transport they play a crucial role in the general circulation of the stratosphere.

Exercises

5.1 The linearized momentum equations for a Boussinesq fluid on an equatorial β -plane are (see Gill, 1982, p449):

$$\frac{\partial u}{\partial t} + 2\Omega w - \beta y v = -\frac{1}{\rho_o} \frac{\partial p}{\partial x},$$

$$\frac{\partial v}{\partial t} + \beta y u = -\frac{1}{\rho_o} \frac{\partial p}{\partial y}$$

$$\frac{\partial w}{\partial t} - 2\Omega u = -\frac{1}{\rho_o} \frac{\partial p}{\partial z} + \sigma,$$

Consider the following scaling: horizontal length scale $L = (c/\beta)^{1/2}$, time scale $T = (\beta c)^{-1/2}$, horizontal velocity scale U , pressure scale $P = \rho_o c U$, vertical length scale $H = c/N$, vertical velocity scale $w = (\omega/N)U$, where ω is a frequency. Show that the Coriolis acceleration associated with the horizontal component of rotation $2\Omega w$ can be neglected if $2\Omega < N$. Show that in this case the vorticity equation reduces to

$$\frac{\partial \zeta}{\partial t} + f \left(\frac{\partial u}{\partial x} + \frac{\partial v}{\partial y} \right) + \beta v = 0,$$

where $f = \beta y$. Give an interpretation of this equation in the case of steady motions. Note that the foregoing scaling is suggested by a linearized wave analysis of the approximated equation set (see Gill *op. cit.*).

5.2 The dispersion relation for the mixed Rossby-gravity wave is

$$\omega = \frac{1}{2} k c - \left[\frac{1}{4} k^2 c^2 + c \beta \right]^{1/2}.$$

Show that $\omega \rightarrow -\beta/k$ as $k \rightarrow 0$ and $\omega \rightarrow \frac{1}{2} k c$ as $k \rightarrow \infty$.

Show also that although the phase velocity is westward for all wavenumbers, the group velocity is eastward.

Chapter 6

STEADY AND TRANSIENT FORCED WAVES

In this chapter we consider a range of specific situations in which waves are excited in the equatorial wave guide. We begin with an analysis of steadily forced waves with application to understanding the structure of the Walker circulation and go on to study transient waves generated by tropical convection, or by middle latitude weather systems.

6.1 Response to steady forcing

Consider a homogeneous ocean layer of mean depth H forced by a surface wind stress $\mathbf{X} = (X, Y)$ per unit area. We assume that through the process of turbulent mixing in the vertical, this wind stress is distributed uniformly with depth as body force $\mathbf{X}/(\rho H)$ per unit mass. Suppose that there is also a drag per unit mass acting on the water, modelled by the linear friction law $-\mathbf{r}\mathbf{u}$ per unit mass. Then the equations analogous to (3.21) and (3.22) are

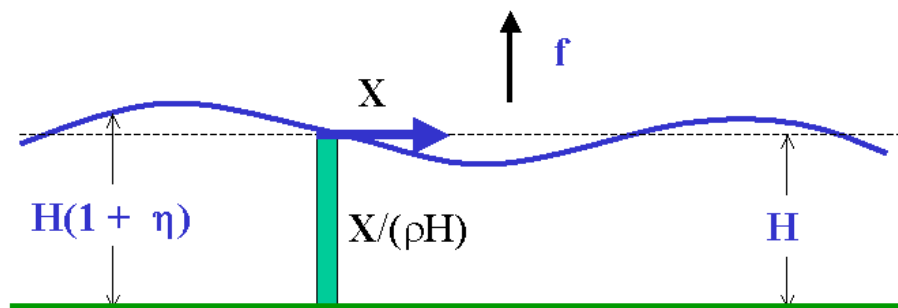


Figure 6.1: Shallow-water model with a wind stress distributed as a uniform body force over depth. (From Gill, 1982).

$$-\beta yv = -gH \frac{\partial \eta}{\partial x} + X/(\rho H) - ru, \quad (6.1)$$

$$\beta yu = -gH \frac{\partial \eta}{\partial y} + Y/(\rho H) - rv. \quad (6.2)$$

The continuity equation analogous to (3.23) takes the form

$$c^2 \frac{\partial u}{\partial x} + \frac{\partial v}{\partial y} = -gE/\rho - c^2 r \eta, \quad (6.3)$$

where E may be interpreted as an evaporation rate (i.e. rate of mass removal) and $r\eta$ with $r > 0$ represents a linear damping of the free surface displacement. In the atmospheric situation, a positive/negative evaporation rate is equivalent to the effect of convective heating/cooling (see Chapter 5) and the damping term represents Newtonian cooling due, for example, to infra-red radiation space. Although formally obtained for a shallow homogeneous layer, we have shown that these equations apply for each normal mode, but with a value of appropriate to that mode. Also, the magnitude of the forcing is then determined by expanding the forcing function in normal modes.

As before, Eqs. (6.1-6.3) can be written as a single equation for v , i.e.

$$\begin{aligned} & \frac{r}{c^2} (r^2 + f^2) v - r \left(\frac{\partial^2 v}{\partial x^2} + \frac{\partial^2 v}{\partial y^2} \right) - \beta \frac{\partial v}{\partial x} = \\ & \frac{1}{\rho H} \left\{ \frac{r}{c^2} (rY - fX) + r \frac{\partial E}{\partial y} - \frac{\partial}{\partial x} \left(\frac{\partial Y}{\partial x} - \frac{\partial X}{\partial x} + fE \right) \right\}. \end{aligned} \quad (6.4)$$

Note that leading terms involve only x derivatives, i.e. in the case of small friction ($r \rightarrow 0$), this equation reduces to

$$\beta \frac{\partial v}{\partial x} = \frac{1}{\rho H} \frac{\partial}{\partial x} \left(\frac{\partial Y}{\partial x} - \frac{\partial X}{\partial x} + fE \right), \quad (6.5)$$

which may be integrated with respect to x to give

$$\beta v = \frac{1}{\rho H} \left(\frac{\partial Y}{\partial x} - \frac{\partial X}{\partial x} + fE \right). \quad (6.6)$$

When $E = 0$, this is Sverdrup's formula (see DM, Ch. 6).

6.1.1 Zonally-independent flow

In this case, $(\partial/\partial x = 0)$ and Eq. 6.4 reduces to

$$\frac{(r^2 + f^2)}{c^2} v - \frac{\partial^2 v}{\partial y^2} = \frac{1}{\rho H} \left\{ \frac{(rY - fX)}{c^2} + \frac{\partial E}{\partial y} \right\}, \quad (6.7)$$

where a factor r has been cancelled. This formula is valid on an f -plane, or on an equatorial β -plane, where $f = \beta y$. In the latter case, solutions are possible in terms of parabolic cylinder functions of order $\frac{1}{2}$ (see Gill 1982, p467).

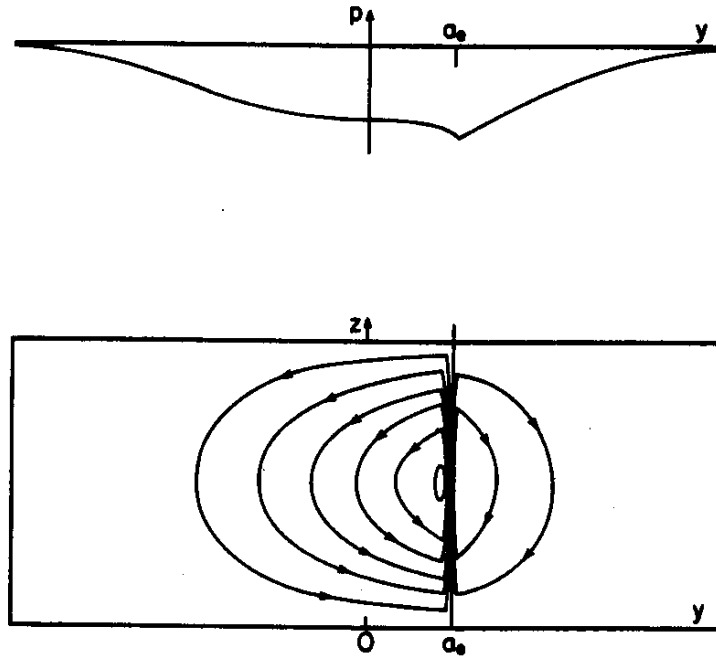


Figure 6.2: The linear solution due to a line source of heat (or evaporation) located at $y = L_E$, i.e., one Rossby radius from the equator. The upper panel shows the pressure distribution with a trough at the heating latitude. Inflow to the trough comes mainly from the equatorial side. This is depicted in the lower panel, where the solution is interpreted as having a sinusoidal vertical structure associated with a single vertical mode. The picture then has the character of the meridional circulation generated by heating along a particular latitude, as occurs in the ITCZ (From Gill 1982).

The upper panel of Fig 6.2 shows the variation of surface elevation (or pressure perturbation p') for evaporation (or heating) concentrated along the line $y = L_E$, the equatorial Rossby radius. The variation of f is manifested in a slower fall off in pressure on the equatorial side of the evaporative sink. When the solutions are applied to baroclinic motions in an incompressible atmosphere of constant buoyancy frequency N with a “rigid lid” at some height, the baroclinic modes have a sinusoidal vertical structure (see section 5.8). The “gravest” mode (i.e. the one with the largest vertical scale) is a sine of height with half-wavelength spanning the depth. If diabatic heating is applied with this distribution in the vertical, only the gravest mode is excited and the equations are the shallow-water equations with heating replacing the evaporation term. The lower panel of Fig. 6.2 shows the meridional circulation

produced by such heating concentrated **on the line** and is obtained by attaching the appropriate vertical structure to the solutions of (6.7). This is a type of Hadley circulation that is generated by a line source of heating such as occurs along the ITCZ. Rising air is found only in the heating zone. Most air is drawn in from the equatorial side, so that the most pronounced circulation is on this side. The pressure curve shows how the surface pressure varies **with such solution**.

6.1.2 Zonally-dependent flow

Gill (1982, p469) explains how to construct a solution to Eq. 6.4 for the more general case of a localized heating covering a restricted range of longitudes and similar to that which obtains in the atmosphere in July. If the equatorial Rossby radius L_R is taken to be about 10° of latitude, the solution shown in Fig. 6.3 with $L = 2L_R$ corresponds to maximum heating at about 10°N and covering 40° of longitude. According to Newell et al. (1974; see plate 9.1), the region of large heating in the atmosphere is concentrated as it is in Fig. 6.3, but with maximum at about 15°N and with largest values between 90° and 140°E longitude.

In the region of heating, Fig. 6.3a shows vertical motion and mainly northward velocities, although there is some distortion on the west side because of friction. The interpretation is that ascent associated with the heating causes vortex stretching and thereby to the generation of cyclonic vorticity. Thus the fluid particles tend to move polewards in order to keep their relative vorticity small. The only wave that can propagate eastwards from the forcing region is a Kelvin wave, so that the region $x > L$ (corresponding to the Pacific Ocean if the model is applied to the effect of forcing over Indonesian longitudes) shows motion with characteristic features of the Kelvin wave, namely, flow parallel to the equator and symmetric about the equator. The winds are easterly toward the heat source and decay eastward at the rate r/c per unit distance. Physically, the decay process represented by r (Geisler, 1981) appears to be "cumulus friction" due to momentum transfer between levels through cumulus activity. Long planetary waves can propagate westward from the forcing region, but they decay faster than the Kelvin waves and thus cover a smaller area. They include meridional motion, so the equatorward return of the air moving poleward in the heating region is found to the west. The result is a cyclonic center on the west flank of the heating region. (Comparisons can be made with the observed 850-mb flow shown in Fig. 1.11.) Solutions with similar properties were found by Webster (1972), who obtained numerical solutions with a two-layer model for perturbations on a zonal flow, and Matsuno (1966), who obtained solutions for forcing periodic in x . Solutions of the shallow-water equations with friction on a sphere, as obtained by Margules (1893), show similar characteristics also.

The upper panels of Fig. 6.4 show the zonally averaged flow, exhibiting a strong Hadley cell with rising motion in the latitude of maximum heating. Equatorial motion is associated with easterlies and poleward motion with westerlies. This is due to conservation of angular momentum and the fact that, in a linear formulation,

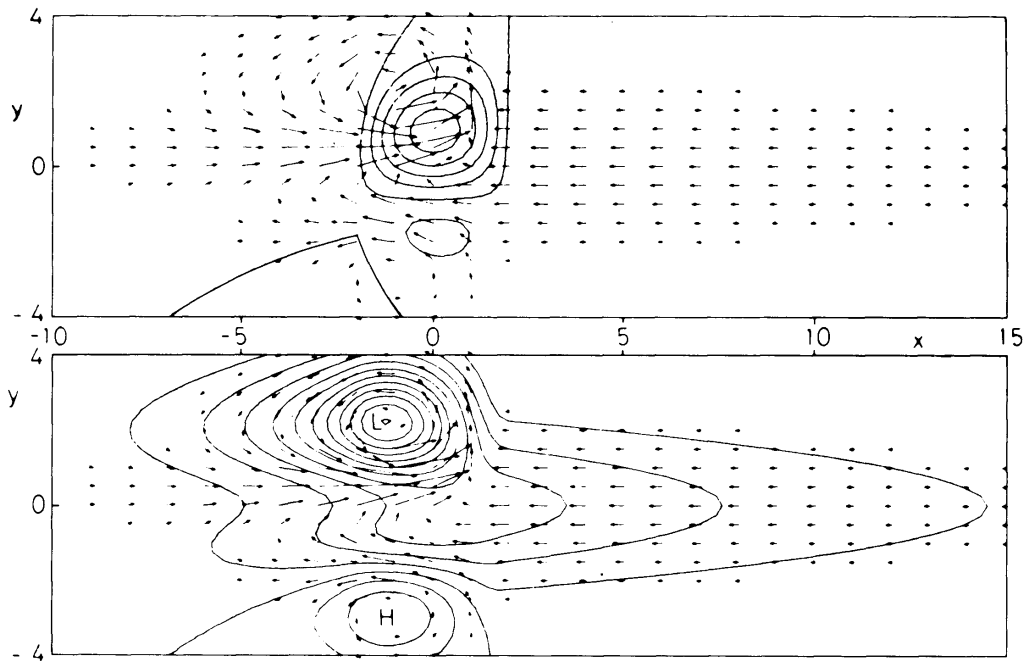


Figure 6.3: The solution of the forced shallow-water equations for heating (or evaporation) that is confined to the range of longitudes $|x| < 2L_E$. The arrows give the horizontal velocity field and the solid contours in the upper panel give the vertical velocity, which has a distribution close to the heating function. The motion is upward within the contours north of the equator with a maximum near $x = 0$, $y = L_E$. The contours in the lower panel are pressure contours, and the axes are labelled in units of L_E . (From Gill 1980).

the fluid "remembers" only the angular momentum from the latitude where it has just been. Thus the zonal velocity changes sign on crossing the equator. The lower panel of Fig. 6.4 shows the meridionally averaged circulation, which is due only to the part of the forcing that is symmetric about the equator. Rising motion is found over the longitudes of the heating region, and sinking elsewhere. The circulation corresponds with the Walker circulation discussed in Chapter 1.

6.2 Response to transient forcing

The low-latitude atmospheric response to transient forcing can be studied also using the equatorial β -plane model [described in this chapter](#). Silva Dias *et al.* (1983) used such a model to investigate the atmospheric response to localized transient heat sources, which crudely simulate convective bursts in the tropical region. The equations of motion are similar to Eqs. (5.73), (5.74) and (5.78), but include forcing terms on the right-hand sides similar to Eqs. (6.1) - (6.3). The reader is referred to

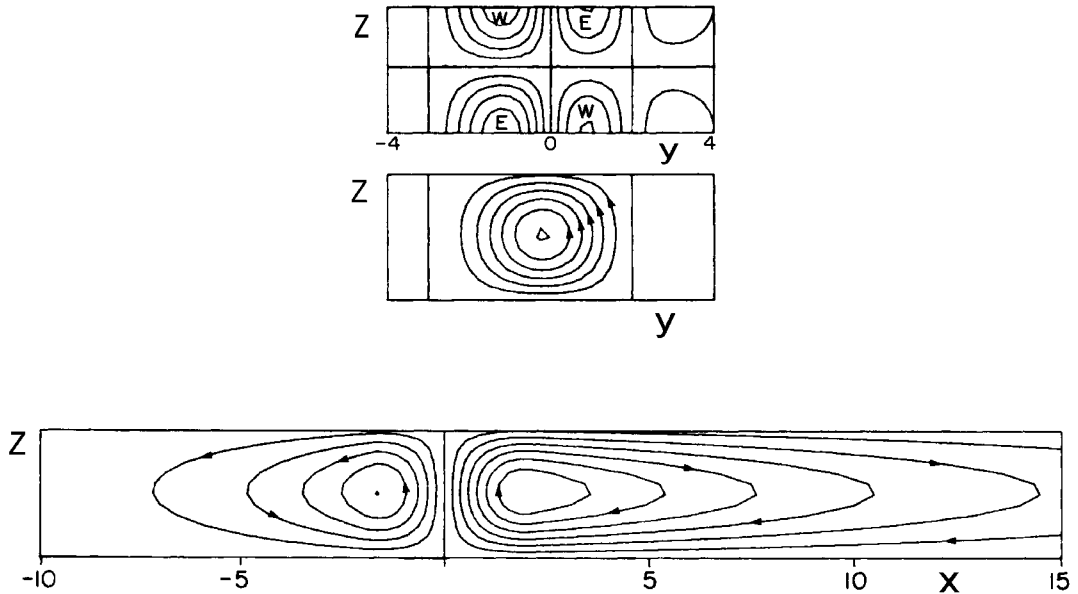


Figure 6.4: The mean zonal flow (uppermost panel), mean meridional circulation (middle panel) and corresponding with the solution in Fig. 6.3, when the response is interpreted as a baroclinic response to heating with sinusoidal variation in the vertical. The lower panel shows the meridionally-averaged zonal flow (Walker circulation). (From Gill 1980).

the original paper for details of the formulation, which uses $\ln p$ as vertical coordinate rather than the actual height as used here.

Silva Dias *et al.* (1983) study the case where a heat source is added to Eq. (5.78) with the form:

$$\frac{1}{\pi a^2} \exp \left[- \left(\frac{x}{a} \right)^2 - \left(\frac{y - y_0}{a} \right)^2 \right] \chi(t). \quad (6.8)$$

This heat source is centred at a distance y_0 from the equator and has e-folding radius a . The time dependence $\chi(t)$ is given by

$$\frac{1}{2} \alpha^3 t^2 e^{-\alpha t}, \quad (6.9)$$

where α is a nondimensional parameter that characterizes the rapidity of the forcing (see Fig. 6.5). The forcing is a maximum when $t = 2/\alpha$, which corresponds to about 4 h for $\alpha = 4$ and about 12 h for $\alpha = 4/3$, using the time scale for the first internal mode in the calculations. The total heating is independent of α since

$$\int_0^\infty \frac{1}{2} \alpha^3 t^2 e^{-\alpha t} dt = 1$$

and it is independent of y_0 since

$$\int_{-\infty}^{\infty} \int_{-\infty}^{\infty} \frac{1}{\pi a^2} \exp \left[\frac{x^2}{a^2} + \frac{(y - y_0)^2}{a^2} \right] dx dy = 1$$

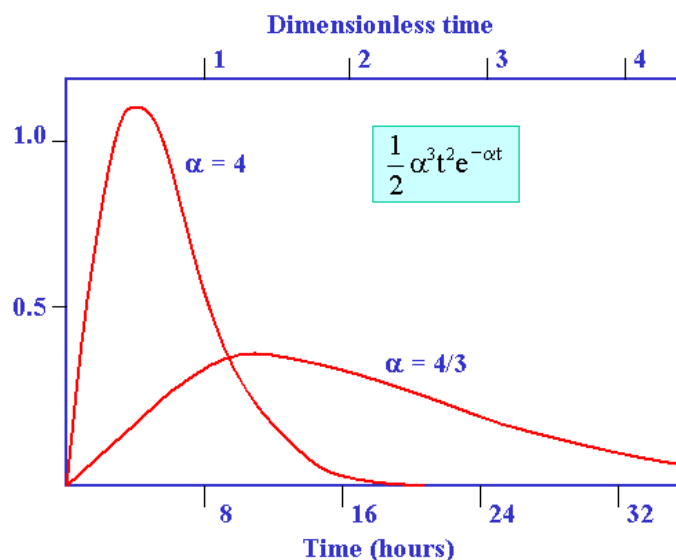


Figure 6.5: Time dependence of the momentum and heat source/sink terms for two parameter values of α . (From Silva Dias *et al.* 1983).

Silva Dias *et al.* (1983) used transform techniques to solve the equations. Here we summarize some of the key results. Figure 6.6 shows the wind and geopotential fields for the case $\alpha = 4/3$, $a = 0.5$ and $y_0 = -0.8$ at $t = 2, 4, 6$ and 8 nondimensional units. Also shown is the contribution to the total field from the Kelvin waves (panels b), mixed Rossby-gravity waves (panels c) and Rossby waves (panels d). The wind and geopotential fields are equally scaled. For the internal mode corresponding to $c = 51 \text{ m s}^{-1}$ the dimensional time scale [T] is 8 h and the spatial scale [L] is ~ 1500 km. Using this scaling, the e-folding radius of the thermal forcing is then 750 km and the latitude of the forcing is 11°S . As can be seen in Fig. 5.7, when $a = 4/3$, the forcing is a maximum at $t = 1.5$ nondimensional units and becomes negligible after $t = 6$ nondimensional units which correspond to $t = 12$ h and $t = 48$ h respectively.

The total flow fields in panels (a) of Fig. 6.6 show many interesting features. At $t = 16$ h (left column) the high-pressure centre that developed in response to the forcing is displaced slightly south of the maximum forcing. Also noticeable is the asymmetry of the response. There is a strong cross-equatorial flow with the maximum wind speed in the neighbourhood of the equator. The flow pattern becomes more geostrophic as the latitude increases in agreement with the larger Coriolis parameter. At $t = 32$ h the forcing has decreased to 25% of its maximum intensity and the flow

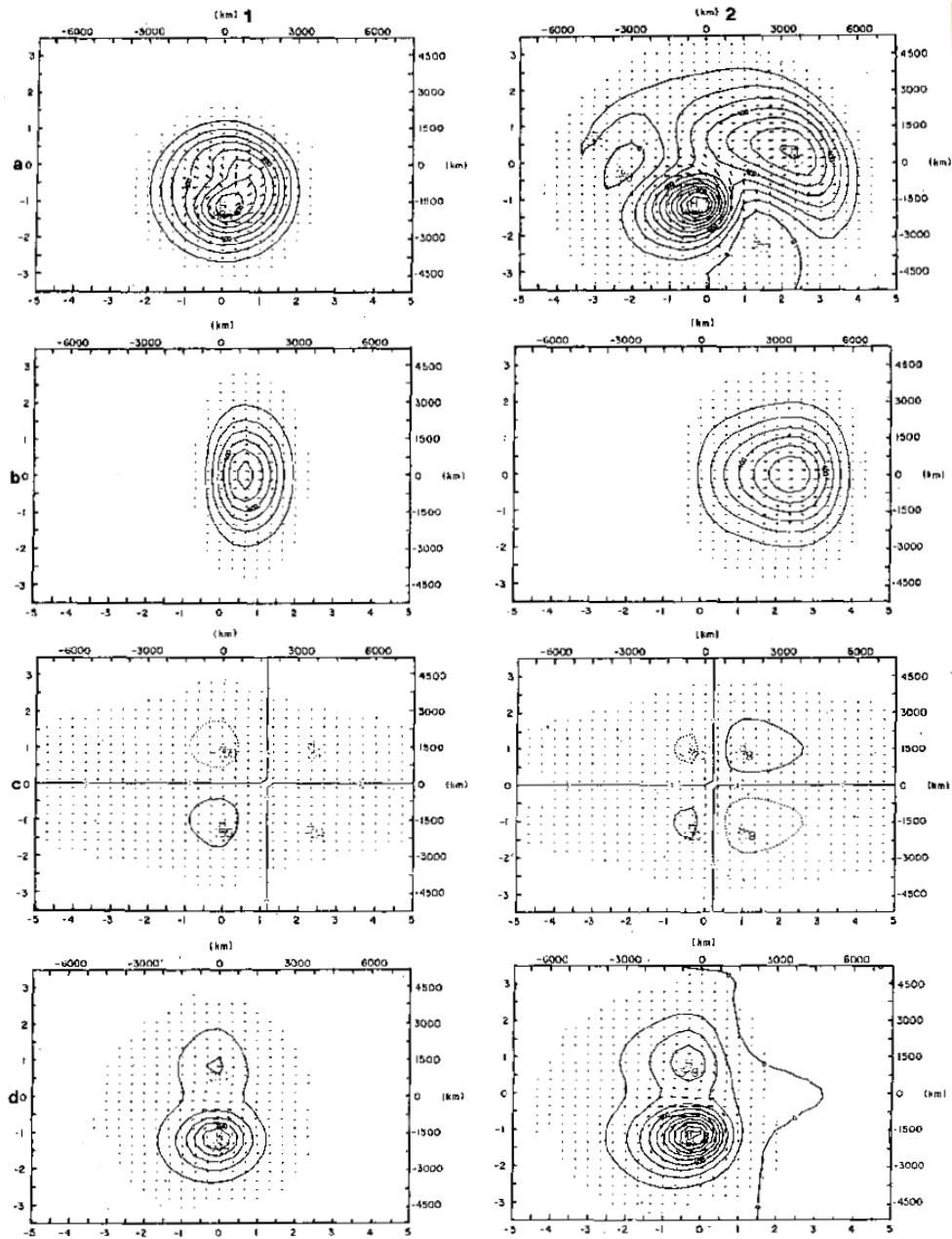


Figure 6.6: Horizontal structure of the wind and geopotential fields at $t = 16, 32, 48$ and 64 h (columns 1 and 2, here and columns 1 and 2 overleaf, respectively) for the case of a heat source centred at $y = -1200$ km (11°S) with time constant $\alpha^{-1} = 6$ h and horizontal scale $a = 750$ km. The total field is shown in (a) and the contributions to this from the Kelvin, mixed Rossby-gravity and Rossby waves are shown in (b), (c) and (d), respectively. (From Silva Dias *et al.* 1983).

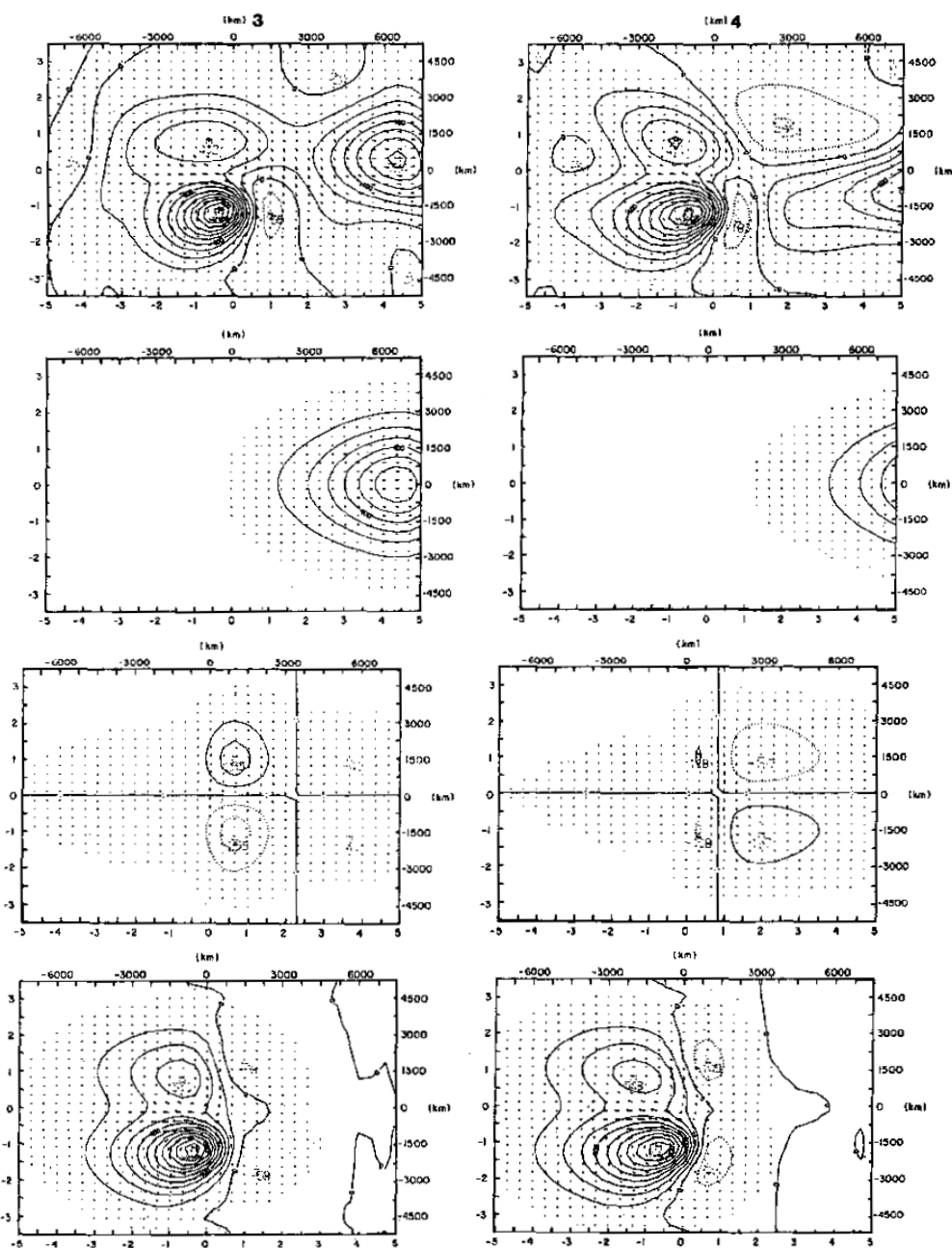


Figure 6.6 (continued).

pattern is becoming more geostrophic although the cross-isobaric flow is still intense near the equator. At $t = 32$ h there are several features that deserve attention:

- (i) the southerly and southeasterly flow on the northeast side of the anticyclone have become more intense,
- (ii) the centre of the anticyclonic circulation is now displaced west of the maximum

forcing,

- (iii) a trough is beginning to develop east of the anticyclonic circulation,
- (iv) westerlies have developed along the equator with maximum wind speed at $x = 3000$ km and maximum pressure perturbation displaced slightly towards the Northern Hemisphere and
- (v) the flow across the equator now has an anticyclonic curvature in the Northern Hemisphere.

At $t = 48$ h and $t = 64$ h the above characteristics tend to become more evident except that the cross-equatorial flow north of the main high pressure has decreased and a new region of cross equatorial flow with a northerly component has developed between $x = 1500$ km and $x = 4500$ km. By $t = 48$ h the forcing has decreased to 4% of its maximum value and the whole flow pattern is slowly dispersing. The main anticyclone is becoming elongated toward the west and a sharp east-west geopotential gradient is forming between the low centred near $x = 1500$ km and the main high. Accordingly, strong winds are also observed in this region. Also noticeable is the rapid eastward drift of the circulation pattern discussed in item (iv). A comparison of panels (a) and (b) in Fig. 6.6 shows that this circulation pattern is associated with the Kelvin wave contribution. Thus, the cross-isobaric flow observed on the northeast quadrant of Fig. 6.6a at $t = 16$ h moves eastward and propagates as a nondispersive wave group.

At first it may appear that the Kelvin waves in Fig. 6.6 are exhibiting a dispersive behaviour since the initially narrow disturbance at $t = 16$ h becomes elongated at later times. ~~This, however,~~ is due to the continual generation of Kelvin waves while the forcing is active. After $t = 48$ h when the forcing becomes negligible the Kelvin wave group propagates eastward without changing shape.

The contribution from the mixed Rossby-gravity waves shown in Fig. 6.6c is small, but is responsible for certain features of the total flow field. The mixed Rossby-gravity waves have a westward phase speed, but propagate energy eastwards. This feature can be seen in panels (c) of Fig. 6.6 as a successive eastward reinforcement of the geopotential and wind maxima. Comparing panels (a) and (c) in Fig. 6.6 at $t = 48$ h and $t = 64$ h shows that the northwesterly flow at the equator between $x = 1500$ km and $x = 3000$ km, and the lowering of the geopotential near $y = -1500$ km and $x = 1500$ km in the total solution, are associated with the mixed Rossby-gravity waves. The formation of this trough east of the main anticyclone is **also** caused partially by the eastward dispersion of short Rossby waves which can be seen by comparing Figs. 6.6a and 6.6d at $t = 64$ h. The formation of the low geopotential region at $x = 3000$ km and $y = 2000$ km, which is most evident at $t = 64$ h, is also primarily related to the mixed Rossby-gravity waves with some contribution from the shorter Rossby waves.

The panels in row (d) of Fig. 6.6 show the contribution to the total solution from the Rossby waves. Comparing Figs. 6.6d and 6.6a after $t = 32$ h shows that

the high geopotential configuration which appears in the Northern Hemisphere is a manifestation of the Rossby waves. This high pressure is generated in response to the heat source and migrates westward in the early stages of the transient solution. The pattern continues moving westward after the forcing becomes negligible. This evolution in time can be explained by the group velocity of Rossby waves, the sign of which can be deduced from the dispersion curve for these waves shown in Fig. 5.9. The zonal component of the group velocity is given by $-\partial\nu/\partial\mu$, which is the slope of the dispersion curve. Since the slope changes sign (except for $m = 0$), it is evident that the group velocity is eastward for short Rossby waves and westward for long Rossby waves. Thus, the westward elongation of the geopotential field in Fig. 6.6d is due to the dispersion of long Rossby waves and the intensification of the east-west gradient of the geopotential field east of the main high is a result of the eastward dispersion of short Rossby waves. The appearance of a stronger meridional flow at the longitude of maximum forcing is also predictable from the dispersive properties of Rossby waves since short Rossby waves are almost nondispersive and have more kinetic energy in the meridional than in the zonal component of the wind (Longuet-Higgins, 1964). The strong easterly flow along the equator and the predominately symmetric pattern that develops in panels (a) of Fig. 6.6 can be associated with the $m = 1$ Rossby mode. This particular mode is expected to have a large contribution to the solution because of its horizontal similarity with the forcing function.

Figure 6.7 shows the total wind and geopotential fields for the case when the heat source discussed previously is centred at the equator ($\alpha = 4/3$, $a = 0.5$ and $y_0 = 0$). As discussed in section 3 of Silva Dias *et al.* 1983), more of the energy of the final adjusted state is in the Kelvin modes than in the Rossby modes (see their Fig. 3d). This explains the large amplitude configuration that moves rapidly eastwards in Fig. 6.7. Since the forcing is symmetric about the equator, the initial outward spreading mass builds up two high-pressure centres, which are separated by an equatorial trough. During the initial development, ($t = 16$ h) it is evident that the mass tends to flow primarily along the equator with the streamlines curving toward the poles and away from the heat source. After the Kelvin waves propagate toward the east, the symmetric Rossby waves, which remain in the region of the heat source slowly, disperse.

The fields shown in Fig. 6.7 differ somewhat from the case where the equatorial heat source is stationary in time as discussed in section 5.8. The stationary case shows a zone of upper-level westerlies to the east of the forcing which is much more extensive than the zone of upper easterlies to the west of the forcing. Gill pointed out that the relative sizes of the east-west circulations is explained by the continual generation of the Kelvin waves by the stationary forcing, coupled with the large eastward group velocity of the Kelvin waves compared to the westward group velocity of the long Rossby waves. In the transient case shown in Fig. 6.6 the forcing becomes negligible after $t = 48$ h so that very little Kelvin wave energy is being generated. The previously generated Kelvin waves propagate to the east leaving only the upper-level easterly flow to the west of the forcing which is associated with the slower propagating

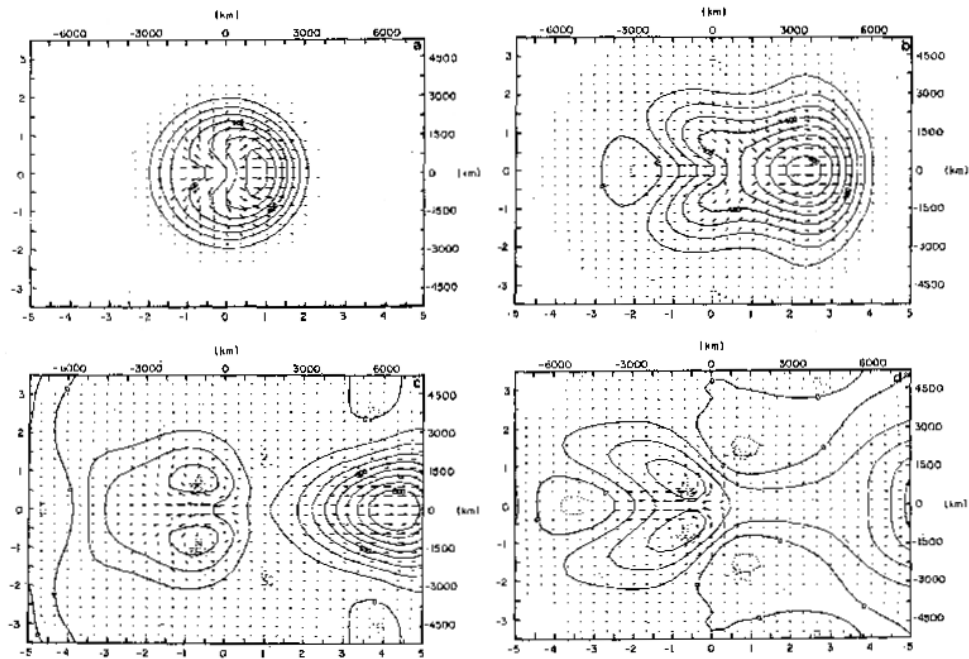


Figure 6.7: Horizontal structure of the wind and geopotential fields at $t = 16, 32, 48,$ and 64 h (Panels (a), (b), (c) and (d), respectively) for the case of a heat source centred at the equator with time constant $\alpha^{-1} = 6$ h and horizontal scale $a = 750$ km. (From Silva Dias *et al.* 1983).

Rossby waves.

The simulations presented in Figs. 6.6 and 6.7 show the response of the model to a transient heat source centred at two different latitudes. For comparison, Fig. 6.8 shows 200 mb FGGE maps at 0000 GMT for 6 February and for 9-12 February 1979 prepared by the European Centre for Medium Range Weather Forecasting (ECMWF). During a period of 2-3 days before 6 February, the Bolivian high was not well developed and the main synoptic feature in the equatorial region of South America was an upper-level cyclone off the northeast coast of Brazil. This is the type of upper low studied by Kousky and Gan (1981). After 6 February, the anticyclonic circulation began to organize and during the period 9-12 February (Figs. 6b-6e), the Bolivian high was again established. On 10 February there was a strong cross-equatorial flow at 50°W that turned and became a westerly flow at about 30°W . The most significant change occurred between 10 and 11 February with the sudden increase in speed of the southerly component between the centre of the Bolivian high and the upper trough off the northeast coast of Brazil. On 10 February the cross equatorial flow was well established and the anticyclonic circulation was developing in the Northern Hemisphere as a result of the change in sign of the Coriolis parameter. The trough off the northeast coast of Brazil was elongated and tilted northwest to southeast. On 12 February the Bolivian high was stretched in the east-west di-

rection with the flow more zonal in the vicinity of the equator and with the wind stronger in the eastern and northeastern sectors of the Bolivian high.

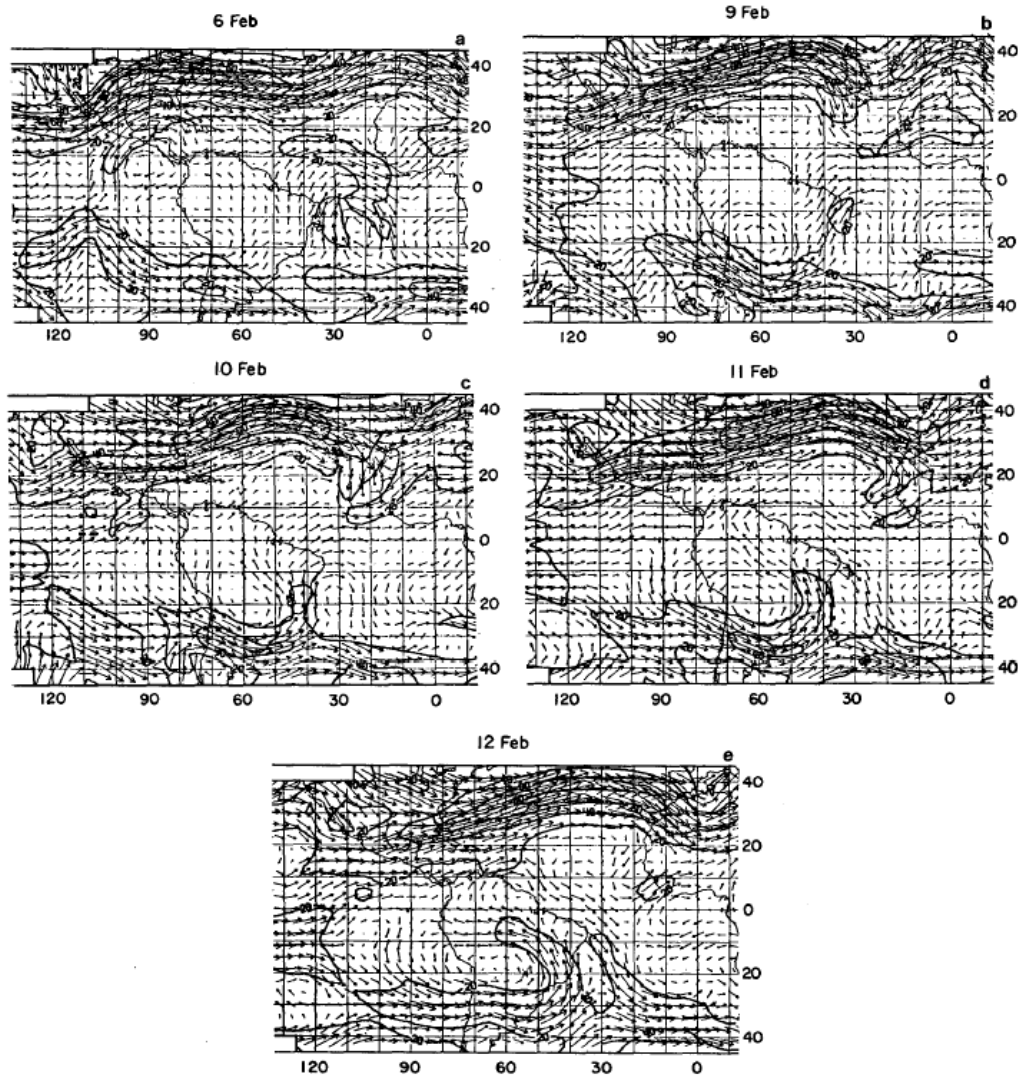


Figure 6.8: ECMWF 200 mb maps for (a) 0000 GMT on 6 February 1979 and for 9-12 February 1979 (panels b - e, respectively). (From Silva Dias *et al.* 1983)

The model results shown in Figs. 6.6 and 6.7 reproduce some of the transient aspects of the Bolivian high. As noted by Virii (1981), a southerly component of the wind dominates over most of the region east and north of the Bolivian high. This is evident in the 9-12 February period shown in Fig. 6.8, and can also be seen in the model results shown in Fig. 6.6a. The model results indicate that initially cross-equatorial flow dominates north of the forcing and that it is replaced by easterly flow as the forcing becomes negligible. A similar feature can be seen in Fig. 6.8. Between the 9th and 10th cross-equatorial flow is established north of the Bolivian

high which turns to easterly flow by the 12th. Virgi (1981) observed also maximum mean wind speeds greater than 10 m s^{-1} and exceeding 25 m s^{-1} on certain days within the latitudinal band between 5 and 10°S . The model results indicate that this equatorial easterly jet appears when the Rossby wave component of the solution becomes dominant after the forcing becomes negligible.

As is shown in Fig. 6.8, the Bolivian high has become elongated in the east-west direction and has maximum winds to the northeast by 12 February. These features are seen also in the model (Fig. 6.6). The westward elongation of the main high is caused by the westward dispersion of long Rossby waves while the sharp geopotential gradient and large wind speeds to the east are caused by the eastward dispersion of short Rossby waves.

The model results show also the formation of a trough east of the main high cell. The modal decomposition shown in Fig. 6.6 indicates that this is a manifestation of the eastward dispersion of the Rossby and mixed Rossby-gravity waves emanating from the source region. A similar trough east of the Bolivian high can be seen in Fig. 6.8 which gradually sharpens up and acquires a northwest-southeast tilt between the 9th and 12th. The anticyclonic flow which developed in the Northern Hemisphere in the model also has its counterpart in the observed flow shown in Fig. 6.8.

6.3 Wintertime cold surges

During the northern winter, the East Asian continent is dominated by a strong surface high over Siberia and northern China. Radiative cooling and persistent cold air advection throughout the troposphere maintain a layer of very cold air over the frozen land. The Tibetan plateau to the southwest restricts the movement of this cold air mass and contributes to the buildup of the surface high. A strong baroclinic zone exists between this cold continental air mass and the warm tropical air mass to its south. A manifestation of this strong baroclinic zone is the steady jet stream over the coast of East Asia. The continental anticyclone fluctuates in strength in response to midlatitude synoptic developments.

The passage of a deep upper trough in the midlatitudes often triggers intense anticyclogenesis over central China and cyclogenesis over the East China Sea. As the pressure gradient across the East China coast tightens, cold air bursts out of the continent toward the South China Sea and a cold surge is initiated. In a normal season, cold surges may occur at intervals of several days to about two weeks. In the midlatitudes, a surge arrives with a steep rise of surface pressure, a sharp drop of temperature, and a strengthening of northerly winds. The cold front leading the surge sometimes brings stratus and rain, but a strong surge is generally associated with subsiding motions that lead to a clearing of weather (Ramage 1971). Although normally the front associated with the surge cannot be followed southward of about 20°N , the surge propagates equatorward in a dramatic fashion. As a vigorous surge reaches the South China coast, northerly winds freshen almost simultaneously several hundred kilometers to the south, far beyond the region where

the winds could have pushed the front (Ramage 1971; Chang *et al.* 1979). A belt of strong northeasterly winds forms within 24 h off the South China and Vietnam coasts and leads to a strengthening of a quasi-stationary cyclonic circulation embedded in an east-northeast-west-southwest-oriented equatorial trough just north of the Borneo coast (see Fig. 6.9).

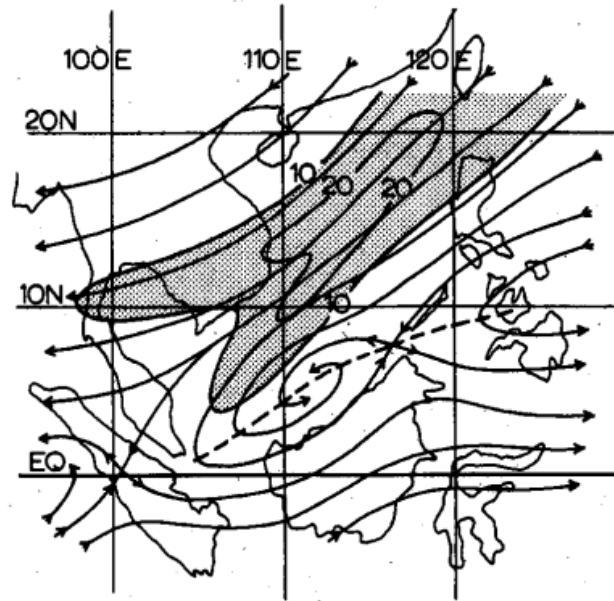


Figure 6.9: A schematic diagram of surface wind field during active winter monsoon surge. The isotachs are in units of m s^{-1} and areas with larger than 10 m s^{-1} wind speed are shaded. The thick dashed line indicates the usual position of the quasi-permanent equatorial shear line (trough) north of Borneo. (From Lim and Chang 1981)

In the equatorial region south of East Asia lies the maritime continent of Malaysia and Indonesia. During winter, extensive deep cumulus convection over this region supplies a large amount of latent heat to the atmosphere and is believed to be one of the most important energy sources that drive the winter general circulation (Ramage 1971). From the results of a series of observational studies, Chang *et al.* (1979) and Chang and Lau (1980, 1981) suggested that this equatorial convective heat source may interact with the cold surges from the north, resulting in modifications of both synoptic- and planetary scale motions. Their findings were supported by later studies (Chang and Lau 1982; Lau *et al.* 1983).

Chang and Lau (1980) summarized the sequence of events in the schematic diagram reproduced as Fig. 6.10. They noted that cold surges are often preceded by intense cooling over northern China. Such cooling appears to be due to the advection of polar air behind upper-level troughs that move rapidly eastward and deepen over northern Japan. The sinking cold air over the continent accelerates the East Asia

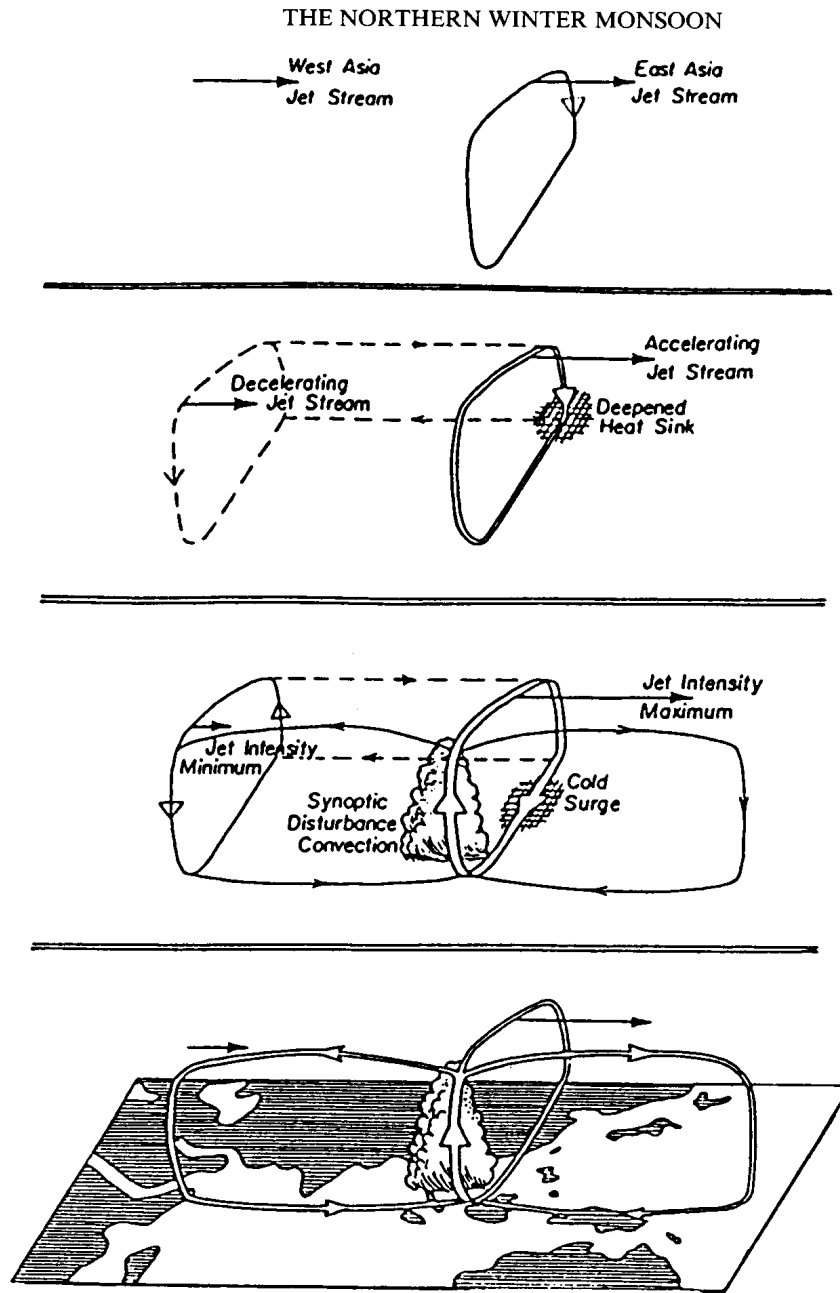


Figure 6.10: A schematic diagram . (From Lim and Chang 1981)

local Hadley cell. Almost simultaneously, the east Asian jet stream centered over Japan intensifies due to the Coriolis acceleration by the ageostrophic southerly flow of the enhanced Hadley circulation. There is also a weakening of the west Asian jet stream after a small time lag, possibly due to an induced reverse local Hadley-type circulation, as indicated in the Fig. 6.10. As a surge arrives over the equatorial

South China Sea, the existing synoptic-scale convective systems flare up and warm the tropical atmosphere by release of latent heat. The upper-level outflow from the South China Sea convection region spreads mainly east and west, driving two Walker circulations. A smaller part of the outflow returns poleward, maintaining the enhanced Hadley circulation. In this panoramic view, cold surges are seen to be an important link in a complicated chain of midlatitude tropical and equatorial east-west interactions. Through these interactions, the effect of an intense baroclinic development over the east Asian continent is spread deep across a wide equatorial belt ranging from East Africa to the mid-Pacific Ocean. Later studies indicated that a cold surge may even have influence over atmospheric motions in the Southern Hemisphere. Williams (1981) described a case of such cross-equatorial influences. About three days after a surge crossed the South China coast, he observed a slow pressure rise over western Indonesia. As if accelerated by the east-west pressure gradient, westerly winds strengthen and convective systems were observed to develop in the southern equatorial region and drift eastwards at a speed of 10 m s^{-1} . His observation was supported by Lau (1982) who found similar eastward-moving systems in a composite study of satellite imagery. Lau (1982) also investigated the meridional symmetry of such eastward-propagating cloud patterns and, with reference to the theory of Lim and Chang (1981) and Lau and Lim (1982), identified them to be Kelvin wave responses to cold surges. **Ref to Love**

Davidson *et al.* (1983) presented some data that suggested a possible relation between cold surges and the onset of the Australian monsoon (Fig. 12.2). In Fig. 6.11a, the strong northerly winds over the South China Sea show that a cold surge was in progress. Four days later, the surge winds penetrated deep into this Southern Hemisphere, and the Australian monsoon became established (Fig. 6.11b). It may be noted that the extensive cloud system associated with the Australian monsoon onset was embedded within the belt of cross-equatorial flow. This observation and the overall flow pattern give one a strong impression that the Australian monsoon and the East Asia winter monsoon cold surges may not be independent events. Chang *et al.* (1985) presented also evidence linking the Northern Hemisphere cold surges to monsoon development in the southern hemisphere tropics. In a composite of the surface flow patterns for the southern summers of 1974 to 1983, they showed that the onset of the monsoon westerlies along 10°S in the Indonesian region is sometimes preceded by a significant strengthening of northeasterly monsoon winds that persists for three to four days. This wide range of processes related to the northern winter cold surges poses challenging questions to researchers in atmospheric dynamics. How does an intense midlatitude anticyclonic development give rise to strong northeasterly surge winds over the South China Sea, which often spread so rapidly southward as to give one an impression of near-simultaneous buildup? What are the mechanisms of interaction between the cold surge and tropical convective systems? Why is it that heating of the tropical atmosphere apparently enhances Walker circulations more than Hadley circulations? Is there a dynamical interpretation for the observed midlatitude-tropical and interhemispheric interactions?

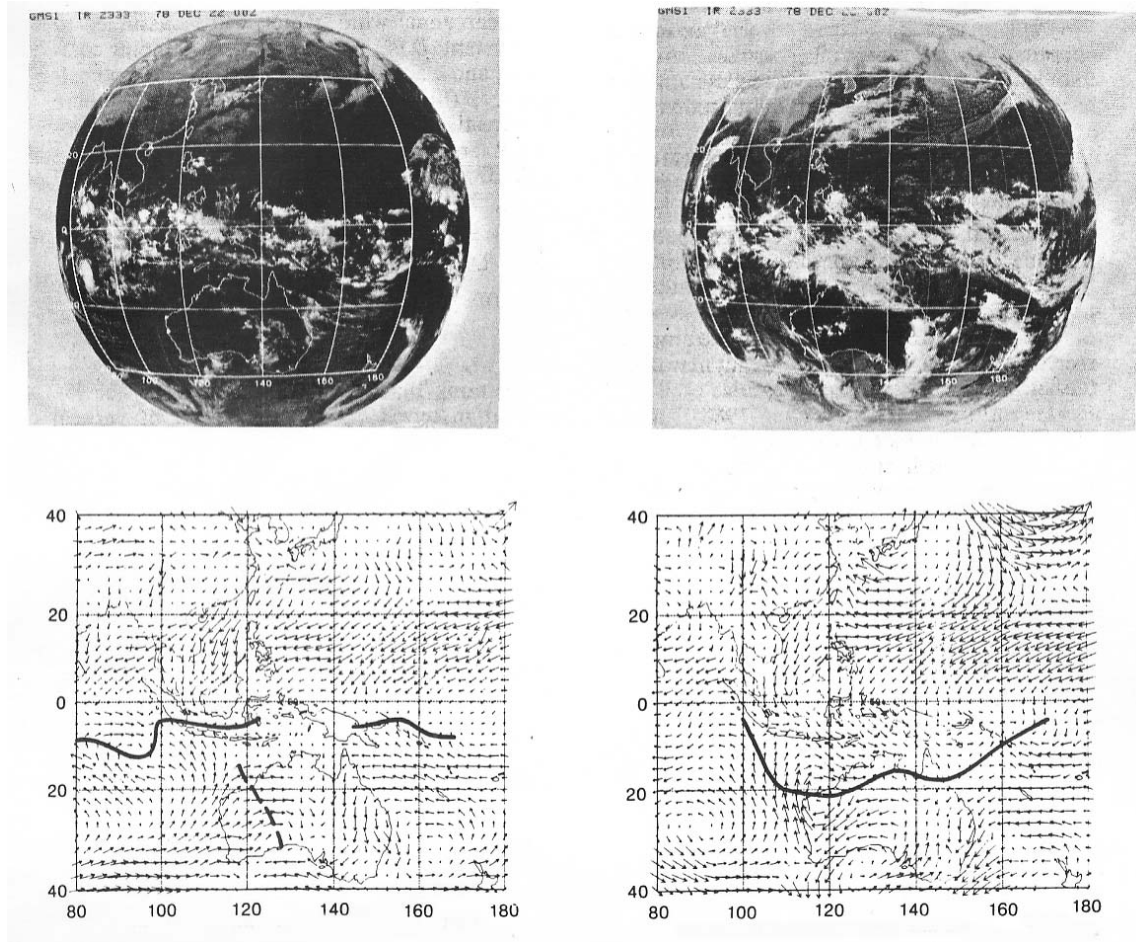


Figure 6.11: A case suggesting cold-surge influence on the Australian monsoon from (a) 00 GMT December 22, 1979 to (b) 00 GMT December 26, 1979. (From Davidson 1983.)

Lim and Chang (1981) carried out calculations similar to those of Silva Dias *et al.* (1983) in an effort to understand the northeasterly monsoon surges and associated tropical motions over southeast Asia during northern winter. They studied the dynamical response of the tropical atmosphere to midlatitude pressure surges using again the linearized shallow-water equations on an equatorial β -plane. The forcing is specified to have a Gaussian spatial distribution with a zonal scale corresponding to approximately wavenumber 7 and a meridional scale of approximately 11° . It rises rapidly from zero to maximum within one day or less and then decays slowly over 2-4 days (see Fig. 6.12).

The characteristics of the midlatitude-tropical interactions are clearly illustrated by the solution for $\tau = 15 \times 10^3$ s, or about 4 h (Fig. 6.13). On day 1, after the forcing is switched on, a belt of strong northerly and northeasterly wind sweeps across the

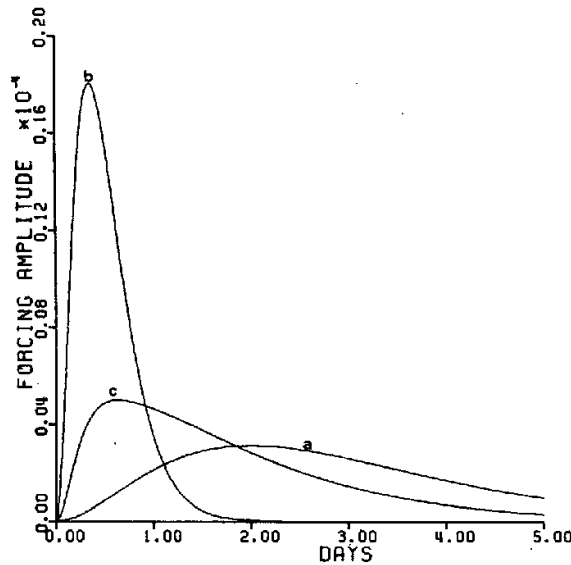


Figure 6.12: Variation of forcing amplitude with time. Curved *a* is for the first case (slow forcing with $\tau = 1$ day), curve *b* for the second case (fast forcing with $\tau = 15 \times 10^3$ s) and curve *c* for the third case (multiple time scale "realistic" forcing). Curves *a*, *b* and *c* are normalized such that the areas under them are equal. (From Lim and Chang 1981)

equator. Near the leading edge, the wind blows perpendicular to the isobars away from the high pressure, revealing strong gravity wave characteristics in the initial equatorward propagation of disturbances. More gravity wave characteristics are exhibited on day 2 when a low center and southerly winds appear behind the leading surge winds, which have now penetrated deep into the Southern Hemisphere and are deflected eastward.

From day 3 onward, the midlatitude anticyclonic circulation around the region of forcing develops a marked northeast-southwest tilt. To its south, a belt of strong northeasterly winds sweeps from the subtropical latitude to the equator. A southwesterly cross-equatorial counter flow around the longitude of the forcing becomes well established after day 6. Sandwiched between the belt of strong northeasterly winds and the southwesterly cross-equatorial flow is an equatorial trough (shear line) extending south-southwestward from about 15°N to the equator. A cyclonic vortex also develops after day 7 in the Southern Hemisphere, just to the south of the cross-equatorial flow. This large area of complex motions, which constitutes the major response of the tropical atmosphere to the midlatitude forcing, drifts slowly westwards but, for all relevant times, remains near the longitude of the forcing. This pattern of response bears a remarkable resemblance to the typical winter season flow pattern Fig. 1.27b. It suggests strongly that the surge wind belt over the South China Sea and the quasi-permanent equatorial trough north of the Borneo coast

are basically features of the dynamical response of the tropical atmosphere to the intense anticyclonic development over China prior to the initiation of a cold surge. This group of responses was identified to be an equatorial Rossby wave group. A computation using only the Rossby wave modes of $n = 1$ to 9 succeeds in reproducing, as far as a visual examination can tell, exactly all the features described (Fig. 6.14). This suggests that the high-order latitudinal modes are not important.

Lim and Chang (1981) gave an explanation also for the evolution of this response in terms of the dispersion behaviour of equatorial Rossby wave groups. From day 3 onward, there is also a group of disturbances that splits off from the Rossby mode response and propagates eastward along the equator. A band of westerlies leads the way at a speed of 30 m s^{-1} . This band of equatorial westerlies is easily identified as a Kelvin wave group. Following behind the Kelvin wave group there are some disturbances with a complicated and rapidly changing pattern. These are due mainly to the juxtaposition of a mixed Rossby-gravity wave group and an $n = 0$ inertia-gravity wave group. They reveal their identity clearly on day 8, when the equatorial eddy of the mixed Rossby-gravity waves and the col pattern of the $n = 0$ inertia-gravity waves (Fig. 6.13g and f respectively) are clearly displayed. Although the phase velocity of mixed Rossby-gravity waves is westward, their group velocity is always eastward, and this accounts for the eastward propagation of the mixed Rossby-gravity wave group. These eastward-propagating disturbances offer a plausible explanation for the drifting cloud clusters observed by Williams (1981) and Lau (1982). It is interesting also to regard this flow evolution as a geostrophic adjustment process on an equatorial β -plane. Motions generated by the pressure pulse gradually separate themselves into a geostrophic component and an ageostrophic component. The geostrophic component here is the Rossby wave group, which has quasi-geostrophic flow even at equatorial latitudes and evolves in time into a pattern resembling the winter flow field of the Southeast Asia region. The ageostrophic component concentrates its energy into the $n = -1$ mode Kelvin waves and the $n = 0$ mode mixed Rossby-gravity waves and inertia-gravity waves in the form of a complicated train of eastward-propagating disturbances.

In summary, Lim and Chang (1981) investigated the dynamics of midlatitude tropical interactions based on the concept of vertical modes. When the mean winds and damping effects are independent of the vertical coordinates, when there is no planetary boundary layer effects, and when the stability parameter is a function of the vertical coordinate only, the equations of motion may be separated into a complete set of vertical modes. Each of these modes is characterized by an equivalent depth, and the evolution of its horizontal structure is governed by a shallow-water equation system having the equivalent depth as its scale height.

It turns out that the existence of horizontal wind shear does not affect the separation of motions into vertical modes, but can lead to qualitative changes in the horizontal structure of the vertical modes. Vertical modes of large equivalent depth ($c > 120 \text{ m s}^{-1}$) have a nearly constant profile in the troposphere. They represent atmospheric motions that have a barotropic structure. Vertical modes with a

medium equivalent depth ($30 \text{ m s}^{-1} < c < 50 \text{ m s}^{-1}$) have a single phase reversal in the midtroposphere (and probably more phase reversals in the stratosphere). Motions associated with these modes have opposite phase in the upper and the lower troposphere, i.e. they are baroclinic motions. In an equatorial β -plane model, free waves of the large equivalent-depth modes have broad latitudinal extent. Motions associated with these modes readily propagate to high latitudes and tend to spread their energy over the whole globe. Tropical influences spread to high latitudes from the tropics, such as the teleconnection patterns, therefore have barotropic vertical structure. Free waves of the medium equivalent-depth modes are trapped within the tropics. Motions associated with these modes excited in the midlatitudes tend to propagate equatorward and hence bring midlatitude influence to the tropics. Tropical motions forced from midlatitudes therefore have baroclinic structure. When damping is weak, the small equivalent-depth modes ($c < 20 \text{ m s}^{-1}$) may survive their slow meridional propagation and exhibit themselves in equatorial motions of complicated vertical structure (short vertical wavelength).

The mechanisms of midlatitude influence on the tropics were clearly illustrated by a study of atmospheric response to a midlatitude pressure surge. In the midlatitudes, the pressure surge generates a simple anticyclonic circulation, which gradually develops northeast-southwest tilt. However, much of the motion excited by the pressure surge spreads equatorward. The energy of the ageostrophic flow components concentrates into equatorial Kelvin waves and mixed Rossby-gravity waves, which are manifest as disturbances propagating eastward along the equator. The energy residing in geostrophically-balanced flow goes into equatorial Rossby waves. The dispersion of equatorial Rossby wave groups gives rise to a complex flow pattern with a band of strong northeasterly winds (the surge), an equatorial trough, and a cross-equatorial current. All these features bear remarkable resemblance to the typical winter flow pattern over Southeast Asia.

A very important basic question that has not been addressed in this chapter is the interaction of heat sources and atmospheric motions. Unlike our models where heat sources are prescribed, heat sources in the real atmosphere are often forced by the motion field. The feedback of motion field to heat source in the tropics is basically the problem of parameterization of cumulus convection—a problem where basic understanding is still lacking. Previous theoretical studies addressing this problem are mostly based on the CISK formulation, which is itself based on rather restrictive and somewhat artificial assumptions. To make significant advance in this problem, we will probably need to carry out further studies using numerical models with physically realistic parameterization schemes for convective heating. Although we are still far from a solution of this fundamental problem, the studies that have been carried out should serve to remind us that by using models with prescribed heat sources, we are studying at most half, and probably it is the easier half, of the problem.

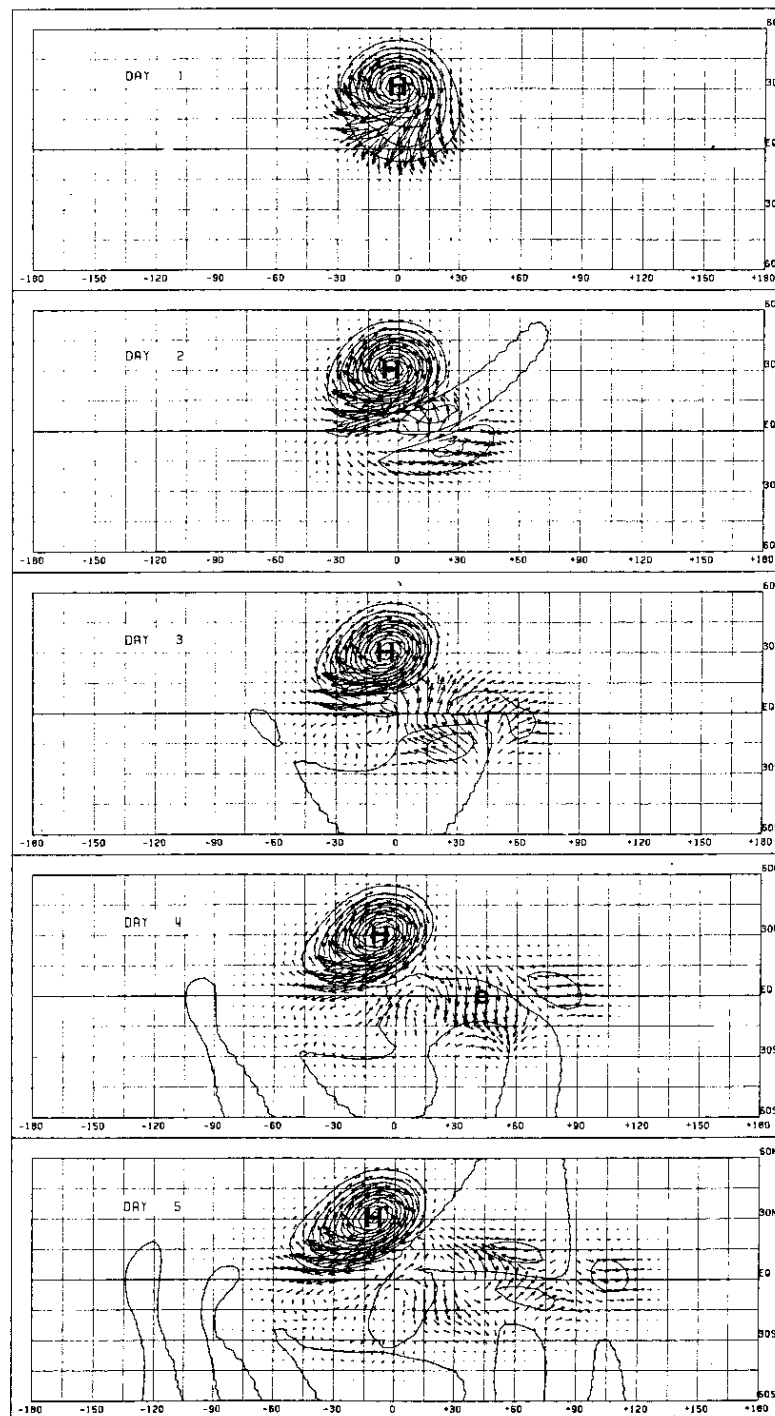


Figure 6.13: Transient local mass source at about 30°N turned on at time 0. The sequence of figures shows the spread of midlatitude influence to the tropics. The ageostrophic flow component concentrates its energy into Kelvin waves and mixed Rossby gravity-waves, which propagate to between longitude $+30$ to 120 on day 9. The Rossby mode response remains near the region of forcing between longitude 90 to $+15$ on day 9. (From Lim and Chang 1987)

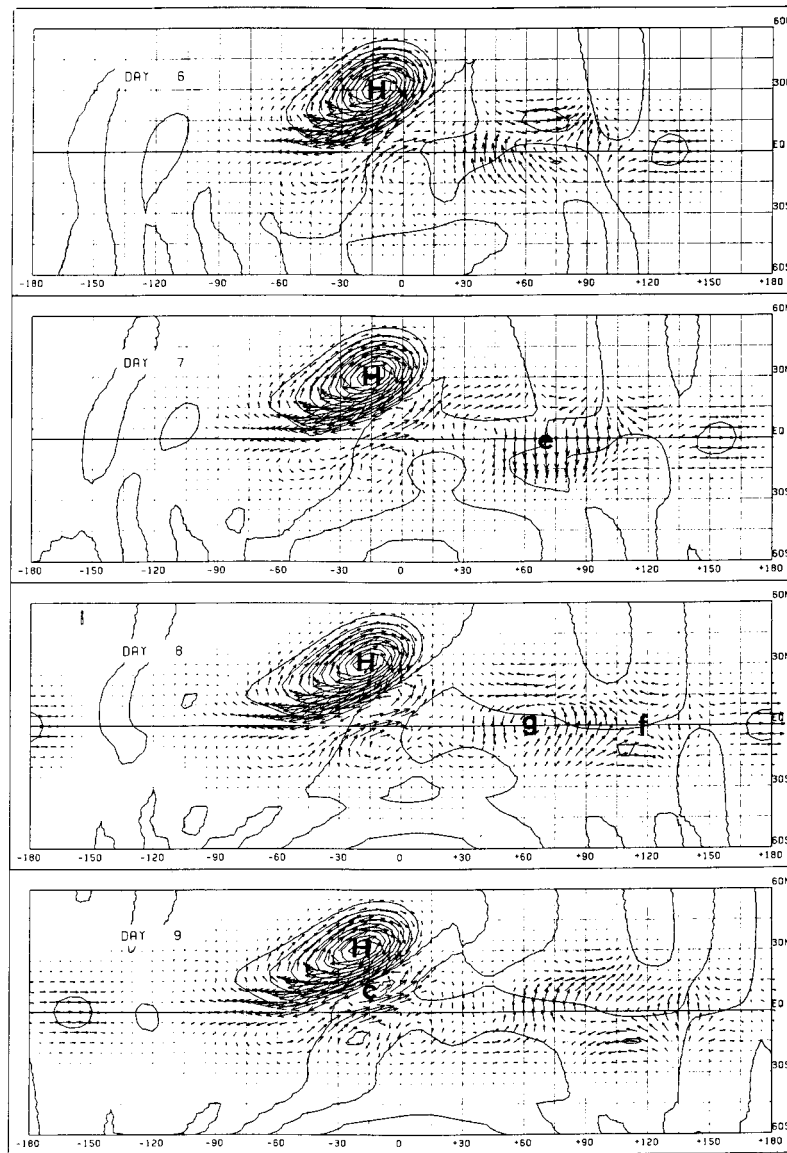


Figure 6.13 continued

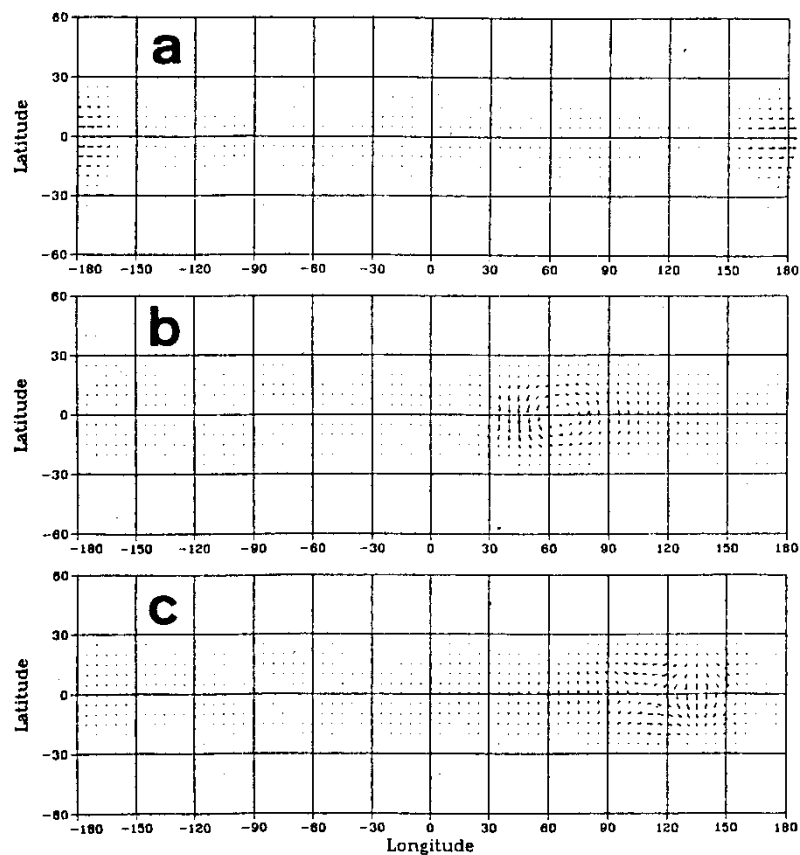


Figure 6.14: The wave groups of different wave modes at day 8. (a) Kelvin wave group ($n = -1$). (b) Mixed Rossby-gravity wave group on $n = 0$. (c) Inertia-gravity wave group of $n = 0$. (d)-(f) Rossby wave groups of $n = 1$ to 4. (g) The combined velocity field of Rossby wave groups of $n = 1$ to 9. (From Lim and Chang 1987)

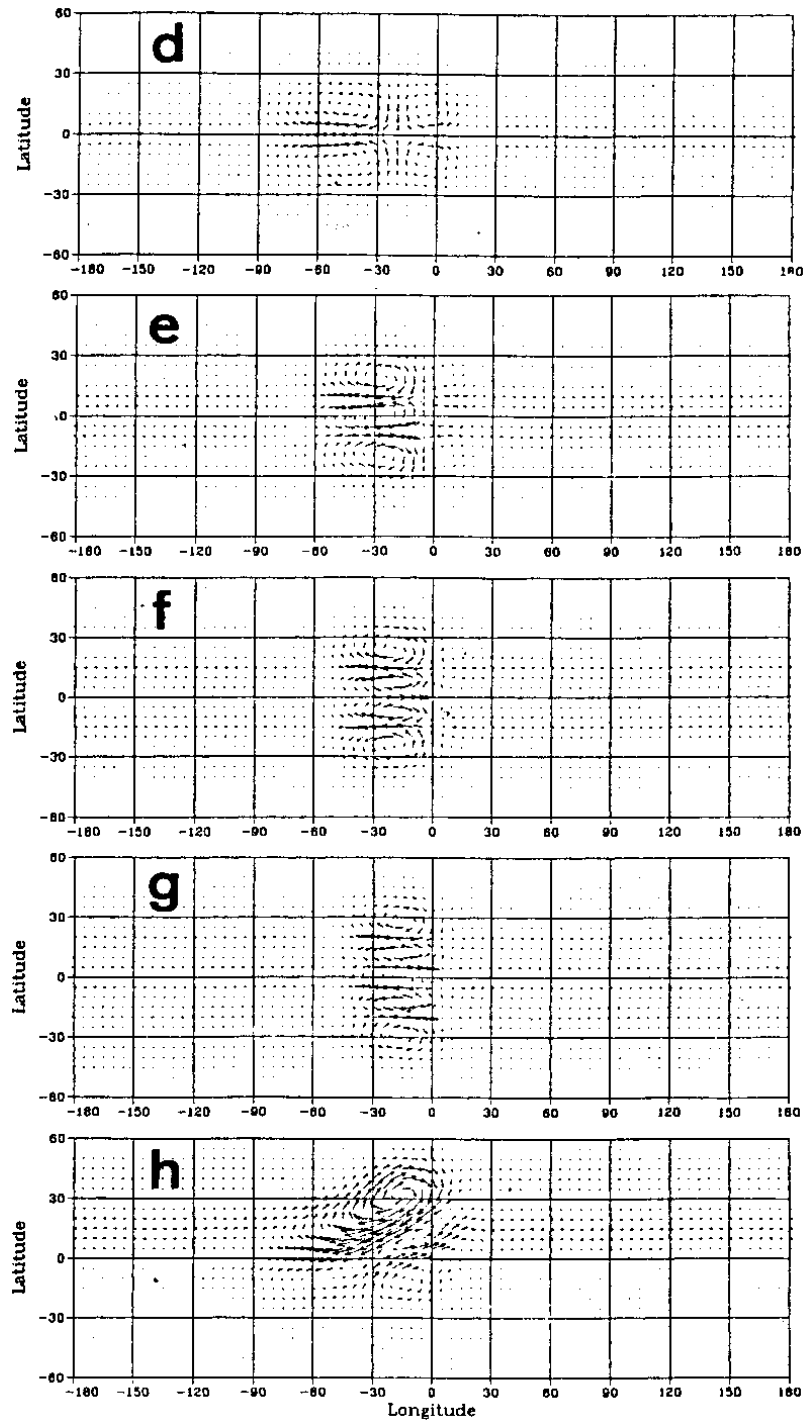


Figure 6.14 continued

Chapter 7

MOIST CONVECTION AND CONVECTIVE SYSTEMS

The discussion of Chapter 1 combined with the scaling analysis of Chapter 2 suggest that the release of latent heat of condensation is a primary driving mechanism for tropical weather systems including tropical depressions and tropical cyclones. A problem is that tropical precipitation occurs for the most part in cells of deep cumulus convection with diameters on the order of 1 to 10 km and it is not easy to see how these cells are organized so as to supply energy to a depression whose scale is on the order of 1000 km. Charney (1973) pointed out that most tropical depressions form in the ITCZ. As noted earlier, this is a narrow zone paralleling the equator, but lying at some distance from it, in which air from one hemisphere converges towards air from the other to produce cloud and precipitation. The ITCZ is characterized by low pressure and cyclonic relative vorticity near the surface. Charney suggested that the mechanism which leads to the formation of the tropical depression may be responsible also for the formation of the ITCZ itself.

In order to make progress in understanding convectively-driven weather systems in the tropics, it will be necessary to separate the two scales of motion, the large-scale system itself, and the cumulus cloud scale. We shall need to find ways of representing the gross effect of the clouds in terms of variables that describe the large scale itself, a problem referred to as the cumulus parameterization problem. To begin with we consider certain basic aspects of moist convection, including those that distinguish it in a fundamental way from dry convection. We go on to consider the conditions that lead to convection and the nature of individual clouds, distinguishing between clouds that precipitate and those that do not. Finally we examine the effects of a field of convective clouds on its environment and vice versa.

7.1 Moist versus dry convection

It is instructive at the outset to consider the differences between moist convection and dry convection. In dry convection, the convective elements (or eddies) have

horizontal and vertical scales that are comparable in size. They have also upward and downward motions that are comparable in strength. In contrast, in moist convection, the regions of ascent occupy a much smaller area than the regions of descent and the updraughts are, in general, much stronger than the downdraughts, except in certain organized precipitating cloud systems. Thus, in moist convection there is a strong bias towards kinetic energy production in regions of ascent. Another feature of moist convection that distinguishes it from dry convection is the presence and dynamical influence of condensate.

In moist convection, instability is released in relatively small, isolated regions where water is condensed and evaporated, whereas surrounding regions remain statically stable and are therefore capable of supporting gravity waves. This renders the problem inherently nonlinear, since the static stability of the cloud environment must be regarded as a function of the vertical velocity therein in order to capture even the most elementary aspects of convection.

In summary, dry convection involves the entire convectively-unstable region in motion and there exists a strong symmetry between updraughts and downdraughts, whereas moist convection may lead to small pockets of rapidly ascending air embedded within large regions of relatively quiescent, stably-stratified air. This asymmetry has an important bearing on the dynamics of convection and convective systems and has a strong influence on the interaction between convection and the larger scale flow.

An important consequence of phase change and the accompanying release of latent heat is the conditional nature of moist instability, i.e., a finite amplitude displacement of air to its level of free convection (LFC) is necessary for instability. This contributes also to the fundamental nonlinearity of convection. In middle latitudes, where displacements of air parcels to their LFC can require a great deal of work against the stable stratification, the problem of when and where conditional instability will actually be released can be particularly difficult.

Some aspects of the response of a stably-stratified environment to convective clouds can be illustrated using rather simple theory. We shall regard latent heat release as the most important aspect of deep convection and shall ignore for the most part momentum transports and other effects.

7.2 Conditional instability

We usually assess the instability of the atmosphere to convection with the help of an aerological diagram (Fig. 7.1). Data on temperature (T), dew-point temperature (T_d) and pressure (p) obtained from a radiosonde sounding are plotted on the diagram. The two points (p, T) and (p, T_d) at a particular pressure uniquely characterize the state of a sample of moist unsaturated air. Thus the complete state of the atmosphere is characterized by the two curves on the diagram.

The radiosonde sounding plotted in Fig. 7.1 is an idealized sounding that is conditionally unstable to deep convection. The air at low levels is well-mixed as

the temperature curve is parallel to a dry adiabat. If an air parcel in this layer were lifted without mixing with its environment, the two points characterizing its state, (p, T) and (p, T_d) , would move along the dry adiabat and saturation mixing ratio line, respectively, until the parcel became saturated at the lifting condensation level (LCL). Above the LCL $T = T_d$, but the state of the parcel depends on what assumption one makes about the fate of condensate. It is common to assume that the parcel rises pseudo-adiabatically¹ above this level, whereupon its state would follow along the pseudo-adiabat passing through the LCL. If the parcel is lifted above its LCL, to begin with its temperature is less than that of its environment and it will have negative buoyancy². However, if lifting continues, the parcel will eventually become warmer than its environment at the point where the pseudo-adiabat crosses the temperature sounding, i.e. at the LFC. Thereafter the parcel could rise freely under its own positive buoyancy until it reached the level of neutral buoyancy (LNB). In other words a certain minimum vertical displacement is required to release the instability. The amount of potential energy that is released as the parcel rises from its LFC to its LNB is proportional to the area between the environmental temperature curve and the pseudo-adiabat between these levels and is called the positive area. The amount of work that has to be performed to raise the parcel from its LCL to its LFC is again proportional to the area between the environmental temperature curve and the pseudo-adiabat between these levels and is called the negative area, or the convective inhibition (CIN). The net amount of work that can be released as the parcel rises from its LCL to its LNB is called the convective available potential energy, or CAPE. Clearly, the CAPE is just the positive area minus the negative area³.

We refer to this kind of instability as metastability, or conditional instability. The instability can be released only if air parcels can be lifted to their LFC, or, alternatively, if rising air parcels in the mixed layer have enough vertical kinetic energy to overcome the CIN. If the inversion above the mixed layer is relatively strong, the CIN may be too large for this to happen and deep convection will not occur.

7.3 Shallow convection

Typically, shallow convection occurs when thermals rising through the convective boundary layer reach their LFC, but when there exists an inversion layer and/or a layer of dry air to limit the vertical penetration of the clouds. As the clouds penetrate the inversion, they rapidly reach their LNB; thereafter they become negatively buoyant

¹“pseudo-adiabatically” means that all condensate is assumed to fall out of the parcel and the latent heat released is all used to heat the parcel. For shallow clouds that do not precipitate, it is a better approximation to assume reversible ascent in which the condensate remains in the parcel.

²Strictly, buoyancy is related to the virtual temperature difference.

³Some authors define CAPE as simply the positive area, but the differences are often small in conditions that are strongly convectively-unstable.

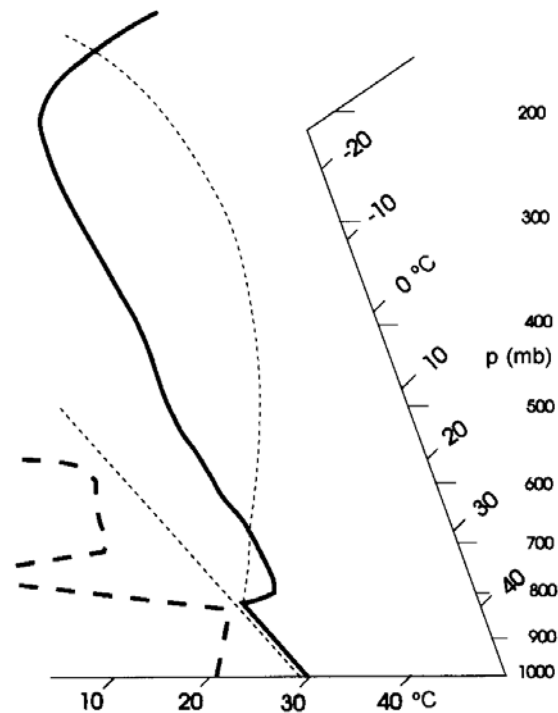


Figure 7.1: Schematic of a radiosonde sounding in a conditionally-unstable atmosphere.

and decelerate. It often happens that the air above the inversion is relatively dry and the clouds rapidly evaporate as a result of mixing with ambient air. One can show that this mixing always leads to negative buoyancy in the affected air (see e.g. Emanuel, 1997). Shallow clouds transport air with low potential temperature, but rich in moisture, aloft, while the intra-cloud subsidence carries drier air with larger potential temperature into the subcloud layer. Thus shallow clouds act effectively to moisten and cool the air aloft and to warm and dry the subcloud layer. By definition, shallow clouds do not precipitate and the tiny cloud droplets tend to be carried along with the air. Accordingly, the thermodynamic processes within them are better represented by assuming reversible moist ascent rather than pseudo-adiabatic ascent. Shallow convection in the form of trade-wind cumuli is ubiquitous over the warm tropical oceans (see Fig. 7.2).

7.4 Precipitating convection

The simplest type of precipitating convective system is the airmass shower or thunderstorm, whose life cycle is depicted in Fig. 7.3. Storms of this type occur in environments with weak vertical shear and have lifetimes on the order of an hour. They begin as vigorous cumulus updraughts, but as they grow deeper, precipitation



(a)



(b)

Figure 7.2: Trade-wind cumuli. Photographs by Roger Smith

develops within the lower part of the updraught, thereby weakening it and eventually reversing the flow into a downdraught. Beyond this stage, the cloud steadily decays,

perhaps leaving behind an anvil of ice cloud aloft, which is slower to evaporate than the liquid water part at lower levels. Although large amounts of latent heat are released in the updraught during the condensation process, the ascending air parcels cool adiabatically as they expand so that only modest temperature rises occur. For the most part, the temperature in the updraught is no more than a few degrees warmer than the environmental temperature at the same level. The re-evaporation of cloud consumes latent heat so that the net heating of the air depends finally on the amount of water that reaches the ground as precipitation. Ascent within the cloud updraught is accompanied by descent in the cloud environment, a process that involves internal gravity waves as explained in section 7.6. Adiabatic compression associated with this subsidence can warm the cloud environment far from the cloud and is the means by which the latent heat released in the updraught is communicated to the air surrounding the cloud. The evaporation of cloud raises the humidity of the air at the level where the evaporation occurs so that cloud updraughts transport moisture upwards. However, this moistening of the near-cloud air is opposed by the subsidence of drier air from aloft (in general, the water vapour mixing ratio decreases with height) so that overall, deep precipitating clouds tend to warm and dry their environment.

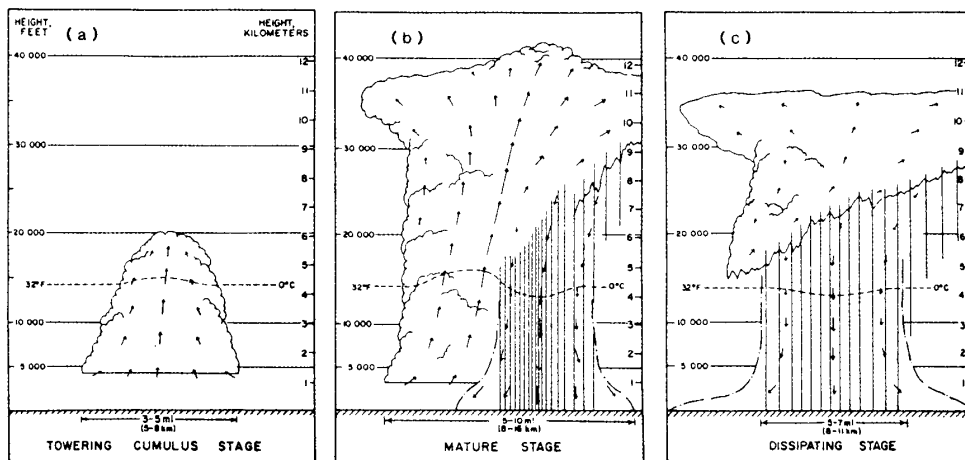


Figure 7.3: Schematic diagram illustrating the three important stages in the life cycle of an airmass thunderstorm: (a) the cumulus stage; (b) the mature stage; and (c) the dissipating stage. (From *The Thunderstorm Project*, 1947)

7.5 Precipitation-cooled downdraughts

An important characteristic of precipitating convection and of mesoscale convective systems is the formation of downdraughts. These are driven in part by the drag ex-

erted on the air by the precipitation and in part by the negative buoyancy associated with the cooling that occurs when precipitation evaporates in unsaturated air, or when it melts at the freezing level.

The potential for generating downdraught kinetic energy by evaporation can be assessed as follows. Consider, for example, an unsaturated air parcel below cloud base. We imagine a two-stage process in which the air parcel is cooled isobarically in situ by the evaporation of precipitation falling into it until it reaches its wet-bulb temperature⁴. We assume that the air parcel then descends along a pseudo-adiabat, with just enough evaporation occurring to keep it saturated. Figure 7.4 illustrates this process in an aerological diagram. If the parcel begins its descent at pressure p_i and reaches the surface (or its level of neutral buoyancy) at pressure p_o , the energy that is made available is the area between the environmental curve and the process curve between the two pressures. We call this the downdraught convective available potential energy (DCAPE).

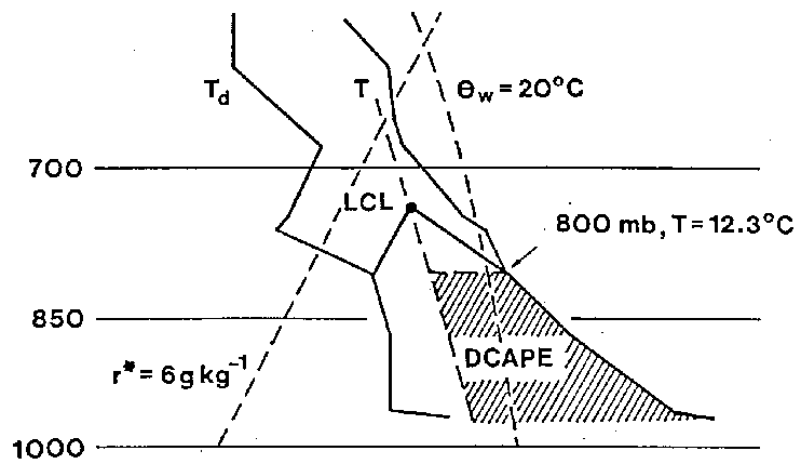


Figure 7.4: A section of a radiosonde sounding showing the graphical determination of DCAPE for an air parcel at 800 mb. The method assumes a process in which the air parcel is first cooled isobarically to its wet bulb temperature by the evaporation of rain into it and then descends to the surface along the pseudo-adiabat through this point, with just enough further evaporation of rain to keep it just saturated.

Clearly DCAPE increases as the relative humidity of the parcel in its initial state decreases. In reality, there may not be enough evaporation to maintain the saturation of a parcel throughout its descent so that we may expect DCAPE to provide an upper limit to the downdraught energy that is realized. Indeed, the actual DCAPE depends sensitively on the amount of rain that actually evaporates.

⁴The wet-bulb temperature is the temperature attained by a sample of moist air when water is evaporated into it at constant pressure until it is saturated, the latent heat being provided by the air sample itself. It can be measured by ventilating a thermometer whose sensing bulb is kept wet by a piece of damp cloth (from which the term ‘wet-bulb’ arises).

In general, precipitation-driven downdraughts are important aspects of deep convection and have a major impact on the subcloud layer, the layer of air below cloud base. When the lower troposphere is relative dry, downdraughts associated with evaporating precipitation from deep convection moisten and cool the boundary layer (Betts, 1976). Two processes are involved, evaporation and downward transport. Evaporation of falling precipitation into the unsaturated sub-cloud layer is a heat sink and moisture source and brings the layer closer to saturation at constant equivalent potential temperature (or moist static energy). The cooling produces negative buoyancy, which together with the drag of falling precipitation generates the downdraught. The downdraught transports potentially warmer and drier air into the sub-cloud layer. The two processes oppose each other in the sense that evaporation cools and moistens while downward transport warms and dries. Betts points out any combination can result, but the observations he reports suggest that the sub-cloud layer becomes cooler and drier after the precipitation and downdraughts. The coolness implies that there is sufficient evaporation into subsiding air to offset the adiabatic warming and the dryness is a consequence of the fact that even the saturation mixing ratio of subsiding air is still lower than that of the boundary layer.

The downdraughts of cool air spread out near the surface as gravity currents and a so-called gust front forms near their leading edge. Air parcels ahead of the gust front are lifted above the cold air and the lifting may be enough to carry them to their LFC, thereby generating new convective cells. This process is believed to be important in maintaining convective activity and it should persist until the downdraughts have replaced most of the unstable air.

7.6 Organized convective systems

When the horizontal wind in a particular air mass has significant vertical shear, deep convective systems have the capacity to become organized in a way that they are able to resist the destructive effects of precipitation-cooled downdraughts. Such systems are often severe and long-lived. Well-documented examples are multicell and supercell thunderstorms, and various types of squall lines (see e.g. Houze, 1993, Chapters 8 and 9; Emanuel, 1994, Chapter 9). There is a tendency also for deep convective clouds to aggregate into clusters of considerably larger scale than individual clouds. One theory is that new clouds are initiated by the lifting of moist low-level air along the gust fronts of older systems (e.g. Mapes, 1993; Kingsmill and Houze, 1999). Such clusters are longer lived than the individual clouds comprising them, their longevity being dependent on a continued presence of processes that destabilize the environment, e.g. radiative cooling of the air aloft and the supply of moisture from the surface. In general there is a diurnal modulation of convection also; convective activity over land tends to peak during the late afternoon or early evening, whereas, over the tropical oceans, the peak occurs a little before sunrise (Gray and Jacobson, 1977). The reasons for the morning maximum over the oceans is thought to be a consequence of the radiative forcing of organized weather systems

associated with diurnal variations in tropospheric radiational cooling between the weather system and its surrounding cloud-free region.

7.7 Clouds in the tropics

Clouds in the tropics occur in a spectrum of sizes ranging from small isolated cumulus to large "cloud clusters". The cloud clusters are identified in satellite pictures by their mesoscale cirrus shields, each shield being ~ 100 - 1000 km in dimension. Statistical studies indicate that the tropical cloud spectrum, whether measured in terms of height, area, duration, or rainfall rate, tend to be distributed log-normally. That is, smaller, isolated cumulus and cumulonimbus greatly outnumber cloud clusters. Nevertheless, the cloud clusters, owing to their size, dominate the mean cloudiness and total precipitation of the tropics. They contain continuous rain areas covering up to 5×10^4 km².

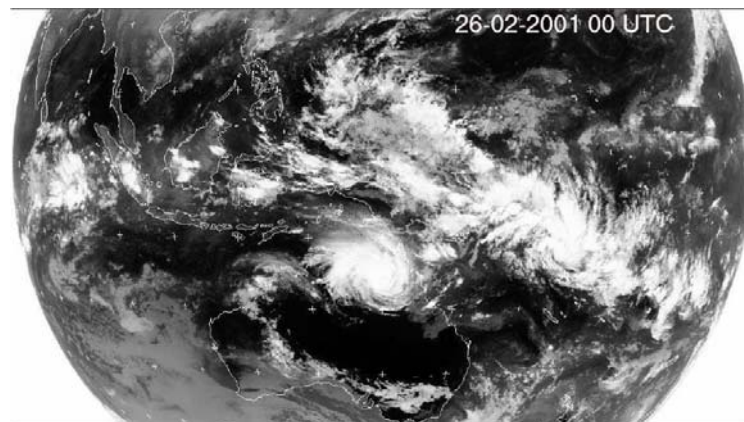
Cloud clusters generally have lifetimes of a day or less and are confined to very low latitudes. Occasionally, however, a cluster evolves into a longer lived tropical storm or even a tropical cyclone⁵, which can move out of the tropics and into the midlatitudes.

The tendency for convection to form clusters is apparent in Fig. 7.5, which shows the GMS-IR satellite imagery at 0000 UTC and 2100 UTC on 26 February 2001. The bright white clouds throughout the tropics have cold tops and are mostly cirrus debris from deep convection. Active convective updraughts occupy only a small fraction of this area at any one time. Figure 7.5a shows a tropical cyclone forming from a convective cloud cluster, or convective system, over the Gulf of Carpentaria in northeastern Australia. In the 21 h between this image and the one in Fig. 7.5b, a second tropical cyclone has emerged from the cloud mass to the north of New Caledonia.

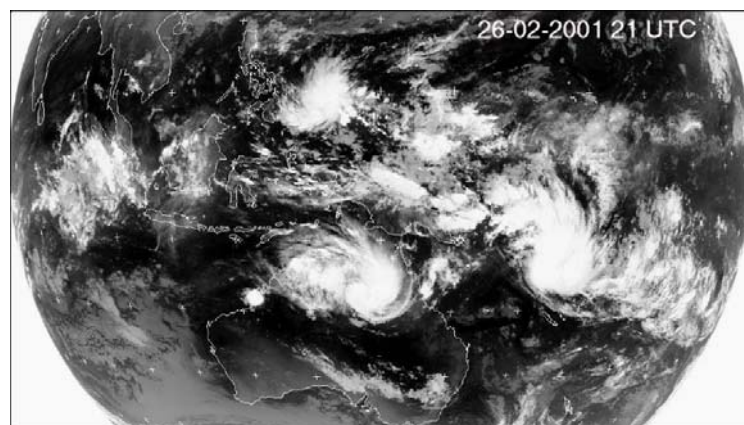
Two types of cloud clusters are generally recognized. Squall clusters are associated with tropical squall lines and are notable for their rapid propagation (15 ms^{-1}), explosive growth, high brightness in IR-satellite imagery, and their distinct convex leading edge. Nonsquall clusters travel more slowly (typically only a few ms^{-1}) and do not possess the distinctive oval cirrus shield or arc-shaped leading edge of squall systems. Figure 7.6 shows a series of squall systems over West Africa, where they are common at certain times of the year. The easterly wave disturbances with which they are associated sometimes develop into hurricanes over the Atlantic Ocean.

Beneath the large cirrus shield that identifies a cloud cluster in satellite imagery there is typically found one or more mesoscale rain areas, each a maximum horizontal dimension ~ 100 - 500 km. Leary and Houze (1979a) extended the conceptual model

⁵Tropical cyclone is the generic name given to cyclonically rotating storms in the tropics, when the maximum near surface 10 min sustained wind speed exceeds 32 ms^{-1} . Severe tropical cyclones, known as *hurricanes* over the Atlantic, Caribbean and eastern Pacific, and *typhoons* over the western Pacific have near surface 10 min sustained wind speed exceeding 64 ms^{-1} . Unlike the rest of the world, the United States adopts a 1 min. sustained wind speed for the definition.



(a)



(b)

Figure 7.5: GMS-IR satellite images for 26 February 2001, (a) 0000 UTC, (b) 2100 UTC.

of a tropical squall-line system (Fig. 7.7) to describe the structure and behaviour of these rain areas. They arrived at the more general concept of a "mesoscale precipitation feature" (MPF), of which the rain area of a squall cluster is an example, but which also applies to the rain areas of nonsquall clusters.

Squall clusters and some nonsquall clusters contain just one MPF, while other clusters contain several MPFs interconnected by a common mid- to upper-level cloud shield. Intersections and mergers of the MPFs can add complexity to the precipitation pattern of the cluster. However, Leary and Houze (1979a) found that when the individual MPFs making up the pattern are identified and followed closely in time, they each exhibit a life cycle similar to that of a squall-line MPF. Figure 7.8

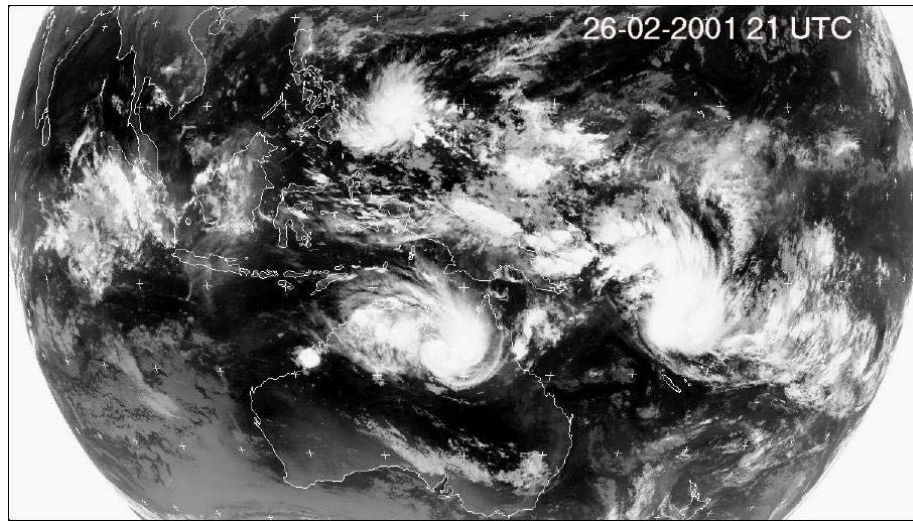


Figure 7.6: METEOSAT water-vapour satellite imagery for 17 June 1997 showing an unusually well developed series of squall line cloud clusters over West Africa.

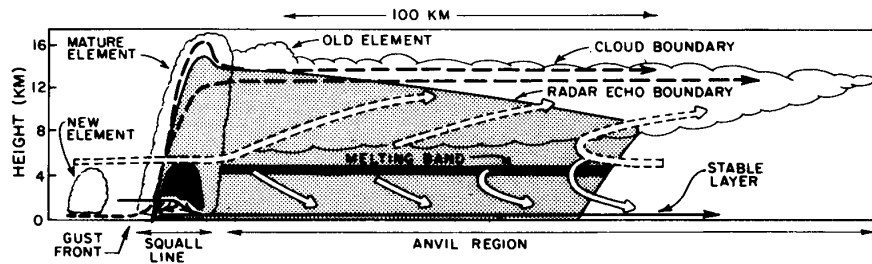


Figure 7.7: Schematic of a typical cross section through a tropical squall system. Dashed streamlines show convective-scale updraught and downdraught motions associated with the mature squall-line element. Wide solid arrows show mesoscale downdraught circulation. Wide dashed arrows show mesoscale updraught circulation. Dark shading shows strong radar echo in the melting band and in the heavy precipitation zone of the mature squall-line element. Light shading shows weaker radar echoes. Scalloped line indicates visible cloud boundary. (From Houze and Hobbs, 1982).

illustrates this life cycle using as an example nonsquall clusters that were observed over the South China Sea during winter MONEX. These clusters formed diurnally off the northern coast of Borneo and typically contained one MPF (Fig. 7.8), which progressed through the stages of the life cycle identified by Leary and Houze (1979a).

The formative stage of an MPF is initiated with an imposed mesoscale convergence at low levels (Zipser, 1980). This convergence may be associated with a

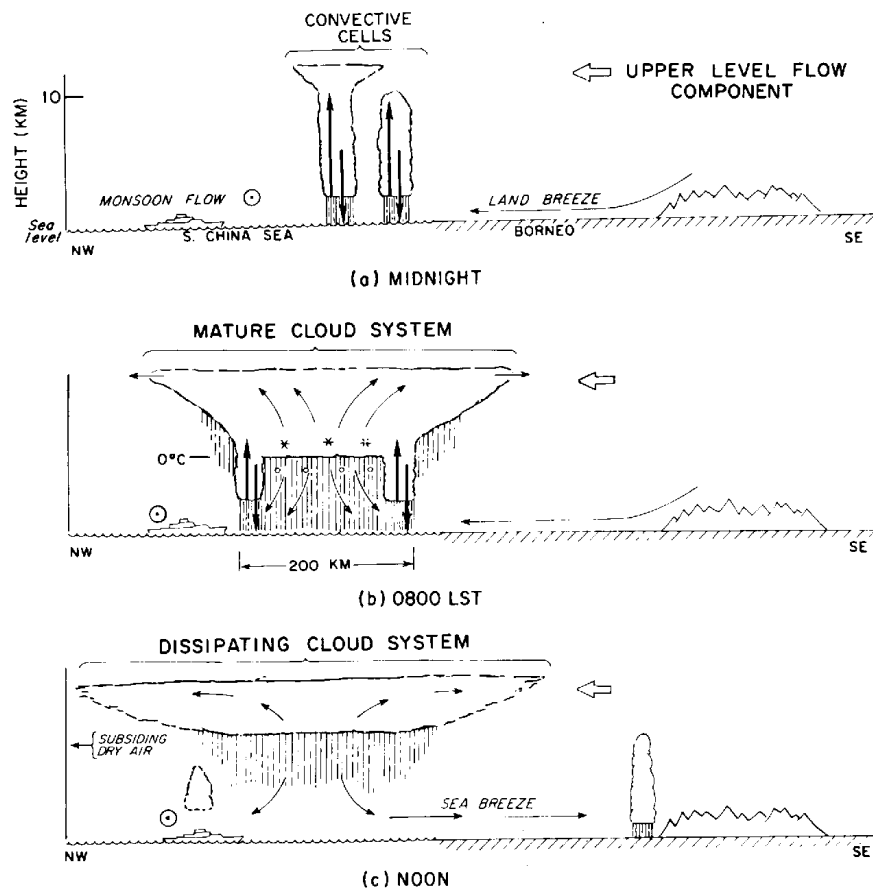


Figure 7.8: Schematic of the development of diurnally generated non-squall cloud cluster off the coast of Borneo. Various arrows indicate airflow. Circumscribed dot indicates northeasterly monsoon flow out of page. Wide open arrow indicates the component of the typical east-southeasterly upper-level flow in the plane of the cross section. Heavy vertical arrows in (a) and (b) indicate cumulus-scale updrafts and downdrafts. Thin arrows in (b) and (c) show a mesoscale updraft developing in a mid- to upper-level stratiform cloud with a mesoscale downdraft in the rain below the middle-level base of the stratiform cloud. Asterisks and small circles indicate ice above the 0C level melting to form raindrops just below this level. (From Houze *et al.*, 1981a)

downdraft outflow boundary from a previous cloud cluster, a confluence line in a larger scale flow, or some other feature that intensifies convergence locally. The winter monsoon clusters used as an example here are triggered by the convergence of the nocturnal land breeze from Borneo with the large-scale northeasterly monsoon flow over the South China Sea Fig. 7.8a. The triggering of convection by low-level convergence is followed by the growth of several discrete cumulonimbus elements, which may be randomly distributed in a group or arranged in a line. This initial

spatial arrangement probably depends on the form of the initiating convergence. The intensifying stage of the MPF is not shown explicitly in Fig. 7.8. It corresponds to the period of transition between Figs. 7.8a and b. During this stage, older convective elements grow and merge while newer elements continue to form. Gradually, this process leads to a large continuous rain area composed of convective cells interconnected by stratiform precipitation of moderate intensity falling from a spreading mid- to upper-level stratiform cloud shield. The mature stage of the MPF is reached when the stratiform precipitation between cells becomes quite extensive, covering areas 100-200 km in horizontal dimension (region between cells in Fig. 7.8). This stratiform precipitation resembles that associated with the anvil clouds of squall clusters. Associated with the stratiform precipitation region of a nonsquall MPF, moreover, are a mesoscale downdraft below the melting level and a mesoscale updraft above, similar to those of squall-line anvils. In the dissipating stage of a cluster's MPF, the formation of new convective cells diminishes. However, the feature can persist for several hours as a region of mostly mid- to upper-level cloud, with continuing light precipitation or virga (Fig. 7.8c).

Figures 7.9 and 7.10 show the typical structure of squall lines. Prominent features are the rather narrow region of strong ascent in convective cells at the leading edge of the squall system with a much more extensive stratiform anvil region behind. Light to moderate rain falls out of the anvil.

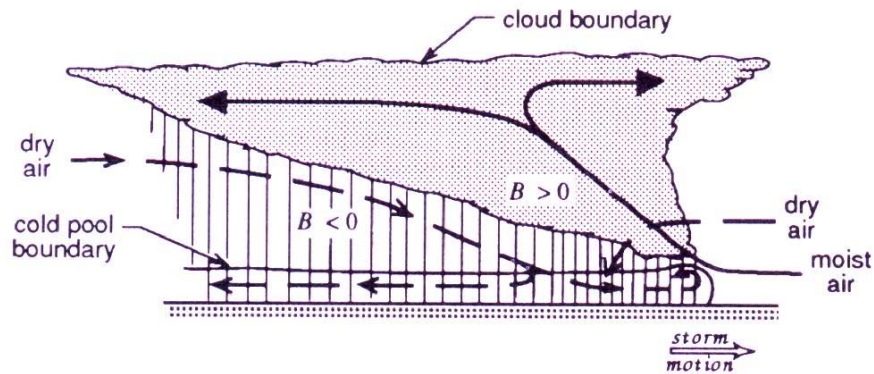


Figure 7.9: Conceptualization of the convective portion of the squall line with trailing stratiform precipitation, with emphasis on the flow of water vapour into and out of the storm. The buoyancy is denoted by B . All flow is relative to the squall line, which is moving from right to left. Numbers in ellipses are typical values of equivalent potential temperature (in K). (From Fovell, 1990)

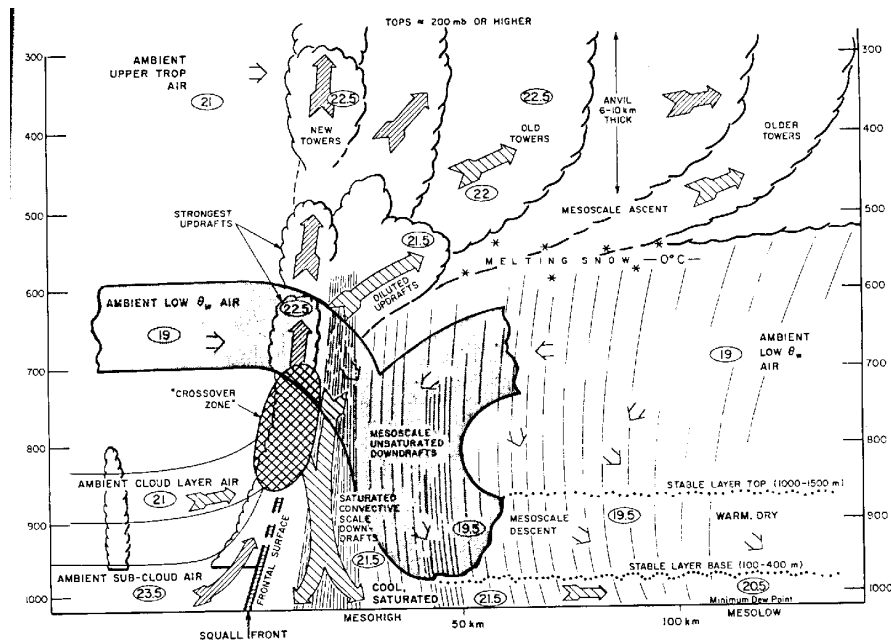


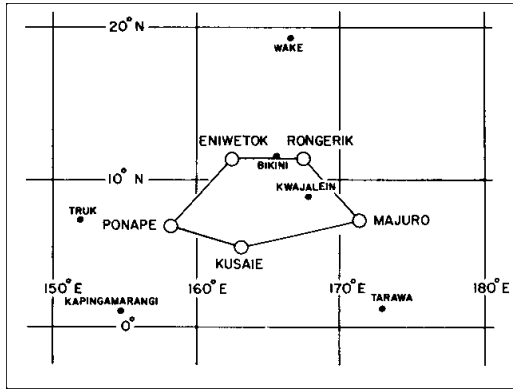
Figure 7.10: Conceptual model of a tropical oceanic squall line with trailing stratiform precipitation. All flow is relative to the squall line, which is moving from right to left. Numbers in ellipses are typical values of equivalent potential temperature (in K). (From Zipser, 1997)

7.8 Interaction between convection and the large-scale flow

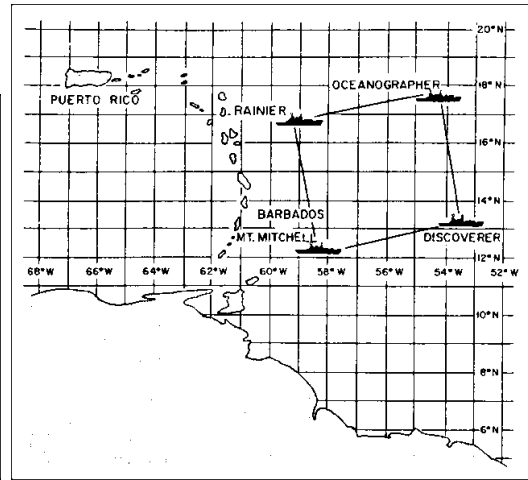
Attempts have been made to determine the bulk effects of convection on the large-scale flow through field experiments. The idea is to carry out serial radiosonde soundings over an array of three or more stations in a convectively-active region. One may carry out budget studies over the array to estimate the effects of convection on the array-averaged flow. Studies of this type were carried out for the GATE and AMEX experiments and two forerunners of GATE: the Line Island Experiment and the BOMEX Experiment. The station array networks for these experiments are shown in Fig. 6.9. The idea is illustrated by the following calculations.

The thermodynamic influence of cumulus convection on the large-scale flow, characterized by average quantities over the network array, can be expressed in terms of two quantities, Q_1 and Q_2 , called the apparent heat source and the apparent moisture sink, respectively. Thus

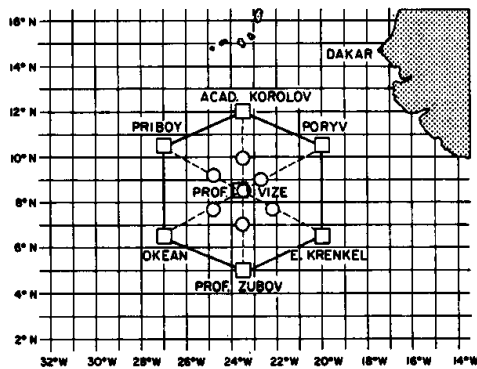
$$\frac{\partial \bar{h}_d}{\partial t} + \bar{u} \nabla \bar{h}_d + \bar{w} \frac{\partial \bar{h}_d}{\partial z} = Q_1 + Q_R, \quad (7.1)$$



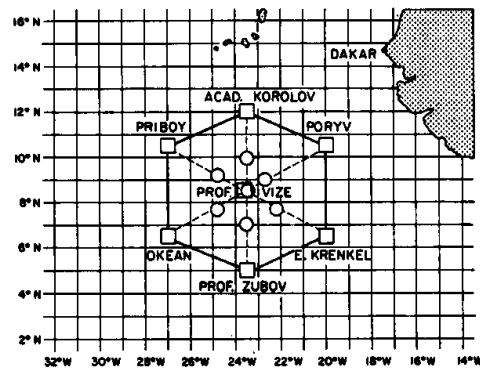
(a)



(b)



(c)



(d)

Figure 7.11: (a) Island stations in the Marshall Islands (1956) The polygon shows stations used to compute the large-scale budgets. (from Yanai *et al.* 1976). (b) BOMEX ship array (1969). (From Nitta, 1975). (c) Inner and outer ship-based radiosonde arrays during GATE (1974). The hexagon shows stations used in budget calculations discussed in the text (From Nitta 1977). (d) The six AMEX radiosonde stations, connected with lines. (From McBride *et al.* 1989).

$$\frac{\partial \bar{r}}{\partial t} + \bar{u} \nabla \bar{r} + \bar{w} \frac{\partial \bar{r}}{\partial z} = -\frac{Q_2}{L_{vo}}, \quad (7.2)$$

where

$$Q_1 = L_{vo}(C - E) - \frac{1}{\rho} \frac{\partial}{\partial z} \overline{\rho h'_d w'} \quad (7.3)$$

$$Q_2 = L_{vo}(C - E) + \frac{1}{\rho} \frac{\partial}{\partial z} \overline{\rho r' w'} \quad (7.4)$$

Note that

$$Q_1 - Q_2 = -\frac{1}{\rho} \frac{\partial}{\partial z} \overline{\rho h' w'} \quad (7.5)$$

This is a measure of the vertical eddy transport of total heat, i.e., it is a measure of the cumulus activity.

Budget equations

Integrating (6.6) gives

$$\int_0^\infty Q_1 dz = L_{vo} \int_0^\infty (C - E) dz - \overline{h'_d w'} \Big|_{z=0} \quad (7.6)$$

where P_o is the precipitation rate at the surface and the last term on the right-hand side is the surface sensible heat flux, H_o . Similarly

$$\begin{aligned} \int_0^\infty Q_2 dz &= L_{vo} \int_0^\infty (C - E) dz + L_{vo} \overline{r' w'} \Big|_{z=0} \\ &\approx L_{vo} P_s - L_{vo} \overline{r' w'} \Big|_{z=0} \\ &= L_{vo} (P_s - E_s). \end{aligned} \quad (7.7)$$

Here, E_s is the surface evaporation rate.

Appendix A

Appendix to Chapter 4

The canonical form of (5.32) is

$$\frac{d^2\psi}{dx^2} + (\lambda - x^2)\psi = 0. \quad (\text{A.1})$$

The solution procedure is to transform the variable ω to y where

$$\psi = \exp(-\frac{1}{2}x^2)y \quad (\text{A.2})$$

and to replace the constant $\lambda = 1 + 2\nu$. Then the equation reduces to Hermite differential equation

$$\frac{d^2y}{dx^2} - 2x\frac{dy}{dx} + 2\nu y = 0. \quad (\text{A.3})$$

We assume a solution of the form

$$y = \sum_{r=0}^{\infty} a_r x^{r+\rho}$$

and substitute in the equation. By equating the coefficient of x to zero one obtains the recurrence relation

$$a_{r+2} = \frac{2(r+\rho-\nu)}{(r+\rho+2)(r+\rho+1)}a_r. \quad (\text{A.4})$$

Equating the coefficient of $x^{\rho-2}$ to zero we obtain the indicial equation $\rho(\rho-1) = 0$.

Corresponding to the root $\rho = 0$ we have the recurrence relation

$$a_{r+2} = \frac{2(r-\nu)}{(r+1)(r+2)}a_r, \quad (\text{A.5})$$

which gives the solution

$$y_1(x) = a_1 \left[1 - \frac{2\nu}{2}x^2 + 2^2 \frac{\nu(\nu-2)}{4}x^4 - \frac{2^3\nu(\nu-2)(\nu-4)}{6}x^6 + \dots \right] \quad (\text{A.6})$$

where a_1 is a constant. Similarly, corresponding to the root $\rho = 1$ of the indicial equation we have

$$a_{r+2} = \frac{2(r+1-\nu)}{(r+3)(r+2)}a_r, \quad (\text{A.7})$$

which gives the solution

$$y_2(x) = a_2x \left[1 - \frac{2(\nu-1)}{3}x^2 + \frac{2^2\nu(\nu-1)(\nu-3)}{5}x^4 + \dots \right], \quad (\text{A.8})$$

where a_2 is a constant. The general solution of Hermite's differential equation is therefore $y(x) = y_1(x) + y_2(x)$. It can be shown that for general ν , both series (A.6) and (A.8) behave like $\exp(x^2)$ as $|x| \rightarrow \infty$. It follows that corresponding solutions to (A.1) behave like $\exp(1/2x^2)$. However, solutions to (A.1) which are bounded (in fact $\rightarrow 0$) as $|x| \rightarrow \infty$ are possible when ν is a positive integer. When $\nu = 2n + 1$ (an odd integer), the series (A.7) has likewise only $2n + 1$ terms. For particular values of a_1 and a_2 that depend on n , these finite series define the so-called Hermite polynomials denoted by $H_n(x)$. The first four are

$$\begin{aligned} H_0(x) &= 1 \\ H_1(x) &= 2x \\ H_2(x) &= 4x^2 - 2 \\ H_3(x) &= 8x^3 - 12x \end{aligned} \quad (\text{A.9})$$

In summary, solutions to (A.1) that are bounded as $|x| \rightarrow \infty$ exist only for certain values of $\lambda = 2n + 1$ where n is a positive integer. These solutions can be written in the form

$$\psi_n(x) = A H_n(x) \exp\left(-\frac{1}{2}x^2\right), \quad (\text{A.10})$$

where A is a constant. These solutions are related to the parabolic cylinder functions defined by

$$D_n(x) = 2^{-n/2} H_n(x/2^{1/2}) \exp(-x^2) \quad (\text{A.11})$$

which are solutions of the equation

$$\frac{d^2\psi}{dx^2} + \left(\lambda - \frac{1}{2}x^2\right)\psi = 0. \quad (\text{A.12})$$

Appendix B

The WKB-approximation

Consider the ordinary differential equation

$$\frac{d^2w}{dz^2} + m^2w = 0. \quad (\text{B.1})$$

If m is a real constant, solutions have the form

$$w = A^{\pm imz}, \quad (\text{B.2})$$

i.e. solutions are wave-like in z with wavelength $2\pi/m$. In this case B.1 may be written

$$\frac{d^2w}{dZ^2} + w = 0, \quad (\text{B.3})$$

where $Z = mz$. Clearly Z increases by 2π over one wavelength.

If $m = m(z)$, define

$$Z = \int m dz \quad (\text{B.4})$$

Then, if $m(z)$ increases with z , the wavelength becomes smaller, i.e. the solution $w(z)$ oscillates more rapidly, and conversely.

From B.4

$$\frac{d}{dz} = \frac{d}{dZ} \cdot \frac{dZ}{dz} = m \frac{d}{dZ}, \quad (\text{B.5})$$

and

$$\frac{d^2}{dz^2} = m^2 \frac{d^2}{dZ^2} + \frac{dm}{dz} \frac{d}{dZ}$$

whereupon B.1 becomes

$$\frac{d^2w}{dZ^2} + \left(\frac{1}{m^2} \frac{dm}{dz} \right) \frac{dw}{dZ} + w = 0. \quad (\text{B.6})$$

Now put $w = m^{-1/2}W$. Then

$$\frac{dw}{dz} = m^{-1/2} \frac{dW}{dz} - \frac{1}{2} m^{-3/2} \frac{dm}{dz} W = m^{1/2} \frac{dW}{dZ} - \frac{1}{2} m^{-3/2} \frac{dm}{dz} W,$$

using B.5. Then

$$\begin{aligned} \frac{d^2 w}{dz^2} &= m^{3/2} \frac{d^2 W}{dZ^2} + \frac{1}{2} m^{-1/2} \frac{dm}{dz} \frac{dW}{dZ} - \frac{d}{dz} \left(\frac{1}{2} m^{-3/2} \frac{dm}{dz} W \right) \\ &= m^{3/2} \frac{d^2 W}{dZ^2} + \frac{1}{2} m^{-1/2} \frac{dm}{dz} \frac{dW}{dZ} - \frac{1}{2} m^{-1/2} \frac{dm}{dz} \frac{dW}{dZ} - \frac{d}{dz} \left(\frac{1}{2} m^{-3/2} \frac{dm}{dz} \right) W \\ &= m^{-3/2} \frac{d^2 W}{dZ^2} - \frac{d}{dz} \left(\frac{1}{2} m^{-3/2} \frac{dm}{dz} \right) W \end{aligned}$$

and B.1 becomes

$$m^{3/2} \frac{d^2 W}{dZ^2} - \frac{d^2}{dz^2} (m^{-1/2}) W + m^{3/2} W = 0$$

or, finally

$$\frac{d^2 W}{dZ^2} + (1 + \delta) W = 0, \quad (\text{B.7})$$

where

$$\delta = m^{-3/2} (d^2/dz^2) (m^{-1/2}). \quad (\text{B.8})$$

It follows that, if $\delta \ll 1$,

$$W \sim e^{\pm iZ},$$

whereupon

$$w \sim \frac{1}{m^{1/2}} \exp \left\{ \pm i \int m dz \right\}. \quad (\text{B.9})$$

This is the WKB-solution to Eq. B.1.

Bibliography

- [1] Bjerknes, J., 1966: A possible response of the atmospheric Hadley circulation to equatorial anomalies of ocean temperature. *Tellus*, **18**, 824-829
- [2] Bjerknes, J., 1969: Atmospheric teleconnections from the equatorial Pacific. *Mon. Wea. Rev.*, **97**, 163-172
- [3] Bjerknes, J., 1970: Large-scale ocean-atmosphere interaction resulting from variable heat transfer at the equator. Rand Corp. RM-6353-ARPA, 23pp. [Available from The Rand Corporation, 1700 Main Street, Santa Monica, CA 90406, USA].
- [4] Bladé, I. and D.L. Hartmann, 1993: Tropical intraseasonal oscillations in a simple nonlinear model. *J. Atmos. Sci.*, **50**, 2922-2939
- [5] Chang, C.-P., J. E. Erickson and K. M. Lau, 1979: Northeasterly cold surges and near-equatorial disturbances over the Winter MONEX area during December 1974. Part 1: Synoptic Aspects. *Mon. Wea. Rev.*, **107**, 812-829.
- [6] Chang, C.-P., and K. M. Lau, 1980: Northeasterly cold surges and near equatorial disturbances over the Winter MONEX area during December 1974, Part 11: Planetary-scale aspects *Mon. Wea. Rev.*, **108**, 298-312.
- [7] Chang, C.-P., and K. M. Lau, 1981: Planetary-scale motions of winter monsoons during cold surge and break periods. *Proc. Int. Conf. on Early Results of FGGE and Large-Scale Aspects off Its Monsoon Experiments*, Tallahassee, WMO, **4**, 12-19.
- [8] Charney, J.G., 1963: A note on the large-scale motions in the tropics. *J. Atmos. Sci.* **20**, 607-609
- [9] Charney, J.G., 1969: A further note on large-scale motions in the tropics. *J. Atmos. Sci.*, **26**, 182-185
- [10] Cornejo-Garrido, A. G. and Stone, P. H., 1977: On the heat balance of the Walker Circulation. *J. Atmos. Sci.*, **34**, 1155-1162
- [11] Defant, A. and F. Defant, 1958: *Physikalische Dynamik der Atmosphäre*, Akademische Verlagsgesellschaft, 527 pp.

- [12] Fein, J. S. and J.P. Kuettner, 1980: Report of the summer MONEX field phase. *Bull. Amer. Meteor. Soc.*, **61**, 461-474
- [13] Fleming, R. J., T.M. Kaneshige and W.E. McGovern, 1979: The Global Wather Experiment 1. The observational phase through the first special observing period. *Bull. Amer. Meteor. Soc.*, **60**, 649-659
- [14] Geisler, J. E., 1981: A linear model of the Walker Circulation. *J. Atmos. Sci.*, **38**, 1390-1400.
- [15] Gill, A. E., 1980: Some simple solutions for heat-induced tropical circulations. *Quart. J. Roy. Meteor. Soc.*, **106**, 447-462
- [16] Gill, A. E., 1982: Atmosphere - Ocean Dynamics. International Geophysics Series. Vol. 30. Academic Press. 662pp.
- [17] Gray, W. M. and R. W. Jacobson, 1977: Diurnal variation of deep cumulus convection. *J. Atmos. Sci.*, **105**, 1171-1188
- [18] Greenfield, R. S. and T.N. Krishnamurti, 1979: The Winter Monsoon Experiment - Report of the December 1978 Field Phase. *Bull. Amer. Meteor. Soc.*, 439-444
- [19] Hadley, G., 1735: Concerning the cause of the general trade-winds. *Philos. Trans. R. Soc. London* **39**, 58-62
- [20] Halley, E., 1686: An historical account of the trade winds, and monsoons, observed in the seas between and near the tropicks, with an attempt to assign the phisical cause of the said winds. *Philos. Trans. R. Soc. London* **16**, 153-168
- [21] Held, I. M. and A. Y. Hou, 1980: Nonlinear axially symmetric circulations in a nearly inviscid atmosphere. *J. Atmos. Sci.*, **37**, 515-533
- [22] Hirst, A.C., 1989: Recent advances in the theory of ENSO. *Aust. Meteor. Oceonog. Soc. Newstetter*, **2**, No. 6, 101-113
- [23] Holland, G. J., J.L. McBride, R.K. Smith, D. Jasper and T.D. Keenan, 1986: The BMRC Australian Monsoon Experiment. *Bull. Amer. Meteor. Soc.*, **67**, 1466-1486
- [24] Holton, J. R., 1972: An Introduction to Dynamic Meteorology (1st Edn.). *International Geophysics Series*. Vol. 23. Academic Press. 391 pp
- [25] Holton, J. R., 1992: An Introduction to Dynamic Meteorology (3rd Edn.). *International Geophysics Series*. Vol. 48. Academic Press. 511 pp
- [26] James, I. N., 1994: Introduction to Circulation Atmospheres. Cambridge Atmospheric and Space Science Series. Cambridge University Press. 422 pp

- [27] Johnson, R. H., and R. A. Houze, 1987: Precipitating cloud systems of the Asian monsoon. In *Monsoon Meteorology*, Ed. C.P. Chang and T.N. Krishnamurti, Oxford Univ. Press, 298-353
- [28] Julian, P. R., and R. M. Chervin, 1978: A study of the Southern Oscillation and Walker Circulation phenomena. *Mon. Wea. Rev.*, **106**, 1433-1451
- [29] Knutsson, T. R., and K. M. Weickmann, 1987: 30-60 day atmospheric oscillations: composite life cycles of convection and circulation anomalies. *Mon. Wea. Rev.*, **115**, 1407-1436
- [30] Knutsson, T. R., K. M. Weickmann and J. E. Kutzbach, 1986: Global-scale intraseasonal oscillations of outgoing longwave radiation and 250 mb zonal wind during Northern Hemisphere summer. *Mon. Wea. Rev.*, **114**, 605-623
- [31] Kousky, V. E., and M. A. Gan, 1981: Upper tropospheric cyclonic vortices in the tropical South Atlantic. *Tellus*, **33**, 538-550.
- [32] Krishnamurti, T. N., 1971: Tropical east-west circulations during the northern summer. *J. Atmos. Sci.*, **28**, 1342-1347
- [33] Krishnamurti, T. N., Kanamitsu, W. J. Koss and J. D. Lee, 1973: Tropical east-west circulations during the northern winter. *J. Atmos. Sci.*, **30**, 780-787
- [34] Kuettner, J. P., D. E. Parker, D. R. Rodenhuis, H. Hoerber, H., Kraus and G.S. Philander, 1974: GATE. *Bull. Amer. Meteor. Soc.*, **55**, 711-744
- [35] Lau, K. M., and P. H. Chan, 1986: The 40-50 day oscillation and the El Niño-Southern Oscillation: A new perspective. *Bull. Amer. Meteor. Soc.*, **67**, 533-534
- [36] Lau, K. M. and L. Peng, 1987: Origin of low-frequency (intraseasonal) oscillations in the tropical atmosphere. Part I: Basic theory. *J. Atmos. Sci.*, **44**, 950-972
- [37] Lim, H., and C.-P. Chang, 1981: A theory of midlatitude forcing of tropical motions during winter monsoons. *J. Atmos. Sci.*, **38**, 2377-2392.
- [38] Lim, H. and C. -P. Chang, 1987: On the dynamics of midlatitude-tropical interactions and the winter monsoon. In *Monsoon Meteorology*, Ed. C.-P. Chang and T.N. Krishnamurti, Oxford Univ. Press, 405-434
- [39] Lindzen, R. S. and A. Y. Hou, 1988: Hadley circulations for zonally averaged heating centred off the equator. *J. Atmos. Sci.*, **45**, 2416-2427
- [40] Longuet-Higgins, M. S., 1964: On group velocity and energy flux in planetary wave motions. *Deep-Sea Res.*, **11**, 35-42.

- [41] Longuet-Higgins, M. S., 1968: The eigenfunctions of Laplace's tidal equations over a sphere. *Phil. Trans. Roy. Soc.*, **262**, 511-607
- [42] McAvaney, B. J., N. E. Davidson and J.L. McBride, 1981: The onset of the Australian northwest monsoon during Winter MONEX: Broadscale flow revealed by an objective analysis scheme. *Proc. Intern. Conf. on early results of FGGE and large-scale aspects of the Monsoon experiments. Tallahassee, Florida, USA, 12-17 January 1981.*
- [43] Madden, R. A., and P. R. Julian, 1971: Detection of a 40-50 day oscillation in the zonal wind in the tropical Pacific. *J. Atmos. Sci.*, **28**, 702-708
- [44] Madden, R. A., and P. R. Julian, 1972: Description of global-scale circulation cells in the tropics with a 40-50 day period. *J. Atmos. Sci.*, **28**, 702-708
- [45] Madden, R. A. and P. R. Julian, 1994: Observations of the 40-50 day tropical oscillation - A review. *Mon. Wea. Rev.*, **122**, 814-837
- [46] Matsuno, T., 1966: Quasi-geostrophic motions in the equatorial area. *J. Met. Soc. Japan.*, **44**, 25-42
- [47] Newell; R. E., J. W. Kidson, D. G. Vincent. and G. J. Boer, 1972: The General Circulation of the tropical atmosphere. Vol. 1. MIT Press, Cambridge, Massachusetts.
- [48] Newell; R. E., J. W. Kidson, D. G. Vincent and G. J. Boer, 1974: The General Circulation of the tropical atmosphere. Vol. 2. MIT Press, Cambridge, Massachusetts.
- [49] Nieuwolt, S., 1977: Tropical Climatology. An Introduction to the Climate of Low Latitudes. John Wiley & Sons, 207 pp.
- [50] Ooyama, K. V., 1969: Numerical simulation of the life-cycle of tropical cyclones. *J. Atmos. Sci.*, **26**, 3-40
- [51] Philander, S. G. H., 1990: El Niño, La Niña and the Southern Oscillation, R. Dmowska and J. R. Holton, Eds., Academic Press, 293 pp.
- [52] Ramage, C. S., 1968: Role of a tropical "maritime continent" in the atmospheric circulation. *Mon. Wea. Rev.*, **96**, 365-3??
- [53] Ramage C. S., 1971: *Monsoon Meteorology*, Academic Press, 296 pp.
- [54] Rasmusson, E. M. and J. M. Wallace, 1983: Meteorological Aspects of the El Niño/Southern Oscillation. *Science*, **222**, 1195-1202
- [55] Raymond, D. J. and A. H. Sobel, 2001: Forecasting convection, precipitation, and vertical motion in the tropics. Proc. Int. Workshop on the Dynamics and Forecasting of Tropical Weather Systems. Bureau of Meteorology, Australia.

- [56] Riehl, H. 1979: *Climate and Weather in the Tropics*. Academic Press. 611 pp.
- [57] Riehl, H. and J. S. Malkus, 1958: On the heat balance of the equatorial trough zone. *Geophysica*, **6**, 503-538
- [58] Sellers, W. D., 1965: *Physical Climatology*, Univ. of Chicago Press, 272 pp.
- [59] Silva Dias, P. L., W. H. Schubert and M. DeMaria, 1983: Large-scale response of the tropical atmosphere to transient convection. *J. Atmos. Sci.*, **40**, 2689-2707
- [60] Smith, W. L., H. M. Woolf, C. M. Hayden, D. Q. Wark, and L. M. McMillan, 1979: The TIROS-N Operational Vertical Sounder. *Bull. Amer. Meteor. Soc.*, **60**, 1177-1187
- [61] Sneddon, I. N., 1961: *Special Functions of Mathematical Physics and Chemistry*, Oliver and Boyd, 184 pp.
- [62] Sobel, A. H. and C. S. Bretherton, 2000: Modeling tropical precipitation in a single column. *J. Climate*, **13**, 4378-4392
- [63] Sobel, A. H., J. Nilsson and L. M. Polvani, 2001: The weak temperature gradient approximation, and balanced moisture waves *J. Atmos. Sci.*, in review.
- [64] Troup, A. J., 1965 The Southern Oscillation. *Quart. J. Roy. Meteor. Soc.*, **91**, 490-506
- [65] Virgi, H., 1981: A preliminary study of summertime tropospheric circulation patterns over South America estimated from cloud winds. *Mon. Wea. Rev.*, **109**, 599-610.
- [66] Vonder Haar, T. H. and V. E. Soumi, 1971: Measurements of the earth's radiation budget from satellites during a five year period. *J. Atmos. Sci.*, **28**, 305-314
- [67] Wallace, J. M., 1970: Time-longitude section of tropical cloudiness. December 1966 - November 1967. ESSA Technical Report NES-56 (ESSA TR NES-56).
- [68] Wallace, J. M., 1973: General circulation of the tropical lower stratosphere. *Rev. Geophys. Space Phys.*, **11**, 191-222
- [69] Wallace, J. M. and V. E. Kousky, 1968: Observational evidence of Kelvin waves in the tropical stratosphere. *J. Atmos. Sci.*, **25**, 900-907
- [70] Webster, P. J., 1972: Response of the tropical atmosphere to local steady, forcing. *Mon. Wea. Rev.*, **100**, 518-540

- [71] Webster, P. J., 1981: Mechanisms determining the mean and transient structure of the large scale winter monsoon circulation. *Proc. Int. Conf. on Early Results of FGGE and Large-Scale Aspects of Its Monsoon Experiments*, Tallahassee, WMO, **4**, 20-29
- [72] Webster, P. J., 1983: The large-scale structure of the tropical atmosphere. *General Circulation of the Atmosphere*, Eds. B. J. Hoskins and R. P. Pearce, Academic Press, 35-275
- [73] Webster, P. J., 1987: The variable and interactive monsoon. In *Monsoons*, Ed. J. S. Fein and P. L. Stephens, John Wiley & Sons, New York., pp. 269-230
- [74] Webster, P. J., L. Chou and K. M. Lau, 1977: Mechanisms effecting the state, evolution and transition of the planetary scale monsoon. *Pure Appl. Geoph.*, **115**, 1463-1491
- [75] Webster, P. J. and R. A. Houze, 1991: The Equatorial Mesoscale Experiment (EMEX): An overview. *Bull. Amer. Meteor. Soc.*, **72**, 1481-1505
- [76] Webster, P. J. and R. Lucas, 1992, TOGA COARE: The TOGA Coupled Ocean-Atmosphere Response Experiment. *Bull. Amer. Meteor. Soc.*, **73**, 1377-1416
- [77] Wheeler, M., G. N. Kilidis and P. J. Webster, 2000: Large-scale dynamical fields associated with convectively coupled equatorial waves. *J. Atmos. Sci.*, **57**, 613-640
- [78] Yanai, M., B. Chen, and W-W. Tung, 2000: The Madden-Julian Oscillation observed during the TOGA COARE IOP: Global view. *J. Atmos. Sci.*, **57**, 2374-2396